ABSTRACT

Title of Dissertation:	PERFORMANCE ENHANCEMENTS OF MICRO CORIOLIS VIBRATORY GYROSCOPES THROUGH LINEARIZED TRANSDUCTION AND TUNING MECHANISMS
	Ryan Knight,
	Doctor of Philosophy, 2023
Dissertation directed by:	Professor Don L. DeVoe
	Department of Mechanical Engineering

A quadruple mass Microelectromechanical System (MEMS) Coriolis vibratory gyroscope has been re-engineered with the singular focus of minimizing nonlinear transduction mechanisms, thereby allowing for angle random walk (ARW) noise reduction when operating at amplitudes higher than 2 μm.

The redesign involved six primary steps: (i) the creation of an aspect-ratio independent deep reactive ion etch with minimal notching on 100 μm thick silicon-on-insulator device layer, (ii) the creation of micro-torr vacuum packaging capability, enabling operation at the thermoelastic dissipation limit of silicon, (iii) the redesign of Coriolis mass folded flexures and shuttle springs, (iv) the linearization of the antiphase coupler

spring rate while maintaining parasitic modal separation, (v) the substitution of parallel plate transducers with linear combs, and (vi) the implementation of dedicated force-balanced electrostatic frequency tuners. Cross-axis stiffness is also reduced through folded-flexure moment balancing to further reduce ARW.

By balancing positive and negative Duffing frequency contributions, net fractional frequency nonlinearity was reduced to -20 ppm. The gyroscope presented in this research has achieved, a first reported of its kind, an ARW of 0.0005 °/√hr, with an uncompensated bias instability of 0.08 °/hr. These advancements hold promise for enhancing navigation and North-finding applications.

In tandem with gyroscope performance enhancements, vacuum packaging of ceramic chip carrier physics packages has achieved pressure levels below 1 micro-torr, a first in the field and remains state-of-the-art. Besides high-performance MEMS inertial sensors, ultrahigh vacuum packaging proves beneficial for chip scale atomic clocks, which require micro-torr vacuum levels to maintain fractional frequencies less than 10^{-12}.

Finally, an approach to tuning the quality factor mismatch between degenerate modes in as-fabricated gyroscopes has demonstrated a reduction in gyroscope bias instability. This tuning can be achieved by incorporating lead zirconate titanate into regions where the trade-off between mechanical *Q*, tuning *Q*, and bias instability reduction is balanced. Both modeling and empirical frequency data justify this approach, suggesting, for typical MEMS foundry Q mismatch of 7%, a 70× reduction in bias instability.

PERFORMANCE ENHANCEMENTS OF MICRO CORIOLIS VIBRATORY GYROSCOPES THROUGH LINEARIZED TRANSDUCTION AND TUNING MECHANISMS

by

Ryan Robert Knight

Dissertation submitted to the Faculty of the Graduate School of the
University of Maryland, College Park, in partial fulfillment
of the requirements for the degree of
Doctor of Philosophy
2023

Advisory Committee:
Professor Don L. DeVoe, Chair
Professor Hugh Bruck
Professor Miao Yu
Professor Francis Patrick McCluskey
Professor Christopher Cadou (Dean's Representative)

Dedication

To my incredible wife, my endearing son, and my parents.

Acknowledgements

First and foremost, I'd like to acknowledge my wife Alison – for tolerating late nights, being intrigued and curious about my research, and encouraging me to pursue this endeavor.

I would also like to recognize my team at the Army Research Laboratory (ARL) – Robert Benoit, Ryan Rudy, Brian Power, Jeffrey Pulskamp, and Scott Thoreson. Thank you for the challenging conversations, problem solving deep dives, and professionalism.

Much gratitude is given to ARL management and the organization as a whole. Parts of this technology area and test equipment capability presented in this thesis was built from the ground up.

Immense thanks to the cleanroom technicians Brian Power and Scott Thoreson for processing cassettes upon cassettes of silicon-on insulator-wafers. For giving me bad news, for giving me good news, and always communicating.

And to the L3Harris ARL cleanroom users, Phillip Sinsky and Scott Rauscher, and their openness and willing to collaborate and share the same deep reactive ion etching struggles as I was.

Finally, to the interns that I have mentored, Esmond Lau, Angelo Maio, and Chris Scheri, and their countless hours collecting gyroscope data.

Table of Contents

List of Tables

List of Figures

Chapter 1: Introduction

The following six chapters will present a comprehensive analysis of navigation-grade Microelectromechanical System (MEMS) gyroscopes. The dissertation will begin with the fundamentals of MEMS gyroscopes and progress to the fabrication of the Quadruple Mass Gyroscope (QMG) architecture. Next, the intricacies of vacuum packaging of high-performance physics packages and QMGs will be explored. A novel redesign of the QMG along with experimental outcomes is discussed before finally delving into strategies to improve bias instability.

Although the chapters are presented in a sequence-like manner, much of the fabrication challenges in Chapter 2 were evoked by the novel redesign of the QMG allowing for its large amplitude drive motion described in Chapter 4. The fabrication challenges created by re-engineering the QMG for large motion, linear transduction, have led to the demonstration of state-of-the-art MEMS gyroscope noise performance.

The third chapter describing vacuum packaging is presented in a somewhat generic manner due to its widespread relevance to various high-performance MEMS sensors, chip-scale atomic clocks, and the miniaturization of atomic and quantum systems. The vacuum packaging technology was developed from the ground up, has demonstrated state-of-the-art sub micro-torr stable pressure, and is now a sought-after capability at the Army Research Lab.

The penultimate chapter discusses the concept of tuning intrinsic quality factor and the implications on bias instability improvement. Certain piezoelectrics exhibit Q tuning behavior with DC polarization voltages and the performance enhancements to MEMS gyroscopes bias instability are presented and discussed. The final chapter summarize all the research activities presented in this dissertation along with the scientific impacts and future work.

1.1 Problem Motivation

The gyroscope is a vital component of an inertial measurement unit (IMU). IMUs can be categorized into two types: 1) gimballed platforms and 2) strapdown platforms. Gimballed platforms utilize spinning mass gyroscopes to stabilize the platform, ensuring the platform's orientation remains perpendicular to gravity. This orientation simplifies the position calculations for the inertial computer. On the other hand, strapdown IMUs lack gimbals and are directly attached to a vehicle. While they are more compact and have fewer mechanical complexities, the responsibility for position calculation is heavily reliant on inertial computation.

Accelerometers quantify motion in space, their output and associated errors are influenced by any drifts or inaccuracies in the gyroscope's orientation tracking and gravity subtraction. This is because accelerometers cannot differentiate between acceleration due to gravity and acceleration due to a vehicle moving. As a result, the process of IMU dead reckoning—integrating motion to monitor position—experiences a drift that amplifies over time at a cubic rate.

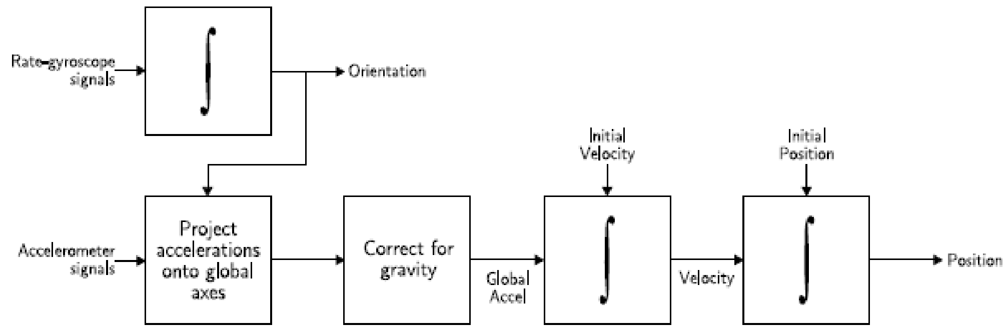

Figure 1.1-1. Flow diagram for IMU dead reckoning integration to obtain position [1]. Orientation error due to angular rate gyroscopes is integrated into position error proportional to cubic power of time.

To obtain an updated position measurement from a strapdown IMU, dead reckoning assesses the gravity vector relative to the IMU's orientation and its updated position. Since most strapdown IMUs measure angular rate rather than orientation, this rate must be integrated to derive the orientation (refer to Figure 1.1-1). Any error in measuring angular velocity is cumulatively incorporated into an orientation error. This misalignment, compounded over time, causes the position error to expand in proportion to cubic time. This is because gravity is tracked and corrected for by the orientation estimate. Moreover, angular rate integrates to orientation, orientation is used to correct for gravity, and gravity vector’s orientation error gets integrated twice for position. Thus, an accurate and high-performance gyroscope becomes the most essential component for strapdown IMUs.

Before the advent of the Global Positioning System (GPS), inertial navigation systems were reserved exclusively for costly strategic and marine applications. However, with the ubiquity of GPS in modern consumer electronics, navigation has become a standard component. A heavy reliance on GPS by consumers, industries, and governments creates vulnerabilities when signals are lost, jammed, or unavailable. Existing strategic- and navigation-grade gyroscope solutions are large, expensive, and consume significant power. The demand for smaller, more efficient gyroscopes to provide positioning when GPS is inaccessible is growing. This need is driven by contested environments such as urban canyons, tunnels, subterranean and underwater settings, and indoor navigation scenarios where GPS is either unavailable or not accurate. These GPS-contested environments are driving the need for high-performance inertial MEMS solutions. Other applications like inside-out virtual and augmented reality require high performance gyroscopes to track orientation [2]. Autonomous vehicles and other consumer markets need higher performing gyroscope, however, government applications as of recent have been the dominant driver in R&D for high performance inertial MEMS [3].

The Hemispherical Resonator Gyro (HRG), one of the highest performing gyroscopes, operates based on mechanical resonant principles rather than optical-based phenomena like fiber optic and laser ring gyros. Scaling from inches to microns requires compromises, but the fundamental mechanical principles provides motivation for high-performance inertial MEMS. These principles, akin to those of the HRG, remain applicable, just on a microscale.

1.2 History of Navigation Tools

Originating from Africa, man explored and colonized the entire globe thousands of years ago. With land exploration, navigation tools weren't as crucial, given our natural adaptability to land environments. However, maritime exploration and navigation were riskier due to the expansiveness of the oceans and resource scarcity. The earliest documented maritime navigation, conducted by the Polynesians circa 2000 BC, employed primitive tools like spatial representations of islands, recognition of winds, waves, and celestial bodies [4]. The Vikings also utilized celestial bodies for navigation, with legends recounting a luminous sunstone—an Icelandic spar—which reportedly revealed the sun's position even on cloudy days. However, no such stone has been discovered in shipwrecks by archaeologists to date [5].

By the dawn of the 16th century, the ancient arts of navigation began to develop rapidly as the new lands were being discovered. Tools like the magnetic compass, sextant, and clocks were utilized as tools to dead reckon by tracking the ships heading and speed. The nautical unit of speed, knot, is derived from a rope with tied knots approximately every 47 feet 3 inches that would be thrown overboard and timed with a 30 second sandglass [6]. By the mid-to-late 17th century, Europe's major seafaring powers recognized the crucial connection between timekeeping and navigation. Numerous countries incentivized innovation to tackle a central problem of the era: determining longitude at sea. While at sea, mariners would compare a clock synchronized to a port time (e.g., Greenwich time) to a local time (based on the Sun's position) to ascertain longitude. The shipboard clocks required very little timekeeping drift while at sea e.g., 39 seconds of time error corresponds to about 10 miles of longitude position error [7].

Navigation tools continued to improve but it wasn't until the early 20th century when inertial navigation systems were developed. Robert H. Goddard was one of the first people to use gyroscopes to guide and control rockets [9]. Gyroscope technology has been consistently advancing into the 21st century, spawning a variety of systems to measure rotation and orientation. These range from gimballed gyro-stabilized platforms, first employed in the Apollo spacecraft, to vibrating tuning forks and fiber optic and ring laser gyros based on the Sagnac effect. Currently the state of the art in rotation measurement and precision are atomic based systems where research over the years has significantly reduced the size of such devices from taking up the entire lab to shoe box size [10].

Starting from the mid-1990s, MEMS gyroscopes have steadily evolved from the original quartz tuning fork gyro developed by BEI Technologies [11] . The early 2000s saw the automotive industry acting as a catalyst for the creation of compact, affordable MEMS gyroscopes, which are now integral components of every smartphone.

1.3 Types of MEMS Gyroscopes

To date all commercial MEMS gyroscopes are Coriolis vibratory gyroscopes (CVG). They oscillate a rotationally sensitive proofmass, m_c, in resonance with an angular velocity equal to $A\omega_r$ and measure the Coriolis response to rotation Ω. The Coriolis acceleration term comes from the fundamental equations of motion for particle acceleration.

$$F_c \approx 2m_c\Omega \times A\omega_r \quad (1.1)$$

The majority of MEMS gyroscope use capacitive gaps for electrostatic transduction and while others, like Silicon Sensing Systems, use piezoelectric and inductive methods [12]. Until recently, MEMS gyroscope technology has been restricted to the red-dotted square shown in Figure 1.3-1 [13]. However, new DARPA programs [3] have been driving this space toward better bias, lower noise, and scale factor stabilities enabling short-term inertial navigation Figure 1.3-2. Note the distinct disparity between MEMS and high-performance "mechanical" gyroscopes.

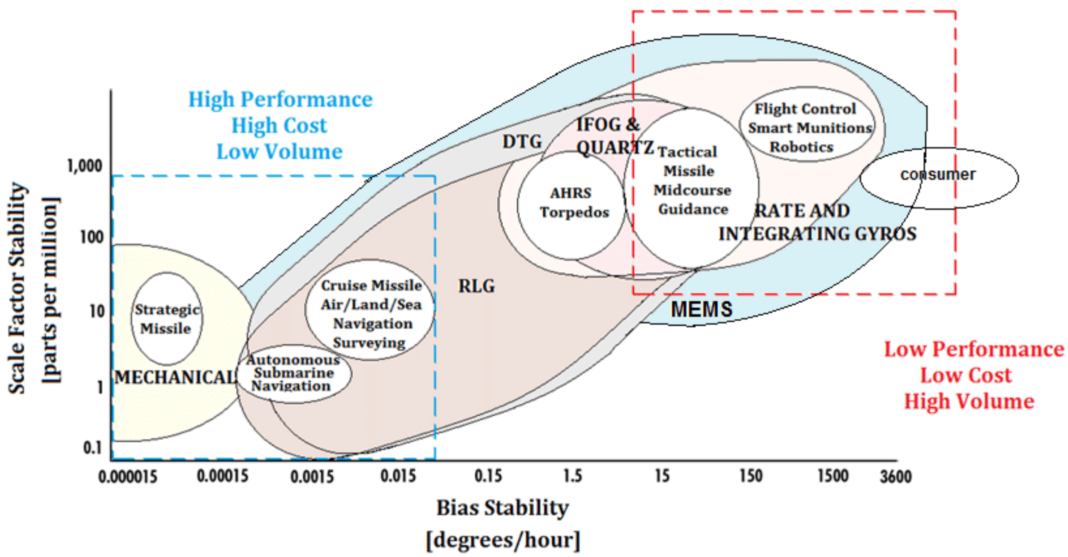

Figure 1.3-1. Historical performance of various gyroscope technologies as a function of scale factor stability and bias stability [13]. Note the two distinct regions between “mechanical” and “MEMS”. Mechanical and MEMS gyroscopes operate on the same physical principles and should overlap with scientific and technological improvements.

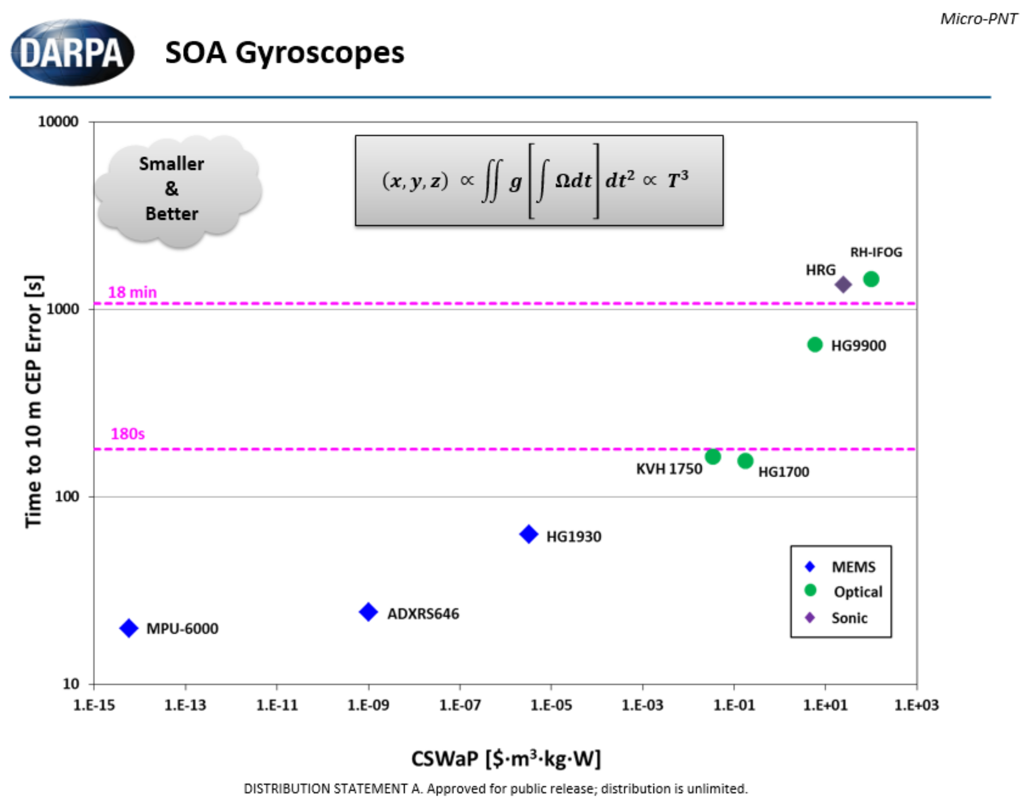

Figure 1.3-2. White space chart courtesy of DARPA [3] plotting the product of cost, size, weight, and power for various gyroscopes as a function mission time to obtain 10 meters of circular error probability. No MEMS IMU solution exists today that can navigation longer than 180 s with 10 m CEP error.

Figure 1.1-1, courtesy of DARPA, plots CSWaP [$m^{3}kgW] for various inertial measurement units. Here, it is assumed that the accelerometer produce zero error and the circular error probability (CEP) accumulates only due to the gyroscope. The plot is in log-log and illustrates that inexpensive consumer-level IMUs, like the MPU-6000, is 17 orders of magnitude lower in CWaP then a navigation or strategic grade IMU, while performance is two orders of magnitude lower.

1.3.1 Type I – Angle Gyroscope

Among the highest performing gyroscopes is the Delco hemispherical resonator gyroscope (HRG), now under the ownership and production of Northrop Grumman.

Superior to many fiber optic and ring laser gyroscopes, the HRG is purely mechanical. The HRG is a wine-glass-like structure that brings the rim into resonance, as shown in Figure 1.3-3. If resonance is continuously driven and the HRG experiences rotation, its Coriolis force, F_c , excites the degenerate and orthogonal mode where the resulting amplitude scales with drive vibration velocity, $A\omega_r$, and the input rotation rate Ω.

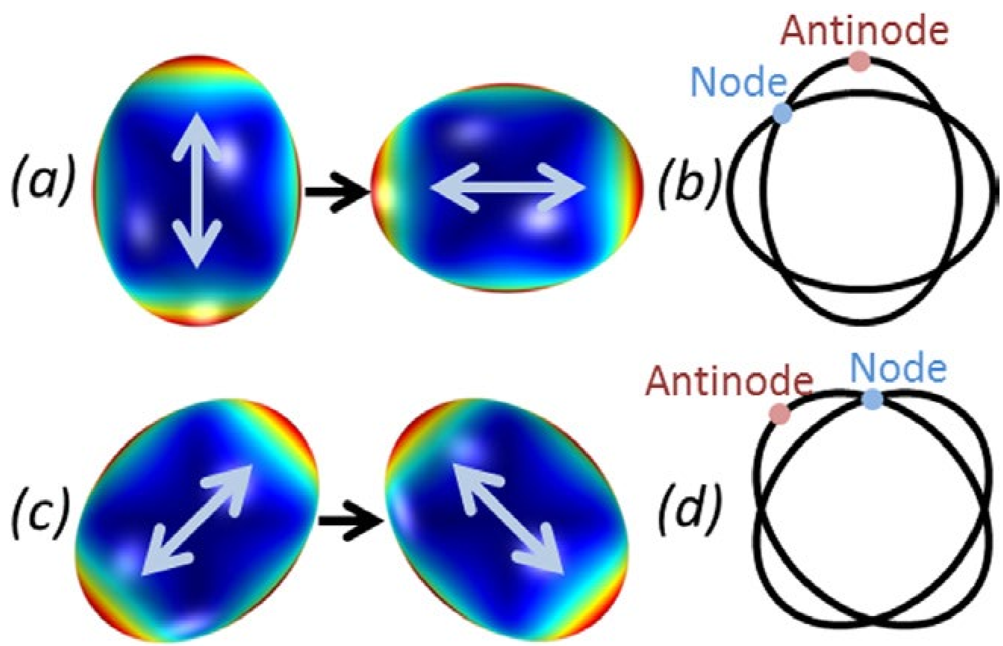

Figure 1.3-3. Hemispherical resonator gyro flex motion in its lowest order bending mode (n=2 mode) [15]. (a) and (b) illustrate the random position of its first degenerate mode and (c) and (d) illustrate the other degenerate mode shape 45 ° rotated from its first degenerate mode shape.

If the HRG is operated in angle mode, the rim is set into resonance and freely vibrates. As the HRG experiences rotation, the mode shape appears to rotate in the HRG inertial reference frame. Rotating the HRG by 90 ° causes the freely vibrating mode to precess 27 °. The angular gain, or Bryan factor, is the ratio of input angles to the precession angle; for the HRG, this value is 0.3 and approximately 1 for the Foucault pendulum [23].

The HRG is classified as a Type I gyroscope as it can directly measure angle. This type of gyroscope requires planar symmetry to measure angle while in free vibration. Near perfect fabrication and minor mechanical trimming are required for this operation, making it costly and time-consuming to produce. Type I gyroscopes can also function in angular rate output mode, thus possessing the capabilities of Type II (see following section). The Northrop Grumman HRG operates under both control paradigms and can switch between angular and rate modes [14].

1.4 Type II – Rate Gyroscopes

Type II rate gyroscopes, commonly found in smartphones, are the most prevalent type of MEMS gyroscope. This section describes various types of MEMS Type II rate gyroscopes and transitions to recent performance of quadruple mass gyroscope (QMG).

1.4.1 MEMS Coriolis vibratory gyroscopes

There are three high-performance MEMS gyroscopes architectures: a) disc resonator gyro (DRG) b) quadruple mass gyros (QMG) and c) tuning fork gyro (TFG). Out of these three high-performance gyros architectures, Boeing and HRL Laboratories first demonstrated it was possible in principle for optimized MEMS gyroscopes to approach useful levels inertial navigation at a fraction of the cost, size, and weight of the conventionally machined HRG. Various Boeing & HRL Laboratories DRG patents dated from 2005-2009 describe its functionality, U.S. Patent No. 7,168,318 & 7,581,443. The DRG design is a 2D version of the HRG and commonly resembles an 8 mm silicon disc. To reduce its radial stiffness relative to a solid disc, the DRG has a series of evenly spaced concentric rings and internal co-etched electrodes for electrostatic forcing and cross-axis frequency tuning. Dorian Challoner et al [16] demonstrated the first 0.01 °/hr bias stability MEMS gyroscope with a quality factor of 80,000 – a record in 2014 which still holds its ground.

The QMG was developed from work out of Professor Andrei Shkel's group at University of California at Irvine. U.S. Patent 8,322,213 describes a four-mass vibratory z-axis gyroscope with high sensitivity and shock rejection. Subsequent publications from this group later named it the quadruple mass gyroscope or QMG. The QMG evolved from their original two mass TFG that exhibited issues with shock susceptibility, vibration rectification error, and the desire to operate the gyros in angle mode (Type I). QMG research first reported Q's ~500k range and, as their fabrication and packaging improved, Q's neared 1.1M approaching the thermoelastic limit of silicon and their design [17]-[18]. The QMG was the first MEMS gyroscope shown to operate in both rate mode and angle mode [18].

Honeywell continues to enhance the performance of their mode-split TFG, but much of their architecture is not disclosed in literature. They offer the TFG only as a part of an IMU and not individually. Recent work by Endean et al. [19] has demonstrated impressive results based on a new tuning fork gyro, demonstrating in-run and over temperature bias stabilities of 0.01 deg/hr and ARW of 0.002 deg/√hr [19]- [20]. Honeywell is planning to integrate their gyroscope as a subcomponent to their HG7930 IMU in a future release [22].

1.5 Equations of motion for MEMS CVGs

Coriolis vibratory gyroscopes (CVGs) can generally be classified into two categories. The first type involves an offset or mode-split between the drive and sense modes. In the mode-split Tuning Fork Gyro (TFG), the tines oscillate in an anti-phase, while the sense mode is a torsional response of each tine. Alternatively, a CVG can operate in a mode-matched condition. Mode-matched gyroscopes, such as the HRG, DRG, and QMG, have symmetric geometries with identical degenerate modes, using the drive and sense quality factor gain to reduce signal to noise.

The principle of all CVGs is embodied by a Foucault pendulum or, equivalently, a point mass constrained to oscillate about the origin in the *xy* plane by an axisymmetric set of linear springs [24]. During oscillation, the point mass experiences a returning force of magnitude $F = -K\sqrt{x^2 + y^2}$ to its origin in Figure *1.5-2*.

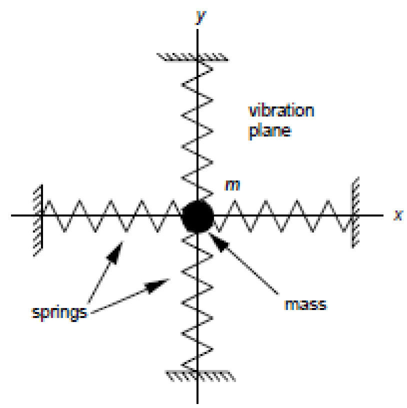

Figure 1.5-1. Foucault pendulum represented by a point mass two-dimensional oscillator with *x* and *y* springs [24].

When under z-axis rotation Ω, the point mass experiences a Coriolis force response orthogonal to its motion and proportional $-2m(\Omega \times v)$ where m and v correspond to the point mass and its velocity. The equations of motion for the two-dimensional oscillator can be generalized by applying an angular gain factor a_g, or Bryan factor [6], as a multiplier of the Coriolis and angular acceleration terms and a multiplier, a_g' of the centrifugal terms, they become

$$\ddot{x} - a_g\left(2\Omega\dot{y} + \dot{\Omega}y\right) + \left(\omega^2 - a_g'\Omega^2\right)x = f_x \quad (1.2a)$$

$$\ddot{y} + a_g\left(2\Omega\dot{x} + \dot{\Omega}x\right) + \left(\omega^2 - a_g'\Omega^2\right)y = f_y \quad (1.2b)$$

where $\omega = \sqrt{\frac{K}{m}}$ is the mass point's natural frequency of oscillation. f_x and f_y represent external force components per unit mass. The point mass oscillation velocity tends to be much larger than any input rotation rate Ω. Thus, angular acceleration and centrifugal terms, $\dot{\Omega}$ and Ω^2, are typically neglected.

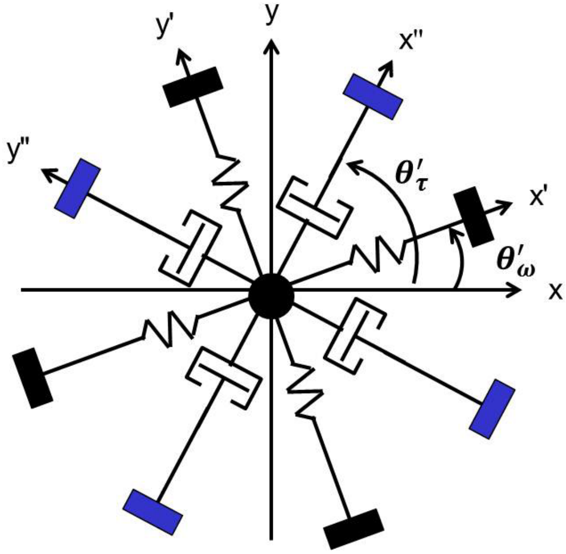

Figure 1.5-2. A point mass two-dimensional oscillator with *x* and *y* springs [24] with representative principal axes of stiffness (ω) and damping (τ). These principal axes aximuth and azimuth angles are introduced due to fabrication and stiffness asymmetries of the governing degenerate oscillator.

To accurately model the behavior of a CVG, anisodamping terms and different natural frequencies due to anisoelasticity for the two modes need to be included in Eq. (1.2a)-(1.2b).

$$\ddot{x} - a_g\left(2\Omega\dot{y} + \dot{\Omega}y\right) + \frac{2}{\tau}\dot{x} + \Delta\left(\frac{1}{\tau}\right)(\dot{x}\cos 2\theta_\tau + \dot{y}\sin 2\theta_\tau) + \left(\omega^2 - a_g'\Omega^2\right)x - \omega\Delta\omega(x\cos 2\theta_\omega + y\sin 2\theta_\omega) = f_x \tag{1.3a}$$

$$\ddot{y} + a_g\left(2\Omega\dot{x} + \dot{\Omega}x\right) + \frac{2}{\tau}\dot{y} - \Delta\left(\frac{1}{\tau}\right)(-\dot{x}\sin 2\theta_\tau + \dot{y}\cos 2\theta_\tau) + \left(\omega^2 - a_g'\Omega^2\right)y + \omega\Delta\omega(-x\sin 2\theta_\omega + y\cos 2\theta_\omega) = f_y \tag{1.3b}$$

where,

$$\omega^2 = \frac{{\omega_1}^2 + {\omega_2}^2}{2}; \quad \frac{1}{\tau} = \frac{1}{2}\left(\frac{1}{\tau_1} + \frac{1}{\tau_2}\right) \tag{1.4}$$

$$\omega\Delta\omega = \frac{{\omega_1}^2 - {\omega_2}^2}{2}\ ; \ \ \Delta\left(\frac{1}{\tau}\right) = \frac{1}{\tau_1} - \frac{1}{\tau_2} \tag{1.5}$$

The 2D oscillator of Figure 1.5-2 has not only been made asymmetric, so that the natural frequencies of the two modes, ω_1 and ω_2 are different, but the normal-mode axes have been assumed not to coincide with the pickoff axes x and y. θ_ω is the azimuth of the ω_2 normal-mode axis measured from the x direction. Similarly, the principal damping time constants, τ_1 and τ_2 , are assumed different and are assumed not to align with pickoff axes *x* and *y*. θ_τ is the azimuth of the τ_1 principal damping axis measured from the *x* direction. When stiffness and damping asymmetries are introduced the eigenvalues and eigenvectors for these locations can be derived from Eq. (1.3a)-(1.3b) and shown by the following equations:

$$\begin{bmatrix} \frac{2}{\tau} + \Delta\left(\frac{1}{\tau}\right)\cos(2\theta_\tau) & \Delta\left(\frac{1}{\tau}\right)\sin(2\theta_\tau) \\ \Delta\left(\frac{1}{\tau}\right)\sin(2\theta_\tau) & \frac{2}{\tau} - \Delta\left(\frac{1}{\tau}\right)\cos(2\theta_\tau) \end{bmatrix} \begin{bmatrix} \dot{x} \\ \dot{y} \end{bmatrix} \tag{1.6}$$

$$\lambda_{1,2} = \frac{2}{\tau} \pm \sqrt{\left(\Delta\left(\frac{1}{\tau}\right) cos(2\theta_\tau)\right)^2 + \left(\Delta\left(\frac{1}{\tau}\right) sin(2\theta_\tau)\right)^2} \tag{1.7}$$

$$v_{1,2} = \left(\frac{\Delta\left(\frac{1}{\tau}\right) cos(2\theta_\tau)}{\Delta\left(\frac{1}{\tau}\right) sin(2\theta_\tau)} \pm \frac{\sqrt{\left(\Delta\left(\frac{1}{\tau}\right) cos(2\theta_\tau)\right)^2 + \left(\Delta\left(\frac{1}{\tau}\right) sin(2\theta_\tau)\right)^2}}{\Delta\left(\frac{1}{\tau}\right) sin(2\theta_\tau)}, 1 \right) \tag{1.8}$$

Using the relationship $\omega^2 = \frac{k}{m}$ and assuming all masses are equivalent then the eigenvalue and eigenvectors can be calculated as the following:

$$\lambda_{1,2} = \frac{\omega_x^2 + \omega_y^2}{2} \pm \sqrt{\frac{\left(\omega_x^2 - \omega_x^2\right)^2}{4} + \left(\frac{k_{xy}}{m}\right)^2} \tag{1.9}$$

$$v_{1,2} = \left(\frac{\omega_x^2 - \omega_y^2}{2} \pm \frac{\sqrt{\frac{\left(\omega_x^2 - \omega_x^2\right)^2}{4} + \left(\frac{kxy}{m}\right)^2}}{\frac{1}{2}\left(\frac{kxy}{m}\right)}, 1 \right) \tag{1.10}$$

From Eq. (1.9)-(1.10) when a cross-axis component of stiffness exists the location of the principle axis of frequency (or stiffness) will always be at 45° from the *x* and *y* when k_{xx} and k_{yy} are tuned to match. To operate a Coriolis vibratory gyroscope in closed loop, the demodulated *y* sense axis signal is forced to be zero where quadrature and rate signal have a 90° phase difference. The term quadrature is the phase relation between the Coriolis sense signal and unwanted motion resulting from drive displacement. An oscillator moving in space, even if confined to a single plane, never has zero motion orthogonal to drive axis and quadrature describes this movement. The term quadrature is an ancient mathematical technique to model curving areas as squares. The term was then adopted by rotary encoders architectures, where square waves are used to determine position and direction by introducing another square wave 90° out of phase as the position signal. Because of this same phase relation with rotary encoders and early spinning mass gyroscopes use of rotary encoders, gyroscopes adopted quadrature to refer to the 90° phase difference between rotational sense movement and unwanted sense axis drive movement.

Section 4.2.2 will further discuss how to reduce quadrature with folded flexure designs where cross-axis movement is reduced.

Scale factor and bias from Eq. (1.3a)-(1.3b) can be derived for both the open loop and force rebalance operation modes [24].

$$SF = \frac{1}{k c_{x_0}} \sqrt{\frac{1}{\tau_y^2} + \left(\omega_x - \omega_{f_x}\right)^2} \qquad \text{for open loop} \qquad (1.11)$$

$$SF = \frac{1}{2k\omega_x c_{x_0}} \qquad \text{for closed loop} \qquad (1.12)$$

Where, c_{x_0} is drive motion amplitude and it's also related to forces in the open loop case by

$$c_{x_0} = \frac{\frac{f x_0}{2\omega_x}}{\sqrt{\frac{1}{\tau_x^2} + \left(\omega_x - \omega_{f_x}\right)^2}} \qquad (1.13)$$

Unlike open loop scale factor, closed loop force-to-rebalance operation does not have any appreciable gain associated with the sense quality factor when operating in the force to rebalance mode. In Chapter 4, design tradeoffs and novel changes are analyzed in order to increase c_{x_0} without being penalized by mechanical and electrical nonlinearities. Increasing c_{x_0} also has its implications to fabrication and those are discussed in Chapter 2.

Gyroscope zero-rate bias can also be determined from Eq. (1.3a)-(1.3b) by separating out the angular rate dependent terms and quadrature arriving with the following relationship,

$$Bias = \frac{1}{2a_g} \Delta\left(\frac{1}{\tau}\right) \sin(2\theta_\tau) + \omega\Delta\omega \cos 2\theta_\omega \frac{q}{a} \frac{1}{2a_g\omega_x} \qquad (1.14)$$

Large sources on zero-rate bias occur when there are large as-fabricated quality factor and frequency mismatches. To understand how the bias Eq. (1.14) may drift over time, taking the time derivate where quality and frequency are assumed to drift, the following is obtained:

$$\frac{d}{dt}Bias = \frac{\pi}{2a_g}\left(\frac{\dot{f}_x Q_y - \dot{f}_y Q_x}{Q_x Q_y} + \frac{f_y \dot{Q}_y {Q_x}^2 - f_x \dot{Q}_x {Q_y}^2}{{Q_x}^2 {Q_y}^2}\right)\sin(2\theta_\tau) + \frac{q}{a}\frac{1}{2a_g\omega_x}\cos 2\theta_\omega\left(\left(\frac{{\omega_y}^2}{{\omega_x}^2} + 1\right)\dot{\omega}_x - \frac{2\omega_y\dot{\omega}_y}{\omega_x}\right) \tag{1.15}$$

Bias drift is amplified by differences in drift for both frequency and quality factor. *Q* mismatch scales frequency drift mismatch, *Q* drift is scaled by frequency mismatch, and frequency mismatch scales the quadrature component of drift, i.e., the right part of Eq. (1.15) with the $\cos 2\theta_\omega$ term. Minimizing both frequency and *Q* mismatch will drive bias to zero and make bias drift less susceptible to time dependent changes to these components. Maximum quality factor, minimal damping and frequency misalignment, and higher drive frequency all help minimize bias drift over time. Chapter 3 focuses maximizing *Q* by the removal of air damping by creating a vacuum package where viscous forces have minimal impact on *Q*.

When gyroscopes are used in dead reckoning applications, the rate signal is continuously integrated, as highlighted in Chapter 1.1. Bias drift error is integrated into orientation error which then gets integrated twice as acceleration error, thus, in-run bias stability Eq. (1.14) is one of the most important gyroscope performance metrics to minimize.

The other salient gyroscope performance metric is angle random walk. ARW represents the standard deviation of the random angular rate noise per square root of time. If a gyroscope has no other noise mechanisms, then ARW is proportional to the integration time needed to average rate noise to obtain an accurate angular rate. E.g. and considering ARW as the only noise source, if ARW is equal to 1 deg/hr/√Hz then at 1 sec a one-sigma rate value of 1 deg/hr is obtained. Furthermore, after 100 sec a one-sigma rate value of 0.1 deg/hr is obtained. Low ARW is important for both navigation-grade applications as well as North finding gyrocompasses where true North is measured by modulated Earth's rotation rate. ARW as it relates purely to mechanical thermal noise (MTN) has been derived in [25] and shown below for both the open (OL) and closed loop (CL) control paradigms:

$$\text{ARW}_{\text{MTN,OL}} = \frac{1}{2a_g}\sqrt{\frac{k_B T \omega_y}{A^2 M \omega_x^2 Q_y}\left[1+\left(\frac{Q_y(\omega_y^2-\omega_x^2)}{\omega_x \omega_y}\right)^2\right]^{-1}}\frac{rad}{\sqrt{sec}} \tag{1.16}$$

$$\text{ARW}_{\text{MTN,CL}} = \frac{1}{2a_g}\sqrt{\frac{k_B T \omega_y}{A^2 M \omega_x^2 Q_y}\left[1+\left(\frac{Q_y(\omega_y^2-\omega_x^2)}{\omega_y}\right)^2\right]}\frac{rad}{\sqrt{sec}} \tag{1.17}$$

Similar to scale factor, ARW_{MTN}, is scaled by the inverse of drive amplitude, A, drive frequency ω_x, and the square of Coriolis mass, M, and sense quality factor Q_y. Sense drive frequency ω_y, temperature T, and the Boltzmann constant k_B, increase ARW_{MTN} by the square root. Any difference in ω_x and ω_y (delta frequency) also increase ARW_{MTN}.

The design and experimental results discussed Chapter 4 focus on reducing mechanical and electrical nonlinearities associated with the increase in drive amplitude A of Eq. (1.17). With careful consideration, increasing A will effectively reduce gyroscope rate noise and $\mathrm{ARW_{MTN}}$. The tradeoffs of increasing the denominator parameters, $M\omega_x^2 Q_y$, in Eq. (1.17) are also discussed.

The Allan variance method is a common technique to analyze gyroscope noise performance metrics such as angle white noise (slope = -1), angle random walk (slope = -1/2), bias stability (slope = 0), and rate random walk (slope = +1/2). Figure 1.5-3 plots the various noise sources where the slopes for each noise source are the lower limits for each respective noise source. Allan variance equation, where Allan deviation is the square root of Allan variance, is as follows:

$$\sigma_\Omega{}^2(nT_0) = \frac{1}{2(M-2n)} \sum_{m=1}^{M-2n} (\Omega_{m+2n} - 2\Omega_{m+n} + \Omega_m)^2 \tag{1.18}$$

$$\text{for } n = 1, 2, 3, \ldots, n_{max} \leq (M-1)/2$$

where, Ω_m is the gyro rate output, $\frac{1}{T_0}$ is data sample rate, $\mathrm{MT_0}$ is data record length. Allan deviation method determines reasonable estimates for the various gyroscope noise mechanisms resulting from both mechanical- and electrical-based components.

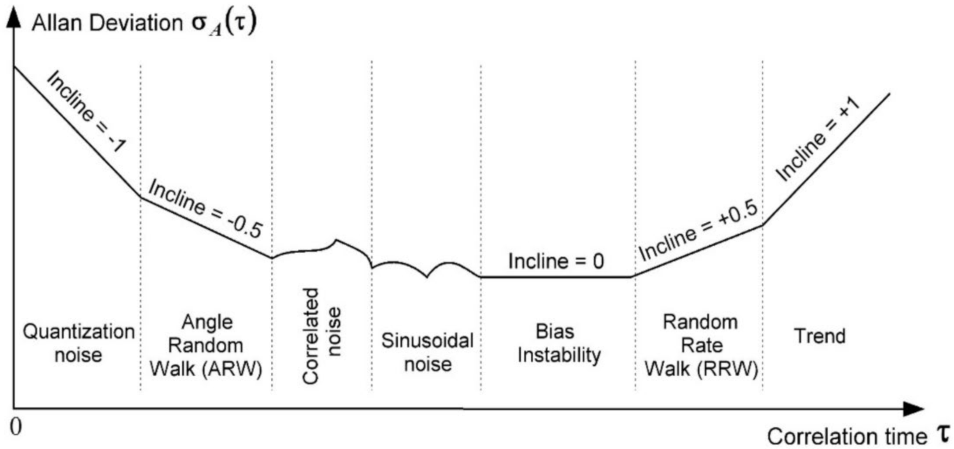

Figure 1.5-3. Allan deviation plot of various noise sources. The amplitude for slopes of -1, -1/2, 0, +1/2, +1 correspond to angle white noise, angle random walk, bias instability, rate random walk, and rate ramp respectively. $\sigma(\tau)$ is gyroscope output rate under zero applied rate and τ are windowed time bins. From [26].

Courtesy of Professor Andrei Shkel's group at the University of California, Irvine, access was given to the original quadruple mass gyroscope design files based on Drs. Adam Schofield and Alexander Trusov research. The work presented in the subsequent sections of this thesis makes several substantial design changes to the original QMG, allowing for large amplitude drive motion, and demonstrates state-of-the-art noise performance. The author acknowledges and appreciates the original groundwork on the QMG that has paved the way for this research.

Chapter 2: MEMS Fabrication

The necessity for precision manufacturing in high-performance mode-matched gyroscopes is highlighted by the need to minimize frequency mismatches between degenerate modes, eliminate potential sources of surface damping on the mechanical flexures, and to reduce damping asymmetries. As highlighted in Chapter 1.5, as-fabricated stiffness asymmetries need to be reduced to effectively tune the degenerate frequency modes to zero frequency mismatch. The minimal as-fabricated frequency mismatch places constraints on the precision of MEMS flexure tolerancing where nanometer of x and y critical dimensions need to be maintained. The silicon surface needs to remain pristine during fabrication, reducing defect density and contamination, thereby increase wafer yield.

Chapter 1.5 also highlights that one approach to reduce gyroscope angular rate noise, effectively angle random walk, is to increase the MEMS CVG drive amplitude. This desire to drive the CVG at large motion while maintaining considerable electrostatic transduction gain, creates a multi-aspect ratio deep reactive ion etching challenge. This chapter tackles that problem by developing morphed bulk and landing etches.

The fabrication work presented focuses specifically on the precision manufacturing of silicon MEMS gyroscopes, utilizing a 150 mm (100) silicon wafer fabrication process. Alongside precise fabrication, the use of a thick silicon device layer is desirable to scale the sensitivity of the Coriolis mass. However, deep etching of single-crystal silicon is not without its limitations, and fabrication imperfections tend to arise when a thicker device layer is employed.

The overall fabrication process steps of the quadruple mass gyroscope are rather straightforward, employing a three-mask process with four processing steps: 1) a backside photolithography mask to establish the gyro die attach to a chip-carrying package; 2) a topside photolithography mask to define wirebond electrical connection points; 3) a deep reactive ion etch (DRIE) mask to define the gyroscope structure; and 4) vapor hydrofluoric acid is then used to release the MEMS device layer from the silicon wafer buried oxide, enabling device layer mobility. Figure 2-1 illustrates a schematic of the four-step process flow.

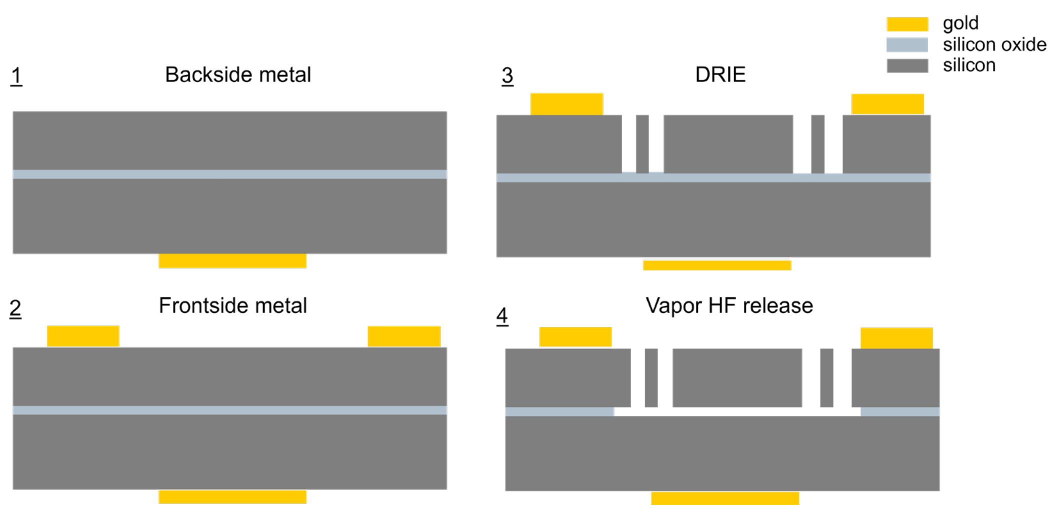

Figure 2-1. Quadruple mass gyroscope fabrication process flow. 1) backside metal, 2) frontside metal, 3) deep reactive ion etch 4) vapor hydrofluoric acid release.

Subsequent sections will describe the fabrication steps, focusing predominantly on the DRIE process. Due to its critical role in the fabrication process flow, the DRIE step is of particular significance. An aspect-ratio independent DRIE has been developed featuring a morphed bulk etch followed by morphed landing etch. The landing etch maintains critical dimension requirements while also minimizing notching at the buried oxide. In total, the DRIE recipe developed produces vertical and smooth sidewalls and lands cleanly on the buried oxide.

Precision DRIE is the most crucial step in the development of silicon high-performance MEMS inertial sensors and is thoroughly described. This chapter ends describing lessons learned which will hopefully guide the reader into not making the same mistakes and save time when developing their own etch.

2.1 Silicon wafer fabrication process

The fabrication of the MEMS gyroscope detailed in this dissertation begins with 150 mm (100) single crystal silicon-on-insulator wafers. The specifications are listed in *TABLE 2-1* below.

TABLE 2-1. SILICON WAFER SPECIFICATIONS

Lot #:	**MTO-A**
Diameter:	150 ± 0.5mm
Device Layer:	
Type/Dopant:	P/Boron
Orientation:	<1-0-0>
Thickness:	100 ± 1μm
Resistivity:	<0.005 Ω-cm
Edge Exclusion:	5mm
Particles:	<20@0.3μm
Surface:	Polished
Buried Thermal Oxide:	
Thickness:	5.0μm ± 5%
Handle Wafer:	
Flat/Notch:	SEMI Std.
Type/Dopant:	P/Boron
Orientation:	<1-0-0>
Thickness:	500 ± 10μm
Resistivity:	1 - 30 Ω-cm
Surface:	Polished

Device wafer fabrication commences with a Piranha clean, a 15-minute treatment in a 120 °C bath consisting of three parts sulfuric acid and one part hydrogen peroxide. Afterward, the wafers are rinsed with deionized water and prepared for backside photoresist. Surface defects on the silicon or photoresist, contamination, or particulates have the potential to disrupt subsequent fabrication steps like DRIE. Thus, it is crucial that wafer processing is undertaken with meticulous care to reduce defects, contamination, or particulates throughout the following steps.

2.2 *Silicon wafer fabrication process: backside metallization*

The silicon MEMS gyroscope die must adhere to a physics package, and for this purpose, eutectic-based adhesion proves most effective, offering minimal outgassing that could affect vacuum packaging pressure. Chapter 3 provides further insight into the importance of eutectic-based die attach. Consequently, backside metal is required to attach the silicon MEMS die to the physics package. Gold metallization is versatile, as it allows for the use of two types of eutectic materials: AuSn and AuSi.

The photolithography process employs a two-layer photoresist (PR) process. LOR10A is first spun onto the wafer and subsequently baked. Then, AZ nLOF 2020 is spun onto the wafer and exposed using the backside mask. The standard edge bead removal step has been omitted from this process to coat the wafer's edge with PR, the significance of which is discussed in Chapter 2.4.4. A chrome, platinum, gold stack is then deposited uniformly across the wafer using an Evatec™ metal evaporator. Chromium is necessary for silicon adhesion and platinum serves as a diffusion barrier for gold.

The dual-PR process forms canopies where the metal is deposited onto the silicon wafer, allowing acetone to undercut and remove the AZ nLOF 2020 PR. A thin circular sheet of metal floats to the top of the acetone bath, leaving only the photomask-defined region of metal on the silicon wafer. The LOR10A, which is not soluble in acetone, is subsequently removed in a Megaposit 1165 bath. The dual-PR metal liftoff process is cleaner than a single PR process because any metal contamination or particulates generated during AZ nLOF 2020 liftoff land on the LOR10A rather than the silicon surface. Contaminants and particulates adhered to the LOR10A are diluted in a subsequent Megaposit 1165 solvent bath, minimizing any metal-silicon surface defects that might result in unintentional masking effects in later fabrication steps. A two-layer photoresist process requiring two separate solvent cleans, protects, and produces a near defect-free metal liftoff process.

2.3 Silicon wafer fabrication process: frontside metallization

The frontside metallization process mirrors the backside metallization process with a few key distinctions: i) the front-side metal functions as conductive wirebonding paths to the MEMS device, ii) thicker platinum is used to create a diffusion barrier between the wirebond and gold contact relative to the silicon, and iii) before metal evaporation, the wafer is briefly dipped in buffered oxide etchant (BOE).

The frontside metallization defines the wirebonding pads for sensor transduction. As the physics package must undergo high-temperature baking prior to vacuum sealing, a thick platinum layer is necessary as a diffusion barrier between silicon and gold. AuSi has a eutectic temperature of approximately 380 °C, and when in contact, Au can actively reflow into Si. The high force and ultrasonic nature of wirebonding also necessitate a thick and robust platinum diffusion barrier to maintain the barrier post-wirebonding. Lastly, the BOE dip right before metal evaporation is required to remove any native oxide present on the silicon surface. Silicon oxide is an insulator and, if not removed, can limit current flow to and from the silicon transducers.

2.4 Silicon wafer fabrication process: deep reactive ion etching.

Arguably, the most essential step for any high-performance silicon MEMS is the deep reactive ion etch (DRIE) or deep silicon etch (DSE™). DRIE defines the mechanical structure, and any associated errors with this etch can impact performance. Errors such as photolithography mask tolerancing errors, critical dimension asymmetries, and photolithography optical astigmatisms are also transferred to DRIE and can become sources of sensor error and performance limitation.

DRIE is divided into three main process steps that are cycled: i) deposition of passivation polymer C_4F_8, ii) directional etch A assisted by a bias voltage source in an SF_6 plasma, and iii) an SF_6 isotropic etch B. Figure 2.4-1 illustrates the quasi-anisotropic nature of DRIE. The passivation step protects the silicon sidewall and etch A is a directional etch, normal to the silicon surface, that penetrates the passivation into the silicon. Then, etch B isotopically etches the silicon, creating sidewall scallops as the etch is looped from deposition, etch A, and etch B.

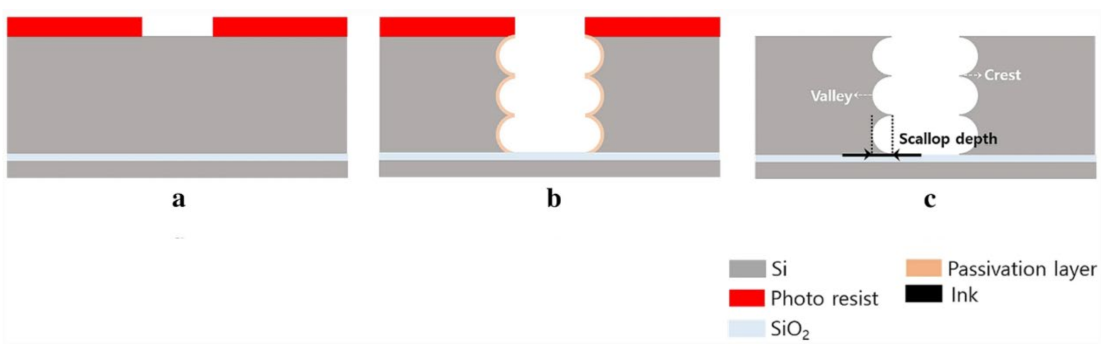

Figure 2.4-1. Example cross-section of DRIE characteristics. a) Red photoresist protects the areas where etching is unwanted, b) the passivation polymer during the deposition step coats the silicon sidewall, and c) the etch loops and creates scallops and stops at the buried oxide (SiO_2).

Table 2-2 shows how DRIE process variables change the etch behavior where the downward arrow decreases the etch behavior, the upward arrow increases the etch behavior, and the left/right arrow has very little effect on etch behavior. This table is useful when creating DRIE process recipes when undesirable etch behavior, such as grassing, is seen.

TABLE 2-2. DRIE PROCESS VARIABLES AND THEIR RELATIONSHIP TO ETCH BEHAVIOR FROM STANFORD NANO FAB WIKI.

Variable Increased	Etch Rate	Sidewall Roughness	Feature Blowout	Grass	Photoresist Selectivity	Polymer Breakdown
Etch gas	↑	↑	↑	↓	↑	↑
Dep gas	↓	↓	↔	↑	↑	↓
Etch:Dep time ratio	↑	↑	↑	↓	↔	↔
Pressure	↑	↑	↑	↓	↑	↑
Etch coil power	↑	↑	↑	↓	↑	↑
Dep coil power	↓	↓	↓	↑	↔	↓
Platen power	↔	↔	↔	↓	↓	↔
Etch EM1 value	↓	↔	↓	↔	↑	↓
Etch EM1 delay time	↔	↔	↔	↓	↓	↔

The quadruple mass gyroscope reported in this work focuses on large amplitude drive which requires multi-aspect ratio etch features. The comb drives are defined with a critical dimension (CD) spacing of 5 µm and 10 µm, springs have a 10 µm CD and 20 µm spacing, symmetric parallel plate frequency tuners have a 20 µm CD and 20 µm spacing, and given the antiphase motion of the QMG, 40 µm etch features need to accommodate this absolute amplitude motion. The aim to improve QMG performance creates a challenging DRIE fabrication problem due to the multi-aspect-ratio features necessary for large amplitude motion.

DRIE has different etch rates associated with aspect ratio, often referred to as etch lag, which is defined as the etch depth relative to the etch CD. The higher the aspect ratio, the thinner the etch pit width is per unit depth. A sensor layout with a single aspect ratio roughly etches at the same rate across the entire silicon wafer, allowing one to time the etch as it nears the buried oxide stop. The use of etch by-product end-point detection also serves as a precise way to time the DRIE when a single aspect ratio is used.

If the etch exposes the buried oxide, an undesirable characteristic called notching starts to occur. This is shown in Figure 2.4-2 on the bottom left.

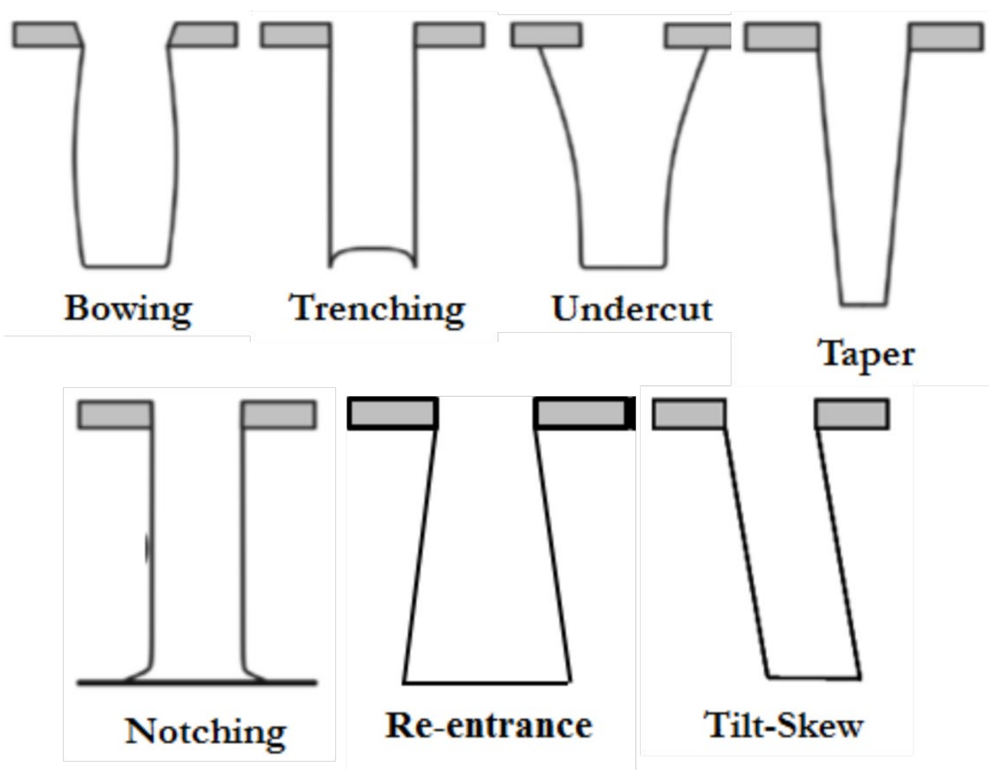

Figure 2.4-2. Various DRIE etch profiles that can be seen during process development from PlasmaTherm Versaline user manual.

The notching effect due to buried oxide charging will be the focus of the DRIE process recipe developed during this work. Tilt-skew (Figure 2.4-2 bottom right) does exist and is unavoidable due to the plasma radial angle where directed plasma angle of incidence becomes slightly off surface normal at radii greater than 50 mm.

As the DRIE progresses through the silicon device layer, the charged SF_6 plasma gets absorbed into the silicon, and the charge dissipates due to the semiconducting nature of silicon. An illustration of this effect is shown in Figure 2.4-3 where charge generated from the plasma is nullified by the silicon. Once the DRIE starts to expose the insulator, and in this work, the buried oxide, the insulator begins to charge.

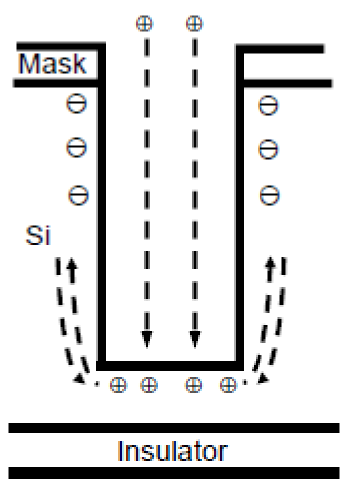

Figure 2.4-3. This figure illustrates current flow within the silicon substrate that prevents charge separation during the bulk etch.

As the insulator charges, etch A begins to be deflected due to plasma being accelerated downwards and repulsion caused by the charged insulator. This effect is shown in Figure 2.4-4. When performing DRIE on silicon with a buried oxide stop, notching is an unavoidable phenomenon. Therefore, DRIE equipment manufacturers, like SPTS or PlasmaTherm, have proprietary methods to minimize notching. This work only has access to a PlasmaTherm Versaline P10111 with the fast-switching Cortex v2.6.1 software and hardware and is reported to have similar DRIE quality as SPTS platforms.

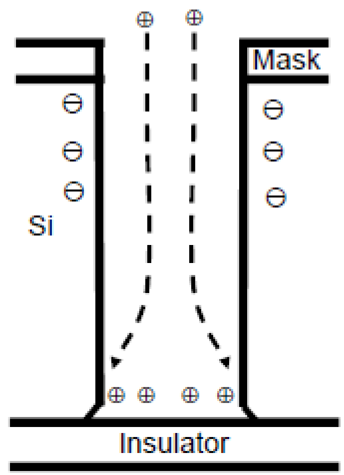

Figure 2.4-4. This figure illustrates the charging effect that causes notching to occur when the insulator is exposed to plasma.

The PlasmaTherm Versaline is equipped with a low-frequency bias voltage source that can be frequency modulated (FM). The bias voltage source provides the excitation energy to direct the SF_6 plasma ions downward towards the silicon surface, allowing for the directional etch A. The software comes with three selectable waveforms, two of which are preprogramed. "Waveform 1" is the standard etch low frequency bias voltage at 100 kHz. PlasmaTherm's general guidance document states this is not power, perhaps to not infringe on the Bosch DRIE patent. Regardless, when an AC voltage source is presented with a plasma RF impedance, power follows the simple relationship of $\frac{V^2}{|Z|}$ where V is voltage and Z is source impedance. The other preprogrammed waveform, "Waveform 2", is used to mitigate the notching phenomena. Waveform 2 uses an frequency modulated 100 kHz / 1 kHz at a 25% duty cycle. This means that 25% of the time the 100 kHz source frequency is on and 75% of the time the 1 kHz source is on. Waveform 2 is designed to discharge the buried oxide insulator, mitigating notching.

The recipe developed to etch the multi-aspect ratio QMG, presented in this work, is a two etch process. The first etch, commonly called the bulk etch, defines the lowest aspect-ratio feature that is critical to the operation of the QMG. In this case, the aspect ratio is 2.5, where a 40 µm trench is being etched. The bulk etch is timed to nearly clear out the 2.5 aspect ratio features. A landing etch is then used with Waveform 2 to minimize notching at the 2.5 aspect ratio feature while continuing to etch the 5:1, 10:1, and 20:1 aspect ratio regions. The 20:1 aspect ratio is cleared last and is the final endpoint of the etch. Figure 2.4-5 illustrates a schematic of how to time a multi-aspect ratio etch. Note, finish and landing etch are used interchangeably.

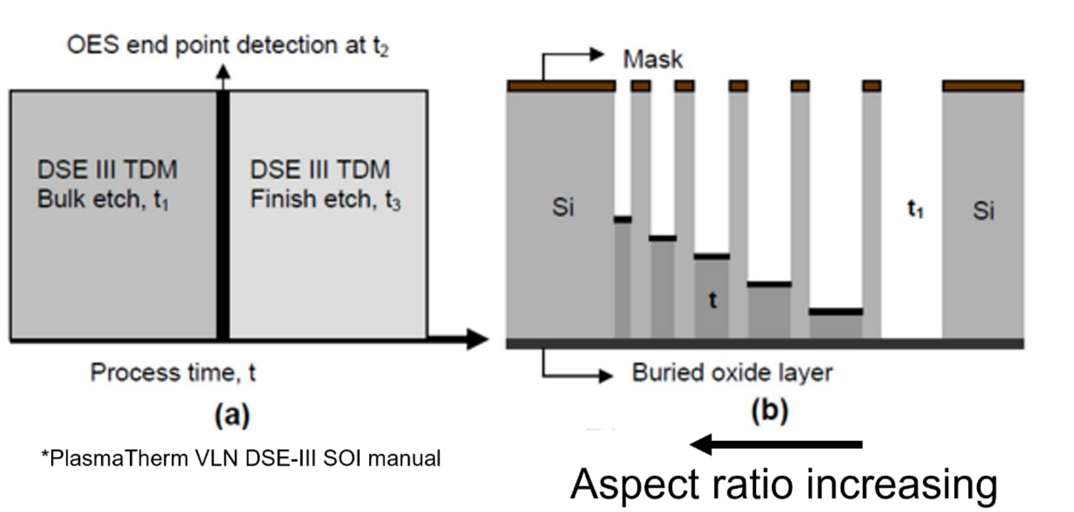

Figure 2.4-5. Example schematic of (a) the bulk and landing (finish) etch versus time and (b) the multi-aspect ratio etch behavior where t_1 is the targeted time to initiate the landing (finish) etch.

Figure 2.4-6 is a scanning electron microscopy image of the QMG and a cross-sectional view. This etch test was conducted on a dummy silicon wafer to characterize the factory acceptance testing (“FAT”) recipe developed by PlasmaTherm specifically for the Army Research Laboratory Versaline tool. Etch trenches varying from 5-40 µm illustrate the etch rate dependency (or lag) on aspect ratio.

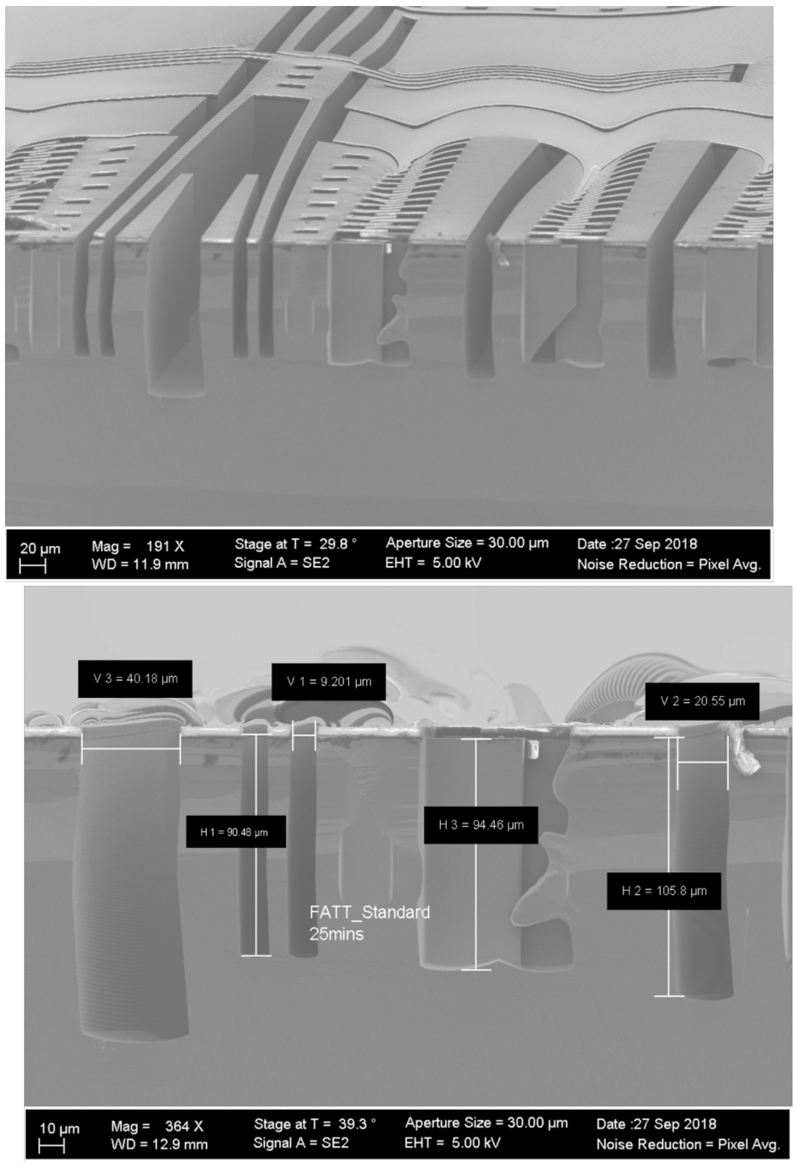

Figure 2.4-6. (top) Side view of QMG coupler and comb transducers (bottom) zoomed-in cross-sectional view of (top).

2.4.1 Deep Reactive Ion Etching – Process terminology and parameters

Given that multi-aspect ratio trench features exhibit different etch rates, developing a DRIE recipe that minimizes notching necessitates over-etching across all trench regions, beginning with the lowest aspect ratio feature. The two main methods to minimize notching are 1) the proper protection of lower aspect-ratio features with C_4F_8 passivation polymer and 2) the utilization of Waveform 2, as described in section 2.4. Once the lower aspect ratio features have been cleared, increasing passivation will not affect these areas but will safeguard them against notching. Nevertheless, the process of increasing polymer deposition is a delicate balancing act. An excessive amount of polymer results in nano-pillars commonly referred to as 'grass.' This occurs when etch A fails to eliminate all the polymer, creating masked regions that make the silicon surface appear as if it has silicon grass on it. Thus, a careful balance between deposition and etch A is maintained throughout the etch.

The two main physical mechanisms responsible for creating etch rate-dependent aspect-ratio features is diffusion and ion depletion due to sidewall capture. As the aspect ratio increases, diffusion starts affecting both the polymer passivation and the etch of the plasma gas species (C_4F_8 and SF_6, respectively). Likewise, the angular distribution of incoming ions into the trench opening cause a higher percentage of the ions to be capture by the sidewalls. Electrostatic fields will also deflection ion in the trenches creating further sidewall depletion. As a result, PlasmaTherm has integrated etch morphing into their software. This feature allows for linear and nonlinear morphing of various etch parameters, including deposition and etch time. The morphed parameters can undergo rapid changes throughout the etch recipe or slower changes, depending on the selected curve number. For instance, if a morphed parameter is programmed to increase from value 1 to value 2, and the morphed value is 0.1, then value 1 will remain almost unchanged until the end of the process when it ramps up to value 2 Conversely, if the morphed value of 9 is selected, then value 1 rapidly transitions to value 2 at the start of the process. Example morphing curves are provided in *Figure 2.4-7*.

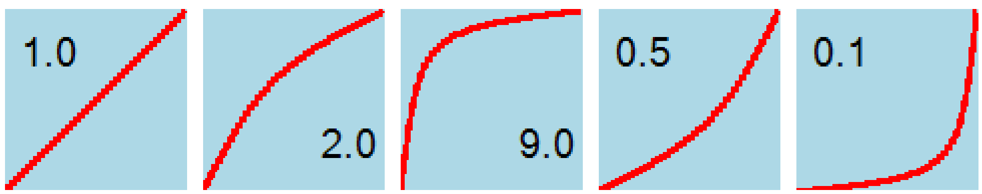

Figure 2.4-7. PlasmaTherm etch morphing curves associated with morphing values proportional to growth factor which is the number in each plot.

In late 2020, the Army Research Laboratory PlasmaTherm Versaline tool underwent a preventive maintenance protocol conducted by PlasmaTherm, which validated our factory acceptance test recipe for high aspect ratio etching. Thus, this "FAT" etch recipe was employed as the starting point for recipe development. This recipe is a single shot recipe without morphing or landing etch. Figure 2.4-8 presents a cross-sectional SEM of 20 µm wide features that are etched to the buried oxide. Several microns of notching are visible. The "FAT" etch recipe is considered the initial bulk etch, and process parameters will be adjusted to meet the multi-aspect ratio demands of the QMG.

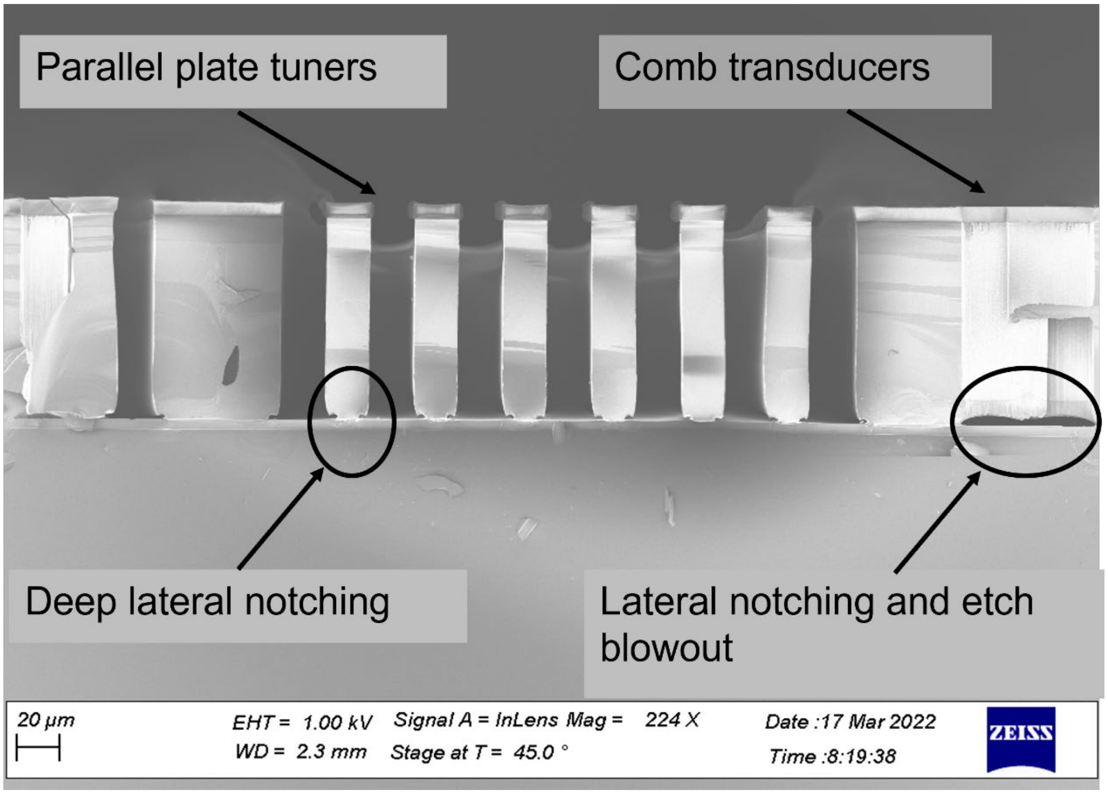

Figure 2.4-8. Bulk "FAT" factory acceptance test etch developed for high aspect ratio features. The 20 µm wide 100 µm tall features exhibit bad notching at the buried oxide interface.

2.4.2 *Deep Reactive Ion Etching – bulk etch modifications.*

The bulk etch recipe, using the factory acceptance testing recipe specifically developed by PlasmaTherm for the DRIE tool at the Army Research Laboratory, served as the baseline starting point for recipe modifications. Given that the 40 µm features are the first to clear, they require protection from the additional etch cycles needed to clear the 5 µm features. An increased passivation deposition time can provide the necessary protective film to mitigate notching. However, as shown in Table 2-1, 'grass' may occur in high aspect ratio regions. To maintain a balance between passivation and etch A, both deposition and etch A time were increased by

67% and 133%, respectively. Considering previous SEMs, such as Figure 2.4-8, showed a clean and vertical etch during the initial third of the process, a morphing value of 0.5 was selected. This allowed deposition and etch A time to change more quickly as the recipe approached the end of its total cycle iterations. As etch B is the isotropic etch, it has remained unchanged. While the morphing parameter was never optimized and could potentially be extended to between 0.3 to 0.9, given the timeline, the author decided to proceed to the second etch, the landing or finishing etch. Figure 2.4-9 and Figure 2.4-10 are SEMs that illustrate the acceptable etch behavior, thereby justifying the author's motivation to focus on the landing etch.

The morphed bulk etch process recipe is listed in *Table 2-3* detailing all process parameters necessary for replication. The author warns that replicating this recipe will most likely not create the same results as the presented SEMs.

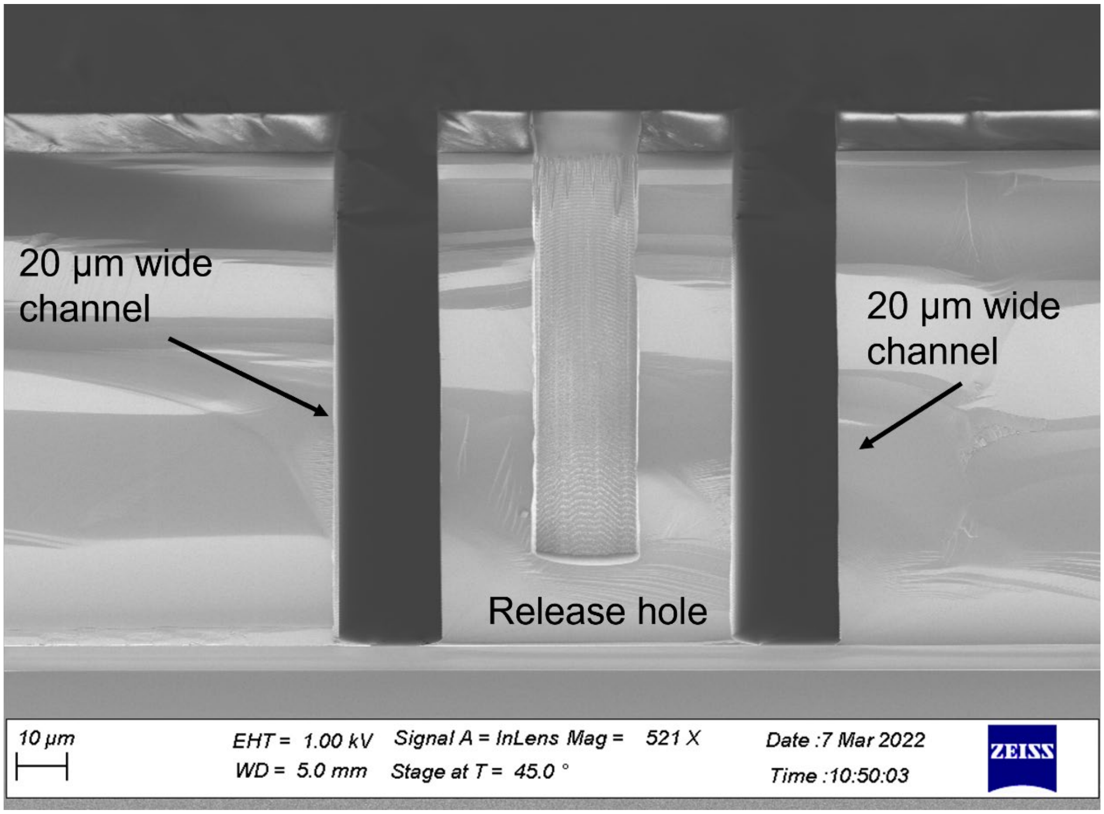

Figure 2.4-9. Bulk etch recipe with 0.5 morphing of deposition and etch A time. Shown in SEM are two 20 µm wide trenches/channels and centered between the two trenches is a 20 × 20 µm release hole. Even though the release holes have the same aspect ratio as the 20 µm wide channels, the into-the-page length also impacts the etch rate. Device layer silicon thickness is 100 µm.

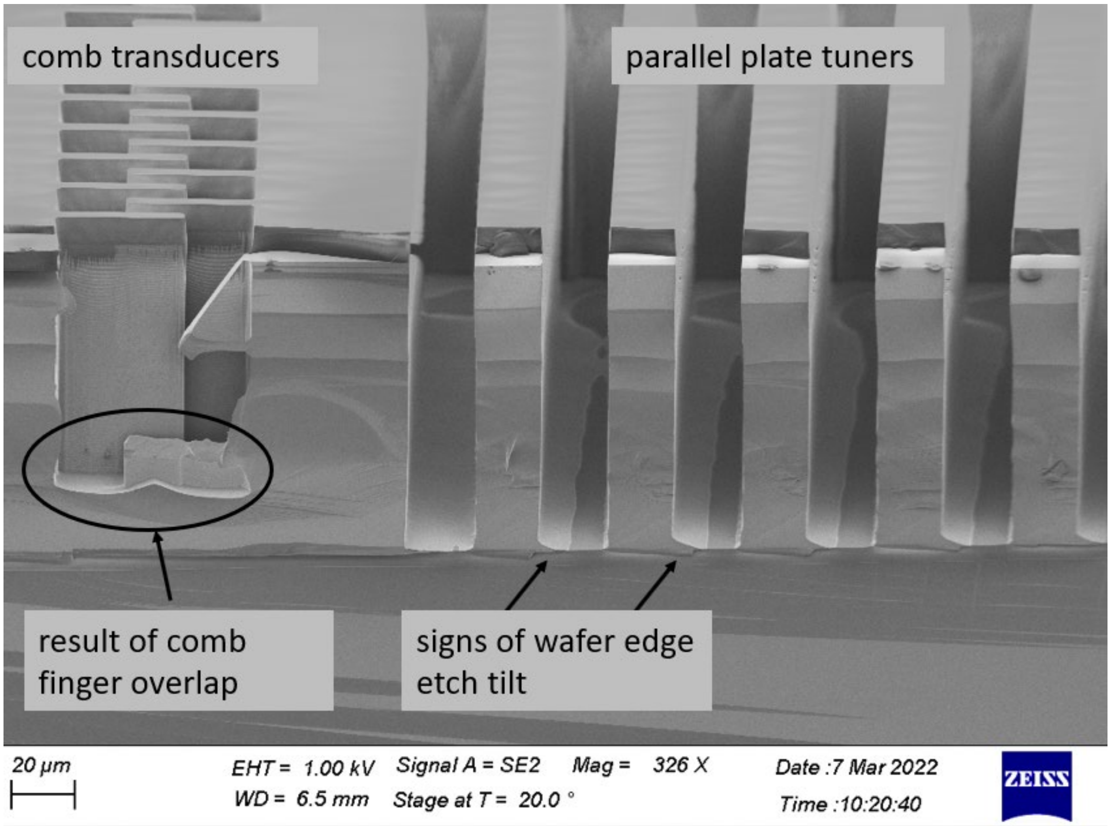

Figure 2.4-10. Bulk etch recipe with 0.5 morphing of deposition and etch A time. Comb transducer with 10 and 5 µm features (overlap and comb gap, respectively) and 20 µm wide parallel plate tuners. SEM location is at wafer edge showing signs of etch tilt (Figure 2.4-2).

TABLE 2-3. MODIFIED BULK ETCH RECIPE WITH NONLINEAR MORPHING OF “DEP” AND “ETCH A” FROM 1.5 TO 2.5 S AND 1.5 S TO 3.5 S, RESPECTIVELY.

RK_FAT_40-1 DSE morph EtchA P10111 ARL

1) < Initial >
2) < Chuck >
3) stab
4) ignition
5) Dep
6) Etch A
7) Etch B
8) Loop 300 times
9) < Dechuck >
10) < End >

	1. < Initial >	2. < Chuck >	3. stab	4. ignition	5. Dep	6. Etch A	7. Etch B	8. Loop to 5
Duration	0:10.0		0:15.0	0:05.0	0:01.5 ► 0:02.5 § 0.5	0:01.5 ► 0:03.5 § 0.5	0:02.0	225 Iter.
Spool	175.0							
Lid	150.0							
Liner	70.0							
Electrode	5.0							
Pressure	1.0	20.0	20.0	20.0	25.0	25.0	50.0	
C4F8		0.0	150.0	150.0	150.0	▼ 150.0	▼ 150.0	
SF6		0.0	▼ 200.0	▼ 150.0	▼ 150.0	150.0	150.0	
Ar		20.0	30.0	30.0	30.0	30.0	30.0	
Bias		0	0	1,000	10	650	10	
ICP		0	0	1,500	1,500	1,000	2,000	
Mode		Default	Manual	Auto	Hold	Hold	Hold	
Load			50.0					
Tune			74.0					
N/A		0	0	0	0	0	0	

2.4.3 *Deep Reactive Ion Etching – landing etch.*

The landing etch is the most significant and impactful stage of the etching sequence. It has two primary objectives: i) to prevent notching in the low aspect ratio CD regions and ii) to continue etching the high aspect regions that have yet to land on the buried silicon oxide. As the landing etch begins when the feature with the lowest CD is at the buried oxide, Waveform 2 is used. Waveform 2 is a preprogrammed FM signal designed to mitigate notching. It employs a 100 kHz / 1 kHz frequency at a 25% duty cycle, meaning that the 100 kHz source frequency is on 25% of the time, and the 1 kHz source is on for the remaining 75%. Waveform 2 is designed to discharge the buried oxide insulator, thereby mitigating notching.

The Army Research Laboratory PlasmaTherm Versaline tool comes with a 'finishing etch' recipe, which was found to cause feature blowout. Figure 2.4-11 shows an SEM of the comb features experiencing base blowout due to the lateral etching of the 'finishing etch' recipe. The primary differences between the bulk etch and the PlasmaTherm finish are: i) a 5.0 s etch A duration, ii) an increased bias voltage on etch A from 650 to 700 V. Despite the use of 'Waveform 2,' lateral etch blowout still occurs. This is attributed to the in complete discharging of the buried oxide, which directs the etch towards the 5 µm comb fingers. The extended etch A duration causes etch taper and lateral etching, reducing the comb's effective height from 100 µm to ~75 µm.

Figure 2.4-11. Example of feature blowout at the comb location near the buried oxide. The lateral etch rate behavior of the PlasmaTherm provided "Finishing Etch" caused 5 µm to lose 15-25 µm of total height.

Following literature reviews and numerous consultations with PlasmaTherm, including the provision of one of their bulk+landing etch processes of record, the conclusion was reached that each process recipe differs depending on the specific DRIE tool and DRIE etch mask and depth. Consequently, a landing etch was developed with only partial guidance from the literature and PlasmaTherm.

The landing etch is intended to be slower than the bulk. Guided by PlasmaTherm, an etch B time was set to 1 s, down from 2 s in the bulk etch. As the balance between deposition and etch A remains crucial, the landing etch continues where the bulk etch ends, with the same deposition and etch A parameters used, apart from an initial 50 V increase in etch A.

When transitioning from the bulk to the landing recipe, the chuck is cooled from 5 °C to 1 °C due to the additional heat generated when the buried oxide is exposed. This cooling step takes about 15 minutes before the landing etch begins. The deposition and etch A times remain unchanged, and 'Waveform 2' is selected. Figure 2.4-12 shows a cross-sectional SEM at the comb region where the etch gap is 5 µm wide. While some loss of CD and sharding were evident, no notching was observed.

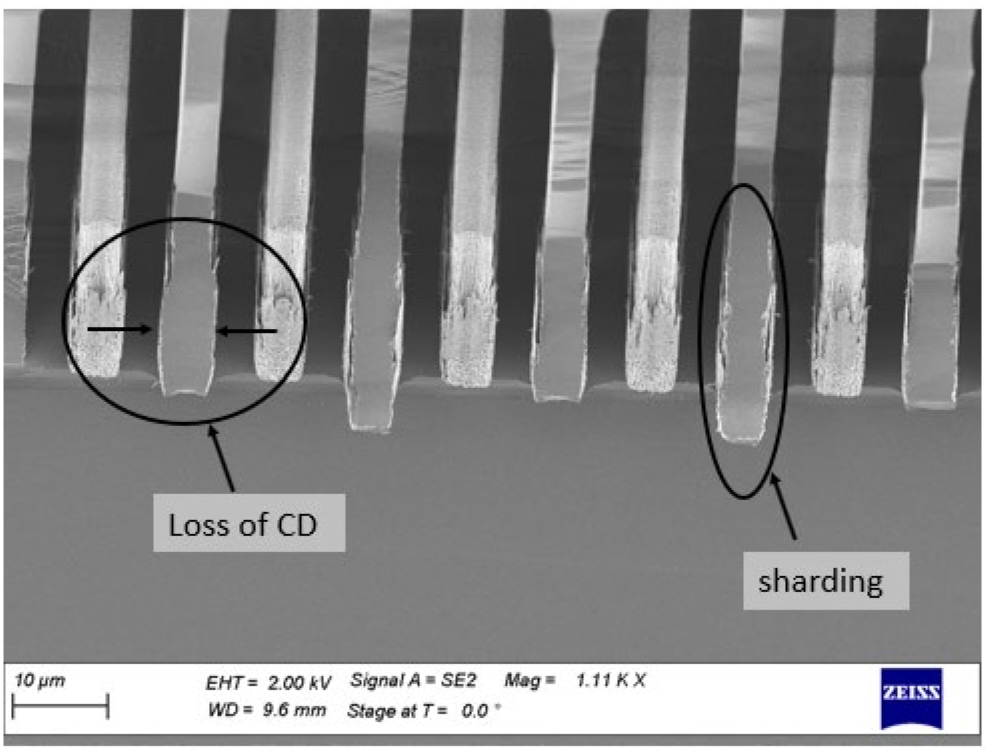

Figure 2.4-12. Cross-sectional SEM of combs for the initial landing etch showing regions of sharding (i.e., shards of silicon separating from the bottom of the combs) and loss of CD.

The regions depicted in Figure 2.4-12 proved detrimental to the yield of functional gyroscopes. The vapor hydrofluoric acid release step caused silicon shards to short the comb's gap between the rotor and stator. Each comb transducer per die has signal routing and if there is a single shorted region, the die is identified as defective.

With the assistance and coordination of L3Harris ARL cleanroom users, the loss of CD and silicon sharding was investigated through several parallel experiments. L3Harris users had structures with similar aspect ratios as the gyroscope presented in this study and were, therefore, using the author's bulk and landing etch. L3Harris conducted a series of experiments modifying polymer deposition time, etch A time, etch A voltage, and chuck helium cooling flow rate. The results of their six different experiments, with permission from L3Harris, are shown in Figure 2.4-13. The only image that revealed any improvement in the etch, "Wafer 8" (bottom right), saw the etch A time increased from 3.5 s to 4.5 s.

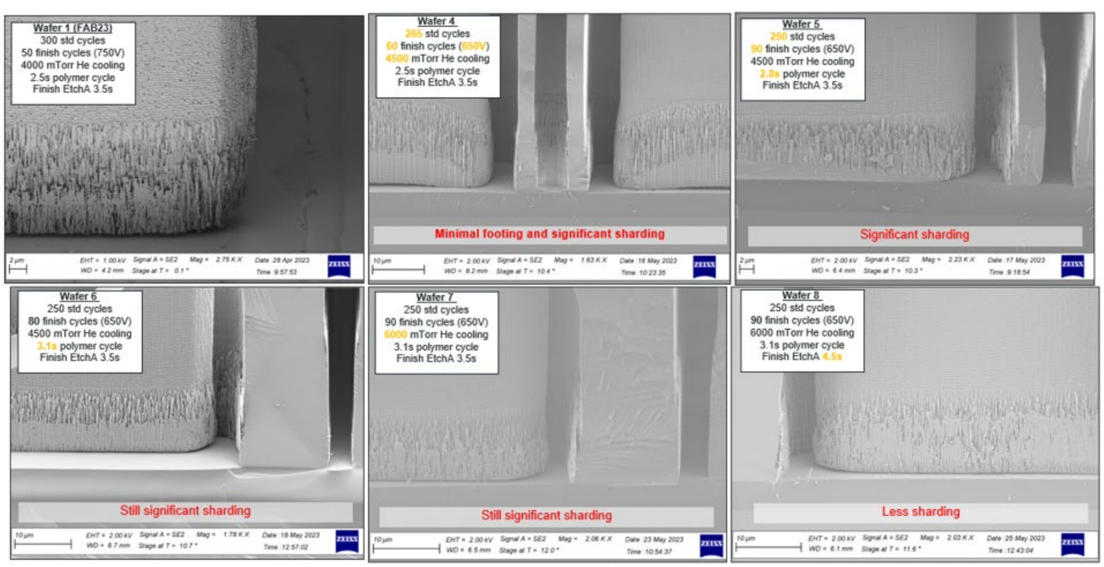

Figure 2.4-13. Six SEM cross-sectional images of L3Harris structures with similar aspect as the gyroscope presented in this thesis. The parameter changed is highlighted in yellow font. The bottom right image of Wafer 8 is the only result that showed any improvement.

Simultaneous to the L3Harris experiments, the author questioned why the etch was behaving differently. 'Waveform 2' significantly reduced notching relative to 'Waveform 1,' used during the bulk etch. However, the power associated with 'Waveform 2' was not intuitive and no guidance was provided by PlasmaTherm on its change. 'Waveform 2' duty cycles the 100 kHz frequency by 25%, meaning it's on for only 25% of the time, effectively reducing its power by a factor of 4. The source power of 'Waveform 2' is equivalent to $\frac{V^2}{|Z|}$, where V is voltage and Z is source impedance. As source impedance ranges between 2-5 kOhm and remains unchanged for both the bulk and landing etch, to accommodate the 25% duty cycle, the source voltage needs to be increased by a factor of 2. The bulk etch A uses a 650 V source bias and increasing it to 1300 V is not recommended. Both PlasmaTherm and the user manual advise against exceeding a 1000 V etch A bias voltage.

To maintain the balance between deposition and etch A, deposition time was reduced from 2.5 s to 2.2 s and etch A bias was increased from 650 V to 1000 V. Following the results of the experiments shown in Figure 2.4-13, where no grassing was seen with an increase in deposition time, deposition time was also morphed from 2.2 s to 3.5 s. Morphing the deposition time allows for increased polymer passivation and protection at the buried oxide interface. Figure 2.4-14 presents a cross-section SEM image of the comb transducer and compares the 1000 V etch with and without the polymer deposition morph. Evidently, the image on the right has smoother features. Figure 2.4-15 is another cross-sectional image of the final morphed landing etch. Minimal notching is observed and although the transition region where the bulk etch ends and the landing etch begins is apparent, this region does not affect the wafer yield.

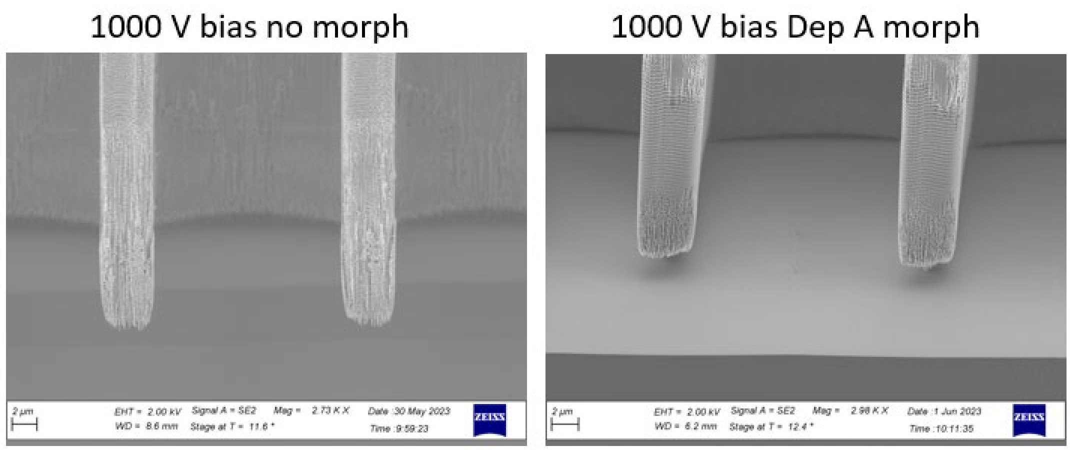

Figure 2.4-14. Cross-sectional SEMs of comb transducer with 1000 V bias on etch A. On the left is without morphing the polymer deposition time and on the right is with morphing. Both etches experienced too many etch cycles resulting in “released-like” combs.

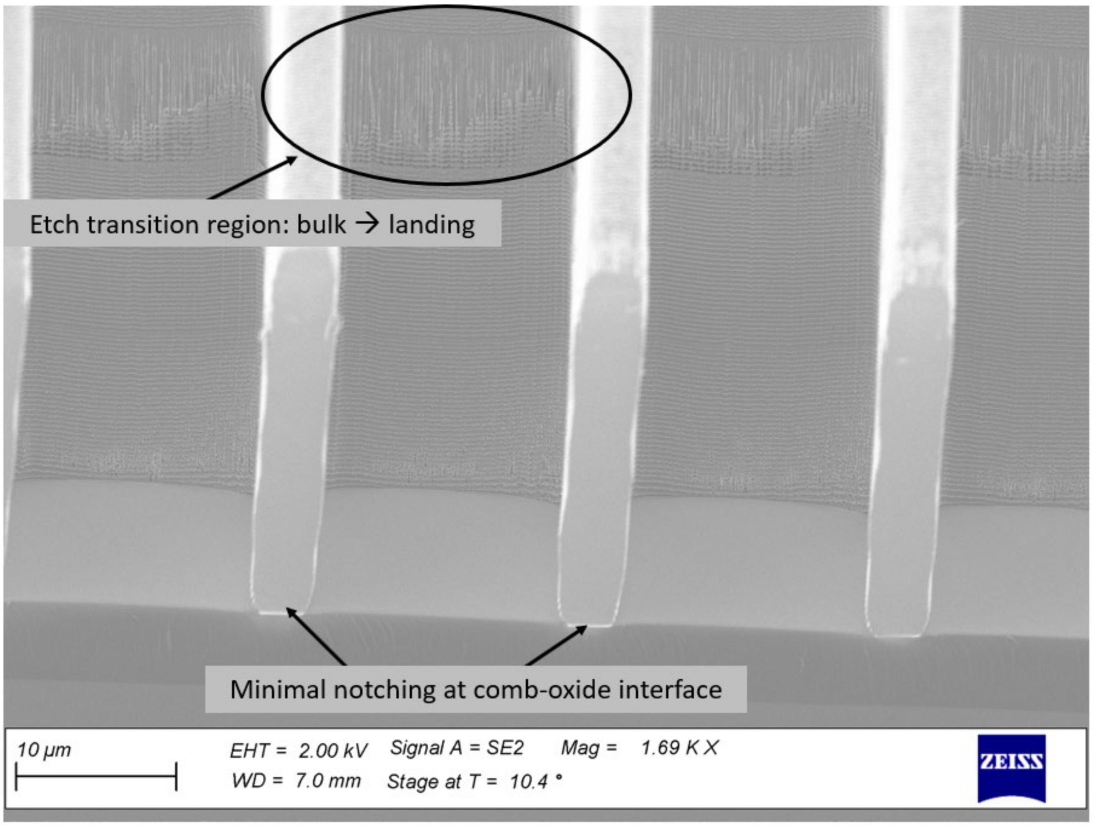

Figure 2.4-15. Cross-sectional SEM of comb transducers illustrated minimal notching the at the comb-buried-oxide interface. The etch transition region where the bulk etch end and the landing etch begins is apparent but not problematic.

The morphed bulk and landing etch process of record recipe is listed in Table 2-4 detailing all process parameters necessary for replication. The author, once again, warns that replicating this recipe will most likely not create the same results as the presented SEMs.

TABLE 2-4. PROCESS OF RECORD FOR ETCHING A 150 MM SILICON WAFER WITH CRITICAL DIMENSIONS OF 5, 15, 20, 40 μm.

RK_FAT_40-1 DSE Morph + ARDE SOI Finish cold — P10111 ARL

ESC Voltage: 800 V
Helium Pressure: 6,000.0 mTorr

1) < Initial >
2) < Chuck >
3) stab
4) ignition
5) Dep
6) Etch A
7) Etch B
8) Loop 225 times
9) Temp Step
10) Evac Step
11) stab
12) Dep
13) Etch A
14) Etch B
15) Loop 80 times
16) Temp Step
17) Evac Step
18) < Dechuck >
19) < End >

	1. < Initial >	2. < Chuck >	3. stab	4. ignition	5. Dep	6. Etch A	7. Etch B	8. Loop to 5	9. Temp Step	10. Evac Step	11. stab	12. Dep
Duration	0:10.0		0:15.0	0:05.0	0:01.5 ▶ 0:02.5 § 0.5	0:01.5 ▶ 0:03.5 § 0.5	0:02.0	225 Iter.		20:00.0	0:10.0	0:02.2 ▶ 0:03.5 § 0.5
Spool	175.0								175.0			
Lid	150.0								150.0			
Liner	70.0								70.0			
Electrode	5.0								1.0			
Pressure	1.0	20.0	20.0	20.0	25.0	25.0	50.0			1.0	25.0	25.0
C4F8		0.0	150.0	150.0	150.0	▼ 150.0	▼ 150.0				▼ 150.0	150.0
SF6		0.0	▼ 200.0	▼ 150.0	▼ 150.0	150.0	150.0				▼ 150.0	▼ 150.0
Ar		20.0	30.0	30.0	30.0	30.0	30.0				30.0	30.0
Bias		0	0	1,000	10	650	10				10	10
ICP		0	0	1,500	1,500	1,000	2,000				1,500	1,500
Mode		Default	Manual	Auto	Hold	Hold	Hold				Hold	Hold
Load			50.0									
Tune			74.0									
N/A		0	0	0	0	0	0				0	0

	13. Etch A	14. Etch B	15. Loop to 12	16. Temp Step	17. Evac Step	18. < Dechuck >	19. < End >
Duration	0:03.5	0:01.0	80 Iter.		10:00.0		2:10.0
Spool				175.0			
Lid				150.0			
Liner				70.0			
Electrode				5.0			
Pressure	25.0	50.0			1.0	20.0	1.0
C4F8	▼ 150.0	▼ 150.0				▼ 0.0	
SF6	150.0	150.0				▼ 0.0	
Ar	30.0	30.0				50.0	
Bias	1,000	10				0	
ICP	1,000	2,000				0	
Mode	Hold	Hold				Auto	
Load							
Tune							
N/A	0	0				0	

2.4.4 *Deep Reactive Ion Etching – final note.*

The development of the bulk and landing etches, as detailed in sections 2.4.2 and 2.4.3, accounted for a significant portion of the author's time. Some critical observations warrant mention. Firstly, a microscope magnification of 10× or 20× is optimal for determining if the silicon DRIE has reached the buried oxide. Figure 2.4-16 visually depicts what silicon etch regions appear like as they start to clear. The oxide appears white, and the dark regions adjacent to the white areas signify the remaining silicon in the etch gap.

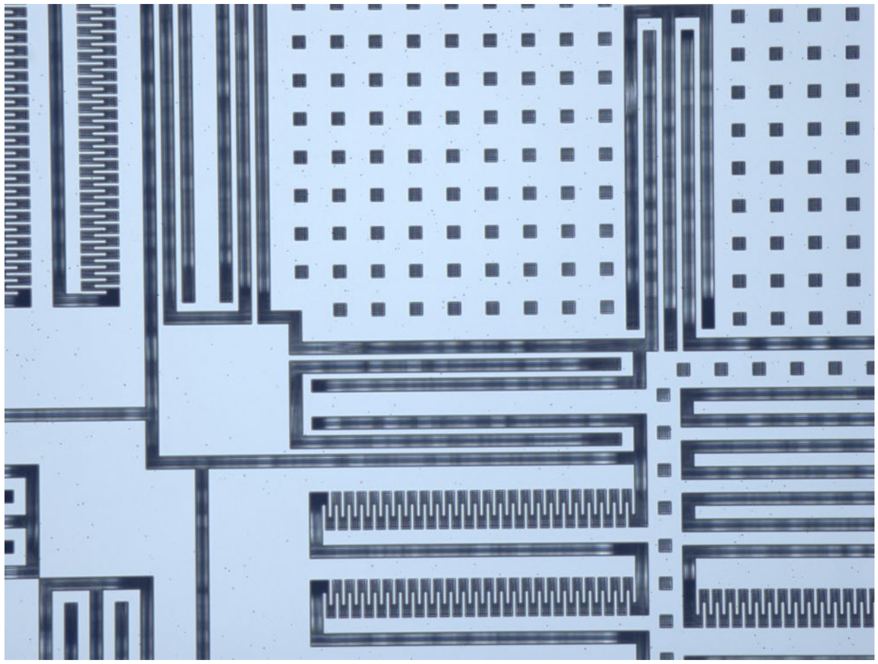

Figure 2.4-16. Etch regions show dark and light areas indicating that the silicon etch is not complete but quite close. Optical magnification 10×.

Another discovered peculiarity is the time-dependent reticulation of the photoresist. Megaposit SPR220, which is used in this context, undergoes reticulation in the PlasmaTherm Versaline tool a few days post-development. This process induces waviness in the photoresist protective layer, consequently impacting the edge fidelity of the defined silicon etch trenches. Reticulation does not occur if DRIE is undertaken immediately following the development of the SPR220. *Figure 2.4-17* depicts the waviness of photoresist reticulation occurring after bulk etch DRIE processing.

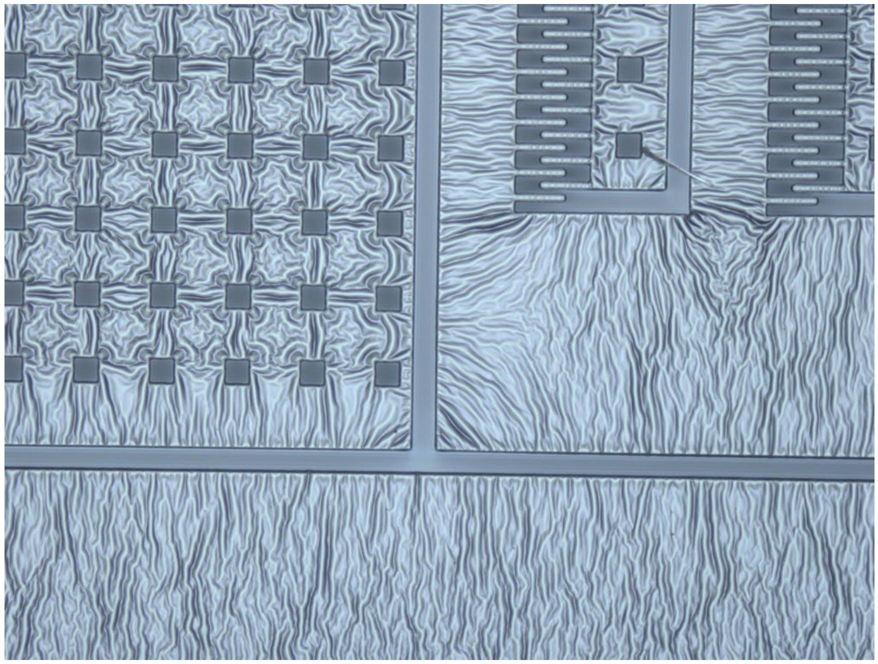

Figure 2.4-17. SPR220 photoresist reticulation seen after DRIE. The SPR220 was developed a few days before DRIE. The excess heat from DRIE induces photoresist waviness and wrinkles which is commonly referred to as reticulation. Reticulation will impact DRIE etch trench edge fidelity.

There are three last essential points to note about DRIE: i) avoid leaving any metal exposed during DRIE, ii) deposition of an edge protect alumina, and iii) understand that dummy silicon wafers etch differently than silicon-on-insulator (SOI) wafers. Metal exposed to DRIE will combine with the C_4F_8 passivation polymer and harden. Specific etchants like EKC265/270 and Dynastrip DL9150 are designed to assist in stripping DRIE residue, however, they are quite hazardous and necessitate closed-system baths. Removing the edge bead removal steps during backside and frontside metal, creates a metal-free wafer edge, further minimizes any changes of metal exposure to the etch.

Wafer handling generates particulates that can subsequently fall into DRIE trenches. The deposition of an alumina edge bead protect improves yield by protecting the wafer's edge during DRIE while also covering any residual metal due to DRIE photolithography precision edge bead removal. Subsequent edge particulates generated are reduced during handling and improves die yield. Special fixturing in typical wafer metal evaporators may be required to deposit an alumina on the edge bead.

Lastly, etch rates and characteristics significantly differ between silicon wafers and SOI wafers. The buried oxide disrupts the heat exchange process from the wafer to the chuck's helium cooling. Higher silicon wafer temperatures reduce the polymer deposition rate and accelerate the wafer's etching process.

Chapter 3: Vacuum Packaging

Quality factor in Chapter 1.5 has been presented a mechanism that if increased will improve MEMS CVG performance. Vacuum packaging is required to remove *Q* degradation sources associated with viscous damping loss mechanism, namely gaseous components of air. Surface contaminates also create *Q* degradation due to frictional losses at the surface and vacuum packaging high temperature bakes tend to outgas surface contaminates. The vacuum packaging work presented has effectively reduce vacuum packaging pressure to state-of-the-art levels for leadless ceramic chip carrying physics packages. This improves high-performance MEMS CVGs and has applications in chip-scale atomic clocks where fractional frequency stabilities below 10^{-12} are required [48].

This chapter aims to mitigate the loss mechanisms associated with $Q_{vicious}$ and $Q_{surface}$. Vacuum packaging of MEMS CVGs is a necessary final production step for high-performance sensors, chip scale atomic clocks, and quantum systems. Vacuum packaging, often incorporating non-evaporable getters (NEG), is a steadily advancing field in MEMS gyroscopes, accelerometers, micromirror displays, RF MEMS, and microbolometers. It is essential for high-performance devices, where high-quality factors, low Brownian noise, and thermal isolation are required. Getters are typically used to reach specified base pressures and capture desorbed outgas species from the package surfaces [28]. The use of getters in final production of high-performance devices is essential due to finite gas leak rates and ongoing desorption of gases from package surfaces. However, to minimize getter vacuum packaging pressure, it is first necessary to reduce the getter-less vacuum packaging pressure. Fine-tuning the base pressure for getter-less vacuum packaging is an important step towards achieving minimal and stable packaging pressures. Although necessary for high-performance sensors and physics packages, getters represent an additional cost in both time and money during the sensor R&D cycle and may not be required, depending on the desired vacuum level. This work employs non-evaporable gettered physics package for experimentation and evaluation of the quadruple mass gyroscope (QMG). The QMG quality factor remains sensitive to vacuum pressure greater than 100 micro-torr while getter-less vacuum packaging is limited to low milli-torr of pressure.

3.1 Getter-less Vacuum Packaging of Ceramic Chip Carriers

Vacuum packaging, often involving getters, has evolved as a common practice for devices like MEMS gyroscopes, accelerometers, micromirror displays, RF MEMS, and microbolometers. The vacuum packaging of MEMS sensors is essential for optimal performance, where factors such as high-quality factors, low Brownian noise, and thermal isolation are sought after. Getters are commonly used to achieve desired base pressures by absorbing desorbed outgassing species from the packaging surfaces [28]. For final production devices, getters are essential due to finite gas leak rates and continuous desorption of gases from the packaging surfaces. However, refining the base pressure for getter-free vacuum packaging is a key step towards achieving minimal and stable packaging pressures. Although getters are necessary for production, they add extra costs in terms of time and money during the sensor R&D phase and might not be needed, depending on the desired vacuum level. This dissertation presents both getter-free and non-evaporable getter-based approaches to vacuum packaging. This section focuses on the approach and the ultimate pressure limit of approximately 1 milliTorr for ceramic chip carrier packages.

High-performance MEMS resonant acceleration and rotational sensors necessitate minimal mechanical and electrical damping mechanisms. To optimize the quality factor and sensitivity of a MEMS sensor, viscous damping mechanisms, such as Couette and squeeze-film damping, must be minimized, which requires low vacuum pressures. Figure 3.1-1 illustrates the relationship between the Knudsen number (the ratio of the mean free path of gas molecules to a characteristic length of the MEMS sensor) and the Q factor dependence of a MEMS resonator. The Q factor of most MEMS no longer depends on viscous damping and is limited to other types of damping mechanisms when vacuum pressures fall below 10^{-3} Torr [29]-[30]. This gas damping insensitive pressure inversely scales with MEMS device layer thickness. High-performance MEMS inertial sensors are typically larger and thicker than their commercial-grade counterparts due to their sensitivity requirements and the proportionality to the sensing mass. Once a sufficiently high vacuum is achieved, surface loss, and intrinsic loss mechanisms, such as thermal elastic dissipation and Akhiezer damping, become the dominant damping mechanisms. Akhiezer damping results from heat flow between different phonon modes and has a relatively minor effect on silicon MEMS at low frequencies [27]. Ideally, stable long-term vacuum packaging pressures below 1 millitorr are necessary for many high-performance

MEMS resonant sensors, due to high aspect ratio device layers, micron motion, and low kHz operational frequencies.

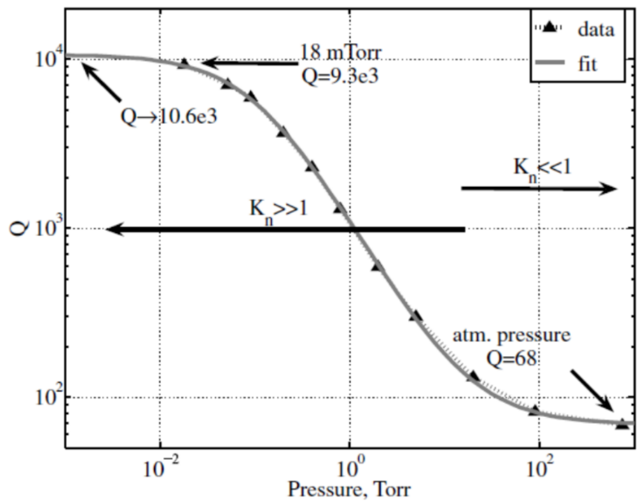

Figure 3.1-1. *Q* factor as a function of pressure for in-phase mode of MEMS resonator. Courtesy of Alexander Trusov [17]. Damping due to viscous effects dominate at pressures above 10 millitorr.

3.1.1 Commercial and existing vacuum packaging

Presently, the most advanced getter-free vacuum packaging results reported in literature indicate a value of 0.75 millitorr for custom Kovar packages that employ a vacuum-based weld seal [31]. However, the method used in [31] involves a custom Kovar package and vacuum welder that are not commercially available and are exclusive to their research. Sparks [32] managed to achieve pressures of 1.4 Torr for getter-less packaging pressures. Prikhodko [33] used a similar leadless ceramic chip carrier (LCC) as in this study, but incorporated a custom glass lid. Their work showed that they could achieve getter-less packaging pressures of approximately 1 Torr. Ramesham [28] used a similar ceramic package (pin grid array) as Prikhodko (dual in-line pin), and achieved similar getter-less vacuum pressures.

The commercially available system utilized in the research conducted by Ramesham [28] and Prikhodko [31] is the SST 3150 high vacuum furnace [34]. This system features a stationary single base-plate heater, with a movable graphite fixture positioned above it. This fixture is designed to hold chip carrier package, usually in an upside-down orientation. *Figure 3.1-2*(a) illustrates a common method for vacuum packaging MEMS sensors in LCC with getter activation. Some limitations associated with this method include the small thermal isolation gap, the risk of losing the preform attachment as it's suspended, and the restriction of being able to heat and independently bake only the lower base plate, commonly reserved only for the Kovar lid.

3.1.2 Custom vacuum packaging system

As noted earlier, a key limitation of the vacuum packaging processes utilized in [28] and [31] lies in the inverted approach, in which the ceramic chip carrier with a soldered sensor die attach is suspended upside down with a gold tin (80/20) preform affixed to it. The gold tin possesses a eutectic point around 280°C, causing the preform to soften and sag at lower temperatures. Consequently, bakeout temperatures near the eutectic point are unachievable due to preform deformation, loss of attachment, and the risks of sensor die attach reflow.

In response to these challenges, a custom high vacuum packaging furnace was developed. This was a collaborative effort between the author, researchers at the US Army Research Laboratory (ARL), and the Kurt J. Lesker Company [35]. The furnace features both top and bottom heaters, a 12" separation between the top and bottom platens, a liquid-cooled isolator, three integrated ports for residual gas analysis (RGA), and a cryogenic trap in line with a turbo pump. The vacuum packaging tool's exterior and interior are shown in Figure 3.1-3.

This innovative configuration allows for a lid (with or without a getter) to be placed on the top platen and a leadless ceramic chip carrier (LCC) with preform on the bottom platen. As a result, higher bake-out temperatures can be achieved without the risk of the preform sagging under gravity or loss of attachment. *Figure 3.1-2*(b) illustrates the setup of this custom high-vacuum packaging furnace designed specifically for MEMS vacuum packaging.

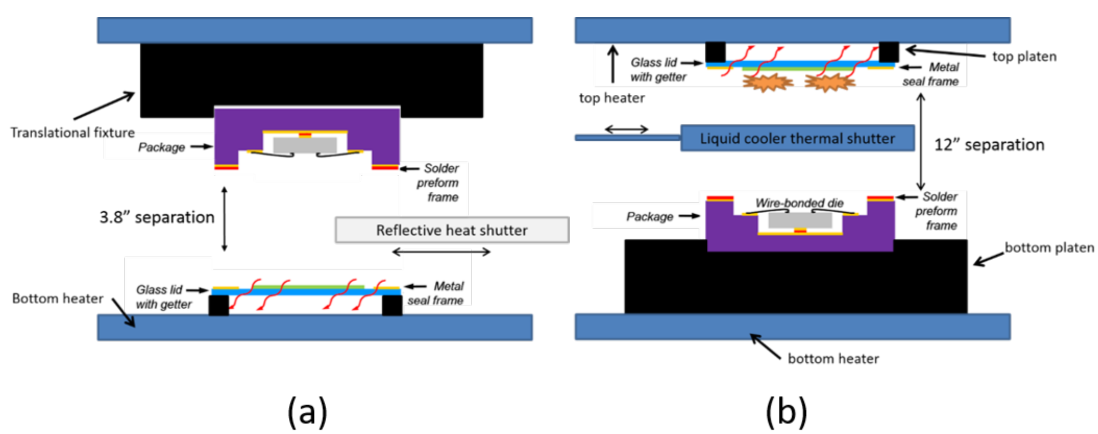

Figure 3.1-2 Cross-section of vacuum packaging methodologies: (a) previously reported approaches in references [2-6] (b) new approach developed in [84]. Limitations of (a) are single bottom heater, small separation distance between platens, and the upside-down suspension of the packaged physics. (b) addresses the limitations of (a) with a 12" platen separation distance, top and bottom platen heaters, and a liquid cooled thermal isolation shutter.

Figure 3.1-3. Custom high vacuum packaging furnace developed as collaborative effort between the author, researchers at the US Army Research Laboratory (ARL), and the Kurt J. Lesker Company.

3.1.3 Vacuum package pressure measurements

Commercially available MEMS Pirani pressure gauges from Posifa Microsystems [36] were packaged in a 44-pin leadless ceramic chip carrier, specifically the Spectrum Semi LCC04438 model. Each package incorporated two Pirani sensors, which were wedge wirebonded to the package and die-attached using Kapton tape. While Kapton tape is known to outgas significantly, it was identified as the most suitable adhesive for die attachment compared to other adhesives and glues. The pressure sensors did not include backside metallization, which made solder die attachment challenging.

The use of off-the-shelf Pirani gauges facilitates rapid experimental iterations. The general experimental process flow is as follows: a) attach with Kapton tape and wirebond Pirani sensors, b) check for electrical connectivity, c) pre-bake at a chosen temperature and time, d) implement the high vacuum furnace packaging process, e) record package pressure sensor voltage values when the package reaches a stable ambient temperature, and finally f) open the packages, place them in a pressure-controlled vacuum chamber, and record the vacuum pressure corresponding to the packaged pressure voltage value. An example Pirani sensor superimposed onto an LCC00438 chip carrier is shown in Figure 3.1-4 highlighting the four wirebonding connection points for Pirani bridge measurement and reference temperature compensation.

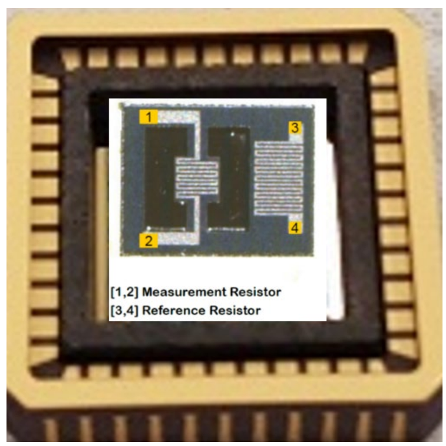

Figure 3.1-4 Example Posifa Pirani pressure sensor in a leadless ceramic chip carrier package prior to vacuum package. The Pirani sensor has two resistors: 1) to measure the Pirani effect by heating the suspended bridge and 2) a reference measurement resistor allowing for temperature compensation.

3.1.4 Getter-less vacuum package pressure, leak rate and vacuum stability

The voltage value of the vacuum packaged Pirani pressure sensors is measured by applying a constant current of 4-7 mA (depending on the vacuum package level) across a suspended resistive heater, namely the Pirani sensor shown in Figure 3.1-4. The vacuum packaged pressure value is measured in the vacuum chamber setup with the chamber lid removed to account for any resistance in the line and connections that could affect the bridge voltage value. After allowing a few minutes for thermal stabilization, the voltage across the bridge is recorded. The temperature compensation resistor shown in Figure 3.1-4 is not used in a Wheatstone bridge-like setup and temperatures effects have been ignored. The package lid is manually unsealed exposing the Pirani sensor to the atmosphere, placed in a vacuum chamber, and depressurized. During the pump-down phase, current is applied to the sensor, and the pressure at both the vacuum chamber and turbo connection is monitored. Typically, these two chamber pressure sensors differ by 10-20 millitorr and their readings are averaged to obtain the final value. Once the Pirani sensor voltage nears the packaged value, a manual chamber leak valve is adjusted to stabilize the chamber pressure.

The development of a getter-less vacuum packaging process was primarily motivated by two factors: a) reduced material costs during development when omitting a getter, and b) setting the lowest possible getter-less package base pressures as an ideal starting point for getter recipe development. Extensive experimentation, as discussed next, has revealed that the getter-less vacuum packaging pressure is predominantly determined by the pre-vacuum sealing bakeout recipe.

Previous studies [28], [38] proposed bakeout time and temperature recipes that varied significantly, from 125 °C for 24 hours [38], to 250 °C for 168 hours, and even 400 °C for 1 hour. We attempted these three bakeout recipes; and the 125 °C and 250 °C recipes failed to achieve a seal during packaging. This was due to an internal package pressure increase during the vacuum sealing step that led to gas pressure buildup and subsequent package outgassing, resulting in vacuum-compromising voids in the eutectic AuSn preform seal. This outgassing was visually confirmed through the process chamber window in the vacuum packaging tool. The 400 °C bake for 1 hour, however, successfully produced sealed vacuum packages, but requires the preform be removed from the LCC surface due to the eutectic temperature being exceeded during pre-bake.

Since >400 °C temperatures are required to achieve a sealed vacuum, the following experiments help determine how long a sufficient pre-vacuum seal bake out is necessary. Figure 3.1-5 depicts residual gas analyzer (RGA) charts during bakeouts at 450 °C for 2.5 hours and 5 hours. Several packages followed either recipe and the results are reported in *Table 3-1*. RGA partial pressure appeared to stabilize at 5 hours, thus this duration was chosen. However, one drawback of high-temperature bakes is the risk of metallic diffusion on MEMS sensors. ARL internally developed MEMS sensor pad gold metallization was found to diffuse through the chrome/platinum adhesion layer and diffusion barriers into the device layer silicon. Moreover, if gold wirebonds penetrate through the metallization to the silicon substrate, the silicon-gold eutectic point of 370 °C can cause the wirebonds to reflow, wick, and ultimately create an open circuit condition. A third recipe was investigated, maintaining the packages just below the silicon-gold eutectic temperature for 24 hours. These results are also presented in *Table 3-1*.

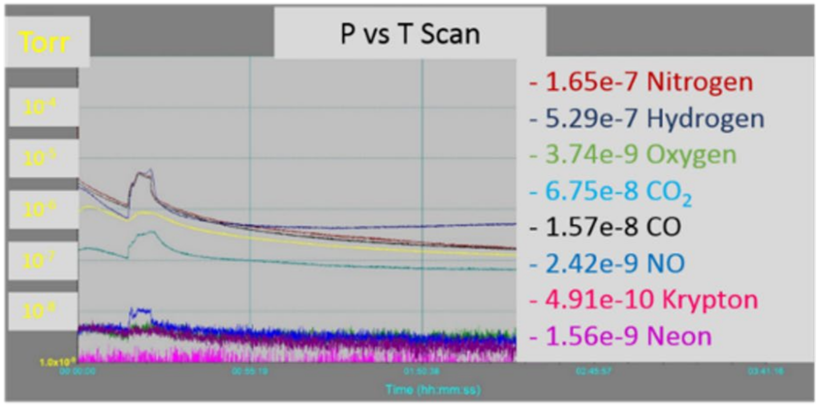

(a)

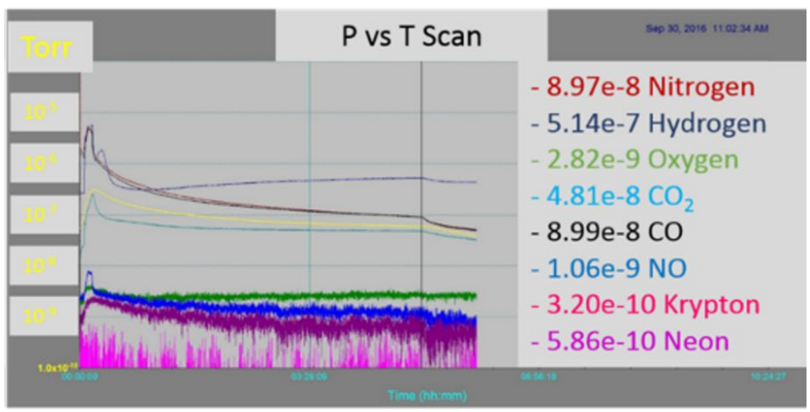

(b)

Figure 3.1-5. Residual gas analyzer comparison of (a) 2.5-hour bake and (b) 5-hour bake at 450 °C. Partial pressure values plotted in each legend represent the amount of gas present in the vacuum chamber after each bake. N_2, CO, CO_2, and H_2O are all reduced with the 5-hour bake.

A series of vacuum packaging runs without pre-bakeouts were conducted to ascertain the importance of pre-bakeout of the Kapton tape. The resulting packaging pressures were two orders of magnitude higher than those obtained from baking out packages with Pirani sensors and Kapton tape die attachment. This clearly underscores the need for lengthy, high-temperature bakeouts.

Lastly, a vacuum furnace sealing recipe was formulated to minimize process chamber base pressures during package sealing. This involved over four days of multiple graphite heater outgassing cycles, as well as a 250 °C bake for two days. During each individual heater outgasses cycle, the process chamber pressure would increase with heater temperature. The corresponding pressure peak was monitored over several heater outgassing cycles until it stabilized to a minimal value. Consequently, the base pressure during vacuum sealing never exceeded 5×10^{-7} Torr. However, a 4-day process is impractical even in a laboratory setting. Therefore, tests were conducted to evaluate the necessity of a 4-day vacuum sealing recipe. The results in Table *3-1* suggest that the actual vacuum sealing recipe has little impact on the final getter-less vacuum sealed pressure. The optimized getter-less packaging recipe requires only a few hours, as opposed to the 4-day period initially used to achieve tool base pressure and subsequent sealing.

TABLE 3-1. GETTER-LESS VACUUM PACKAGING RESULTS.

Bake-out Recipe	Pressure (milli-torr)	1-σ (milli-torr)
2.5 hour pre bake-out at 450 °C – 4 day bake then seal	22	12
5.0 hour pre bake-out at 450 °C – 4 day bake then seal	12	5
24 hours at 370 °C – 4 day bake then seal	57[a]	n/a
5.0 hour pre bake-out, immediate seal, with Kapton tape	3450[a]	n/a
5.0 hour pre bake-out, immediate seal, no Kapton tape	37[a]	n/a

[a] only one data point

3.2 Non-evaporable getter Vacuum Packaging of Ceramic Chip Carriers

The vacuum packaging of MEMS sensors is vital for high performance where elevated quality factors, diminished Brownian noise, and thermal isolation are required. Non-evaporable getters (NEG) are commonly employed in the most sensitive, high-performance MEMS sensors, to achieve sensor package base pressures and to "catch" outgassed species desorbing from the package's surfaces [28]. The application of NEGs in vacuum packaging has been progressively adapted for MEMS gyroscopes, accelerometers, micromirror displays, RF MEMS, and microbolometers. The utilization of getters in final production high performance devices is crucial to maintaining quality factor performance specifications due to the pressure dependence of the Q factor, along with the package's finite gas leak rates and steady desorption of gases from the package surfaces. To ensure optimal Q by reducing viscous loss mechanism, quadruple mass gyroscope presented in Chapter 1, necessitates the use of NEG vacuum packaging.

Minimizing base pressure for getter-less vacuum packaging is a necessary and fundamental step toward attaining optimal and stable NEG packaging pressures. The optimization of getter-less vacuum packaging was discussed in section 3 and in [37]. The subsequent NEG experiments presented start with the getter-less recipe and incorporate a getter activation step post vacuum seal.

High-performance MEMS resonant acceleration and rotational sensors demand minimal mechanical and electrical damping mechanisms. To maximize the Q-factor for a MEMS sensor, the removal of viscous damping mechanisms such as Couette and squeeze-film damping requires low vacuum pressures. *Figure 3.1-1* illustrates the relationship between the Knudsen number, which is the ratio of the mean free path of gas molecules to a characteristic length of the MEMS sensor, and the Q-factor's dependence. In most MEMS systems, the *Q* factor [39]-[40] becomes independent of viscous damping at high Knudsen numbers and instead is limited by other types of damping mechanisms when vacuum pressures drop below 10^{-3} Torr. Anchor and surface loss, along with intrinsic damping sources such as thermal elastic dissipation and Akheizer damping [27], become the dominant damping mechanisms. Ideally, for high-performance MEMS resonant sensors, long-term vacuum packaging pressures need to be consistently maintained below 10^{-4} Torr.

3.2.1 Commercial and existing NEG vacuum packaging

The most advanced published NEG-activated vacuum packaging results came from Asadian [46], who showcased a MEMS vibratory gyroscope with a Q-factor over 2 million. While they claimed micro-torr vacuum levels, they did not verify this with a calibrated vacuum gauge measurement. Prepackaged *Q* measurements showed values near 500,000; however, vacuum packaged *Q*'s increased by a factor of 4. The prepackaged vacuum chamber pressure vs. *Q* factor measurements indicated a *Q* factor ceiling of 500,000, suggesting that *Q* cannot be substantially increased by reducing pressure below 0.2 millitorr. The data reported in this work contend that a vacuum packaged sensor undergoing long duration, high-temperature bakes in ultra-clean vacuum behaves differently in terms of prepackaged sensor *Q* factor over pressure, compared to prepackaged vacuum chamber measurements.

The commercially available system used in the research by [28], [41], and [46] was the SST 3150 high vacuum furnace [34]. This system features a single base-plate heater that remains stationary, with a movable graphite fixture located above the base plate heater, which holds the sensor packages upside down. Figure 3.1-2(a) illustrates a common method for vacuum packaging MEMS sensors in LCC with getter activation. This approach, however, has some drawbacks, including a small thermal isolation gap and the risk of preform attachment sag and loss due to its suspended position which can lead to detachment.

3.2.2 Kurt J. Lesker customized vacuum packaging tool

As previously mentioned, a limitation of the vacuum packaging processes employed in the research [28], [41], and [46] is the inverted approach, where the ceramic chip carrier with a soldered sensor die attach is suspended upside down with a tack-welded AuSn (80/20) preform. The 80/20 AuSn has a eutectic point around 280 °C, and the sealing preform begins to soften and sag at temperatures below this point. Bake-out temperatures near the eutectic point are impracticable due to the risk of preform deformation, attachment loss, and potential sensor die-attach reflow. As highlight in section 3, bakeout is the single most important process step to reduce vacuum packaging pressure.

A custom high vacuum furnace, designed by the US Army Research Laboratory and constructed by Kurt J. Lesker Company [35], addresses these limitations. This furnace incorporates both a top and bottom heater, a 12" separation between the top and bottom platens, a liquid-cooled isolator, three nozzle locations for integrated residual gas analysis (RGA), and a cryogenic trap in-line with a turbo pump.

The innovative design enables a lid, with or without a getter, to be placed on the top platen and a leadless ceramic chip carrier (LCC) to be positioned on the bottom platen. This arrangement facilitates the attainment of higher bake-out temperatures without risking preform sag under gravity or Kovar lid attachment loss. Figure 3.1-2(b) illustrates the setup of this custom high vacuum furnace specifically designed for MEMS vacuum packaging. The preform is situated on the ceramic chip carrier that houses the wirebonded sensor. The large 12" separation between the bottom and top plate along with the liquid cooled thermal shutter allow for near independent platen temperatures during operation.

3.2.3 Getter activation and performance

MEMS quadruple mass gyroscopes (QMG), presented in Chapter 1, were packaged in a 44-pin leadless ceramic chip carrier (LCC), Spectrum Semi LCC04438 model. Each package features a center-mounted 80/20 AuSn die attach to solder the QMGs to the LCC package substrate. The QMGs are wirebonded then released in an ethanol-buffered vaporized hydrofluoric acid solution. The Q factor of anti-phase modal frequencies is recorded using the Zurich Instruments HF2LI lock-in amplifier in a custom vacuum cube chamber before vacuum packaging. The vacuum cube chamber is shown in *Figure 3.2-1*. Given that the Q factors typically exceed 500,000 at frequencies in the 2 kHz region, the ring-down method is used due to the narrow bandwidths needed for the -3 dB method. Following pre-packaging characterization, the sensors undergo a native oxide clean and an optimized 5-hour pre-bake previously detailed in section 3. The vacuum packaging process, executed in the custom Kurt J. Lesker system, shown in Figure 3.1-3, takes 4 days to outgas the heaters and bake out the chamber prior to sealing the LCC. When sealed, the vacuum-packaged QMGs are then allowed a few days to stabilize before initiating *Q* factor measurements.

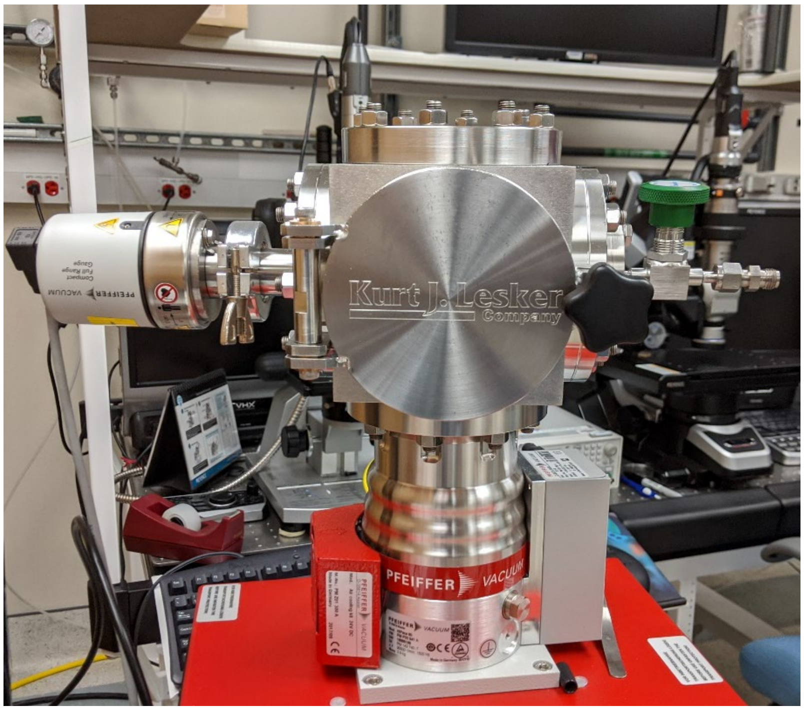

Figure 3.2-1. Custom vacuum cube chamber sitting on top of a Pfeiffer tube pump. Pre-packaged vacuum measures are conducted in this cube due to its three-minute base pressure pump down speed.

Kovar lids are pre-baked using the protocol identified in [37] and sent to SAES Getter for PageLid® NEG deposition with thickness of 2.1 ±0.7 µm. After vacuum chamber characterization, the wirebonded and released QMGs undergo a native oxide strip before initiating the pre-bake using the recipe defined in [37] and section 3. Once the pre-bake is completed, preforms are manually placed on the LCCs and the Kovar lids with deposited NEGs are loaded onto the upper platen. The lower platen houses the LCC, AuSn preform, and the QMG sensor. The tool pumps down, undergoes a series of N_2 purges, and multiple heater outgassing cycles, where high currents are cycled through pyrolytic graphite heaters until a stabilized pressure minimum is reached. After completing the outgassing cycles, the top plate is heated to ~200 °C while the bottom platen is heated to ~265 °C for 48 hours. During the 48-hour bake, the top and bottom platens are separated by a 12” gap, featuring a liquid-cooled thermal shutter acting as a radiative isolator to reduce thermal coupling. SAES Getters advises keeping the getter below 200 °C during baking to prevent premature activation.

The mating and package sealing process begins by turning on the platen heaters at full power. Figure 3.1-5 depicts the lid seal and getter activation steps during this process. The magnified section reveals when the platens' mating occurs and the heaters transition from outgassing H_2 to N_2, CO, and CO_2, as measured by a residual gas analyzer and shown as an overlay in Figure 3.2-2. This is timed to coincide with a local process chamber pressure minimum and is labelled “Platen Mate” in Figure 3.2-2. Upon reaching a platen surface temperature of 310-325 °C, the power is reduced while the getter remains above an activation temperature of 350 °C [37]. This strategy ensures maximum getter sorption rate, capturing only the LCC package species and not activating prematurely and absorbing vacuum chamber species.

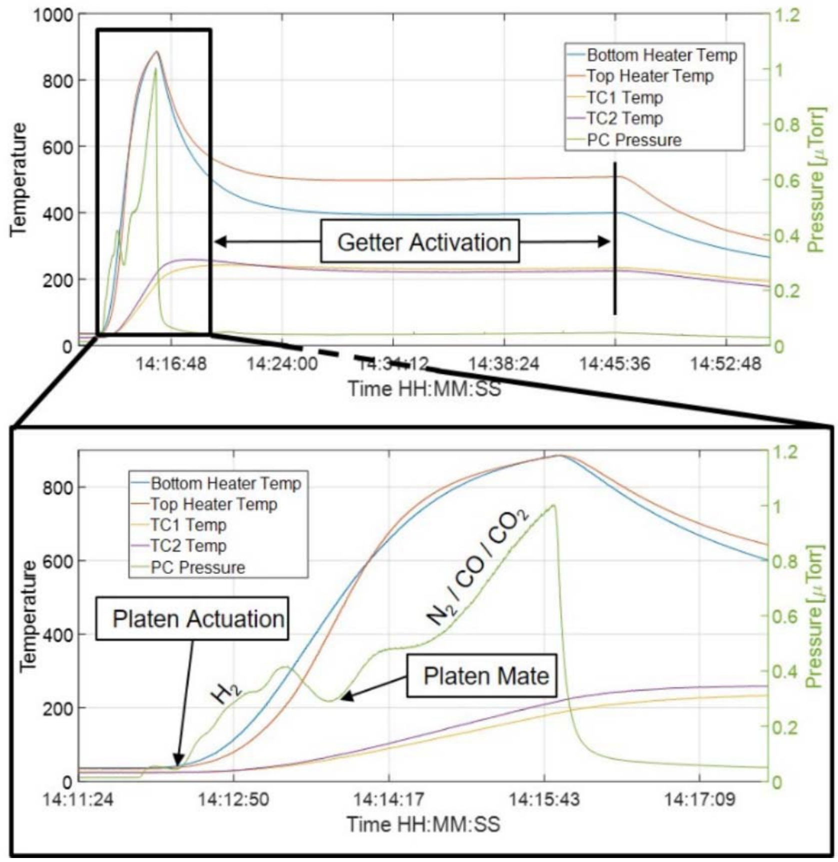

Figure 3.2-2. Lesker vacuum packaging pressure and temperature profile during lid seal. (a) ~45 minute plot during vacuum package lid seal and getter activation plotting chamber pressure, top and bottom heater temperature, and two thermal couple placed near the mated platens. (b) shows a zoomed in look at the start of the package lid seal step where the top and bottom platens heat and actuate to mating. Two spikes in pressure correspond to H_2 outgass of the heaters and subsequent outgassing of $N_2/CO/CO_2$.

3.2.4 Getter vacuum packaging pressure results

The QMGs packaged in the LCCs are soldered to a surface-mount breakout PCB, which includes probe-access holes for shearing off the lid inside the vacuum chamber (this will be highlighted in section 3.2.6). *Q* factor measurements are taken both outside and inside the vacuum chamber before pump-down to ensure consistency. Two independent vacuum gauges, Pfeiffer PKR 251 and Busy Bee PCM301, have determined a vacuum chamber base pressure of 30-47 micro-torr. Reaching the base pressure typically takes a few days. Using the Zurich Instruments HF2LI lock-in amplifier, *Q* factor ring-down measurements were initially performed in the following order: prepackaged vacuum cube (no lid, vacuum cube chamber shown in *Figure 3.2-1*), post-vacuum seal on the lab bench, and then de-lidded in air and re-measured in the vacuum chamber. Figure 3.2-3 illustrates the original packaged Q-factor of 340k, followed by subsequent LCC de-lidding in atmosphere and reinsertion into vacuum chamber for pressure versus Q-factor measurements. An approximate 15-25% change in vacuum-packaged Q-factor is observed when de-lidding the LCC in atmosphere and measuring at vacuum chamber base pressure. A different QMG sensor in Figure 3.2-4 shows a continual decrease of Q-factor over a period of 6.5 days before stabilizing to ~100,000, 7× below its original vacuum packaged Q-factor. This reduction could be due to vacuum chamber contamination adhering to the QMG surface. Figure 3.2-4 also exhibits odd convex *Q* factor behavior over a temperature range from -35 to 215 °C, similarly, observed in [43] micromechanical resonators with silicon oxide. *Q* as a function of temperature of thermal elastic dissipation limited should behave to the $T^{-2.8}$ as discussed in section 4.3.3 and shown in Figure 4.3-2.

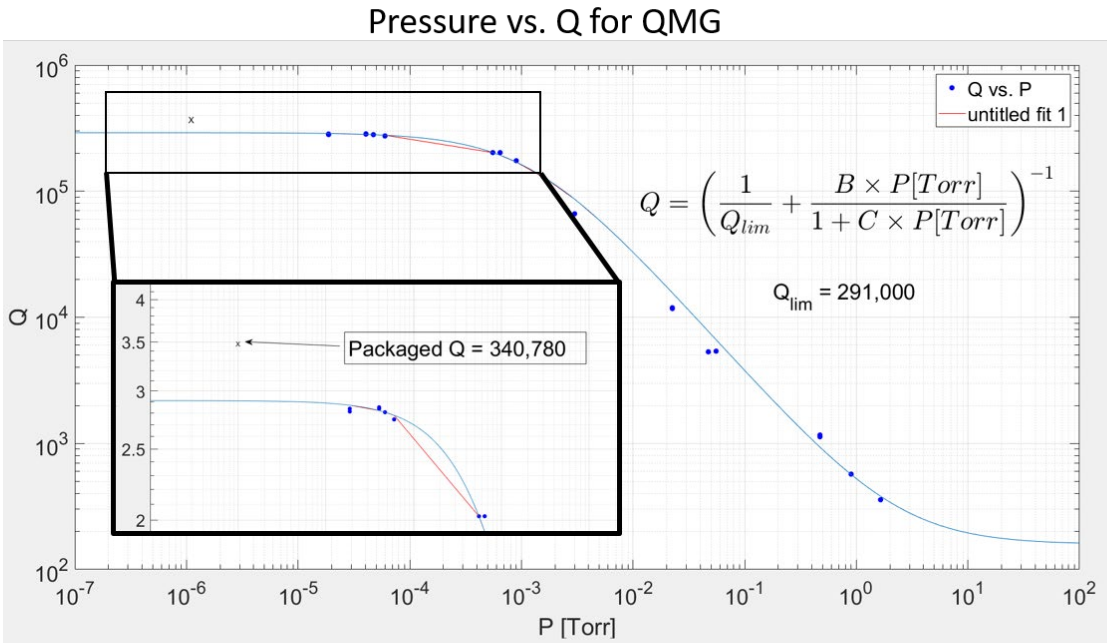

Figure 3.2-3. Quality factor vs. vacuum chamber pressure of a quad mass gyroscope. The "x" marks the vacuum packaged quality factor whereas the blue points are subsequent vacuum chamber measurements with the lid opened initially exposing the quad mass gyroscope to atmosphere prior to vacuum chamber pumpdown.

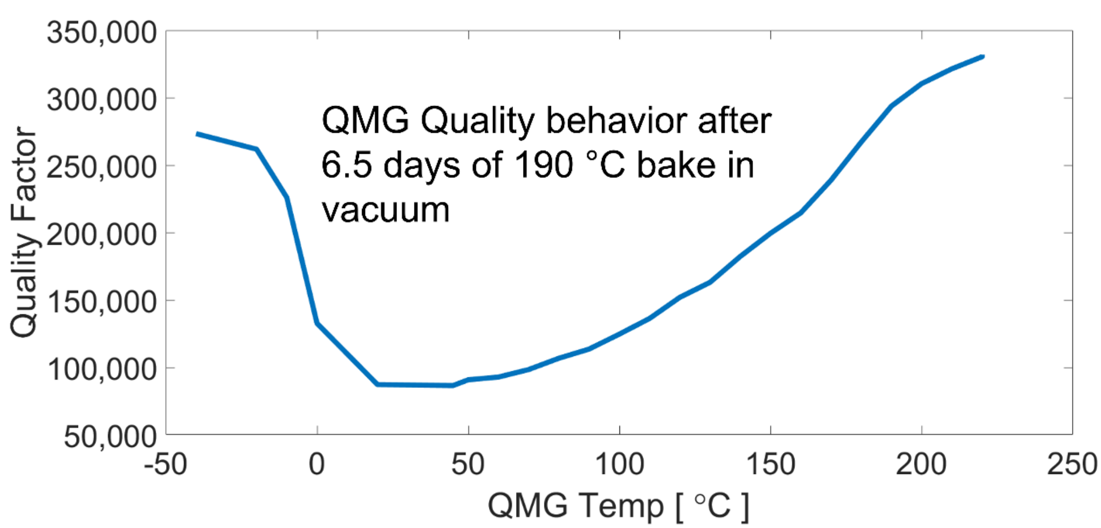

Figure 3.2-4. Convex Q factor behavior over a temperature range of -35 to 215 °C. Q factor has decreased from 775k after exposing to air and slowly decreasing before stabilizing to ~ 100k after 6.5 days in the vacuum chamber. Q vs. temperature measurements were taken when Q stabilized to its lowest value.

3.2.5 Discussion: vacuum package pressure measurement with NEGs

Figure 3.2-3 emphasizes that the Q factor of NEG vacuum-packaged QMG, registering at 340,780, exceeds the limit (Q_{lim}) set by the empirical Q versus pressure function shown in the inset. This phenomenon is observable in all high-Q vacuum-packaged QMGs. Andrei Shkel's group at the University of California, Irvine (UCI) has reported similar vacuum packaging behavior [46]. Figure 3.2-5 indicates the initial vacuum chamber Q at roughly 500,000, followed by the subsequent vacuum-packaged Q after 8 and 24-hour bakes at ~200 °C. The study in [46] primarily focuses on the long-term stability of the packaged Q over 400 days, and does not strive to accurately quantify the pressure of NEG vacuum packaging. When the sensor's Q is measured prior to vacuum packaging in a vacuum chamber, other damping mechanisms such as surface loss, become significant by constraining the Q limit when plotting Q versus pressure (Figure 3.2-3). To accurately replicate the vacuum-packaged Q, the bakeout environment must be duplicated in the vacuum chamber measurement setup. Unfortunately, the setup lacked the thermal capacity to reach 425 °C, and high-temperature ceramic PCBs for signal feedthrough were not utilized.

Surface loss damping due to oxide and contaminants like surface-absorbed hydrocarbons and humidity are noted in [50] contribute significantly to Q reduction. However, in [50], the surface area to volume ratio was substantially larger than that of the QMG flexure, thus a 4× reduction from native oxide growth should not be anticipated. The volumetric surface and friction loss attributable to surface oxide is believed to be much lower for MEMS flexures than for NEMS flexures. The presence of thick surface oxide is typically signaled by a temperature coefficient of frequency (TCF) with convex behavior over temperature [47]. After exposure to the atmosphere and 24-hour bakes, the Q factor was shown to increase after an oxide strip in the vapor HF chamber, indicating that oxide growth may in fact impact Q. During QMG processing, the sensor is briefly exposed to cleanroom atmosphere post native oxide removal. Despite this brief exposure, the sensors are promptly moved to the vacuum packager, native oxide growth occurs instantly. While oxide growth does contribute to surface loss and Q degradation, it is not the dominant mechanism evident in Figure 3.2-3. Anchor loss, as demonstrated in [51], is independent of temperature and not a key driver to increase Q, as shown in Figure 3.2-6. Q due to thermal elastic dissipation (Q_{TED}) decreases with increasing temperature beyond the point where silicon's coefficient of thermal expansion is zero, which is near cryogenic temperatures. Thus, Q_{TED} and Q_{anchor} are ruled out. Q_{gas} does increase with rising temperature but at a rate proportional to $\sqrt{T}$, not quadratically as depicted in Figure 3.2-6. Given that the vacuum chamber was subjected to extended pump-down time with two gauges measuring in the 50 µTorr range, Q_{gas} should not be driving the Q behavior of Figure 3.2-6.

Q behavior similar to Figure 3.2-6 was attributed to surface water and ethanol [45]. Before vacuum packaging, Q factors typically range from 10,000 to 30,000, and a significant boost in Q factor is observed after vacuum packaging. The vapor hydrofluoric acid release and native oxide strip chemistry is buffered with ethanol, which is known to persist on the surface of silicon of vapor hydrofluoric acid treatment. An O_2 plasma RF strip and or a 250 °C hour bakeout is needed after the vapor hydrofluoric acid release.

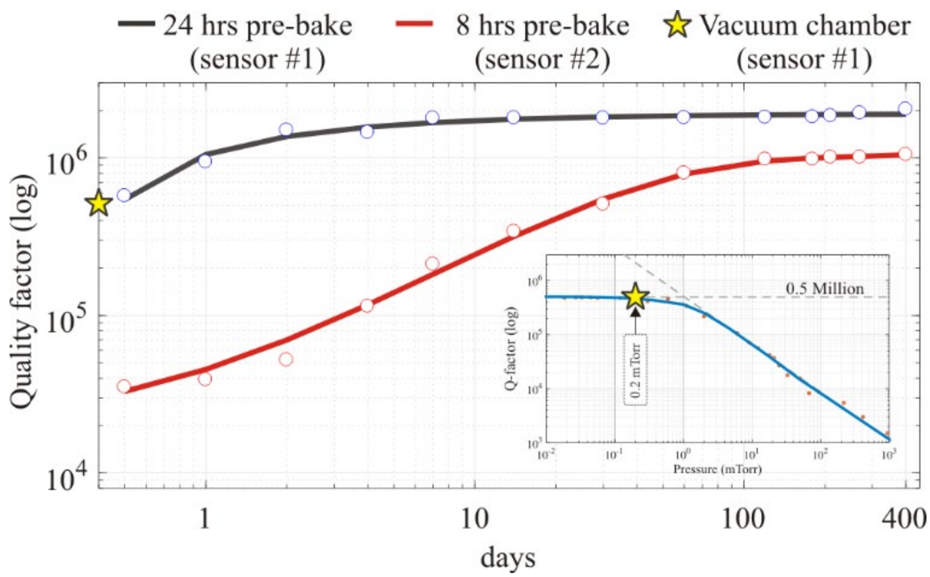

Figure 3.2-5. Andrei's Shkel's group at UCI has shown similar behavior previously shown in Figure 3.2-3. Vacuum packaging with 24 hour 200 °C bakeouts reduce surface loss resulting in higher quality factors for a vacuum packaged resonator compared to one measured in a vacuum chamber[46].

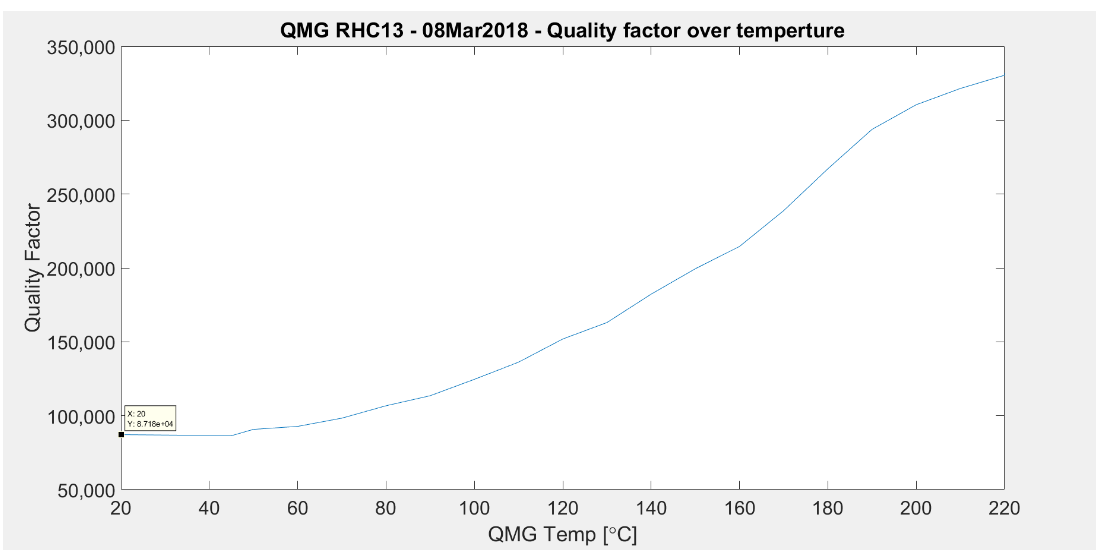

Figure 3.2-6. Quality factor over temperature for quad mass gyroscope, released in vapor hydrofluoric acid and exposed to atmosphere. Measurements were made in a vacuum chamber. Quality factor increases with temperature which is not a typical behavior of silicon resonators [44].

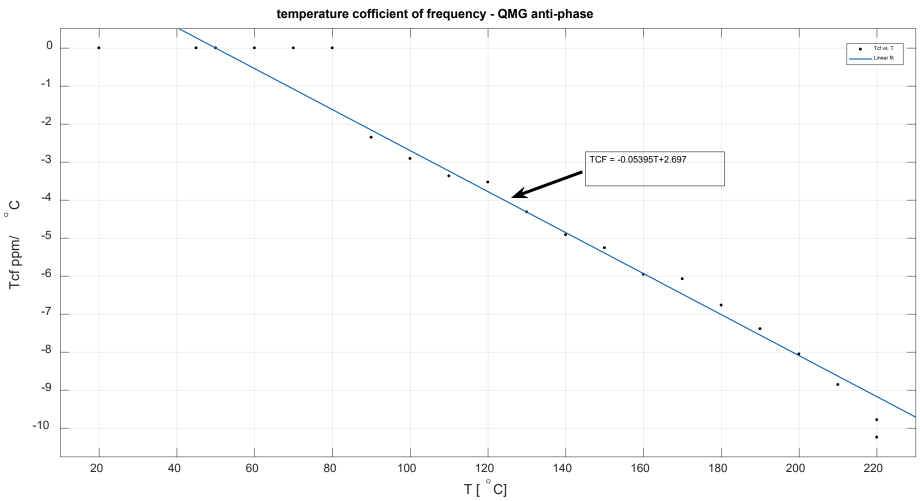

Figure 3.2-7. Temperature coefficient of frequency for QMG when exposed to atmosphere and measured in vacuum. The TcF slope of -5.4 ppm/°C is similar to work published in [47] where the resonator silicon-to-oxide volumetric ratio is 20%.

3.2.6 Experimental verification of vacuum packaged quality factor

Substantial changes in the Q-factor were observed following lid removal as discussed in section 3.2.5. Quality factor vacuum chamber measurements consistently remain at least 2× lower than the NEG vacuum packaged results. Consequently, a special fixture and PCB were designed to remove the lid from the LCCs within the vacuum chamber, mitigating any potential air contaminants that could affect the *Q* factor. Figure 3.2-8 depicts the PCB inside the vacuum chamber, with a probe removing the lid from the vacuum packaged LCC. The evaluated QMG sensor originally had a vacuum packaged *Q* factor of 984,587 (σ = 18,015). After the lid seal was removed, the *Q* factor declined to 906,079, approximately 8% of its original value, at a vacuum chamber pressure of 30-47 micro-torr. By applying a 99.9% confidence interval to the pressure versus *Q* factor curve, one can conservatively assert that the pressure within the getter-activated vacuum-packaged QMG in an LCC is below 1 micro-torr. These values along with the complete Q versus vacuum chamber pressure curve are shown in Figure 3.2-9.

The Kurt J. Lesker vacuum packaging tool, designed to meet the performance specifications required by the Army Research Lab, consistently achieves, and maintains state-of-the-art vacuum packaging pressure. The vacuum packaging bakeout and NEG activation procedures resulted in a pressure of less than 1 micro-torr for leadless ceramic chip carriers. Micro-torr vacuum packaging pressure removes all sources of viscous damping, and Coriolis vibratory gyroscopes with thick device layers (> 100 µm), operating at low frequencies (2-20 kHz) and large amplitudes (>2 µm), will benefit and not be impacted by Q_{gas}. Furthermore, advanced physics packages for chip-scale atomic clocks (CSAC) and other quantum-like systems also necessitate vacuum pressures below 1 micro-torr for low noise performance. Collisional shifts place limits on the vacuum stability required in the atomic beam device. For CSACs, common background gases such as H_2 and He induce collisional shifts and < 7 micro-torr of pressure is needed to achieve fractional frequency stability below 10^{-12} [48].

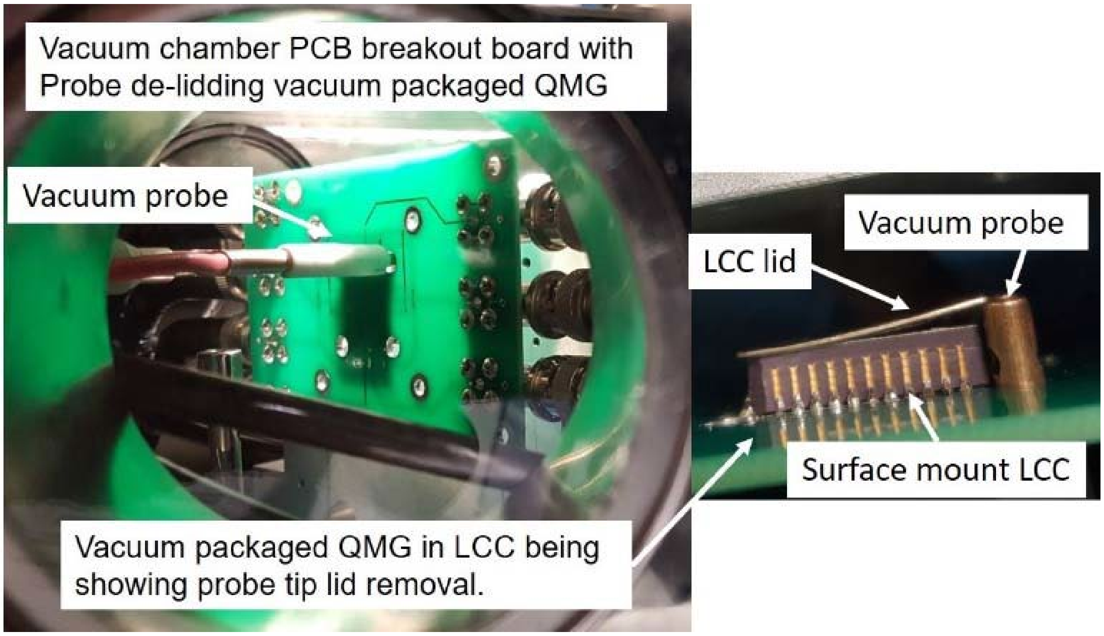

Figure 3.2-8. Vacuum chamber PCB fixture designed to de-lid the vacuum packaged LCC inside a vacuum chamber. This approach allows for vacuum packaged Q measurement by removing any exposure to atmospheric elements like oxygen and water vapor.

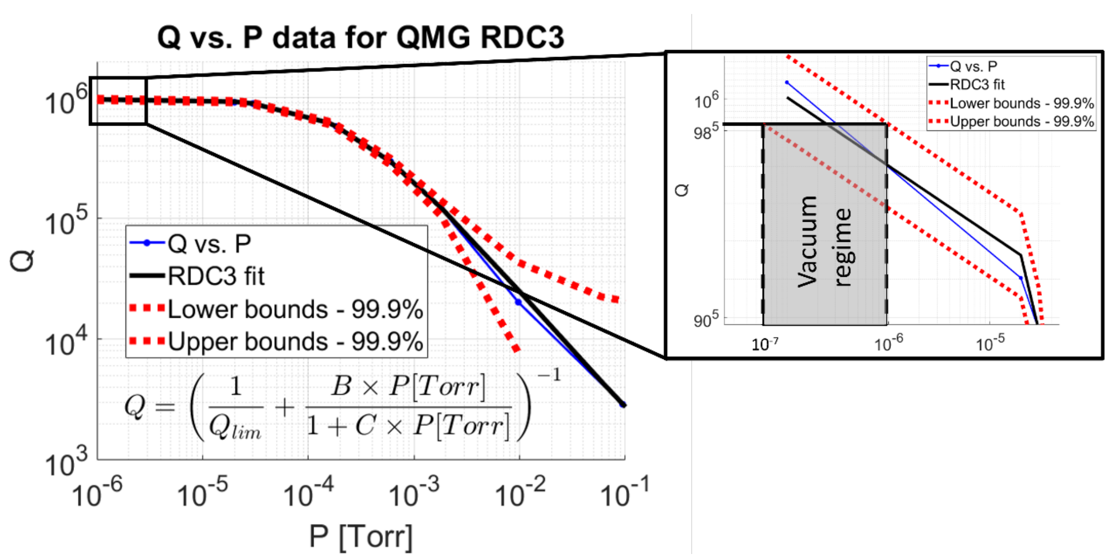

Figure 3.2-9. Quality factor versus vacuum chamber pressure. A QMG sealed with getter and place in a vacuum chamber reported a Q of 984k. Using the special fixture shown in Figure 3.2-8 the QMG seal was broken exposing the sensor to a vacuum chamber base pressure of 30 micro-torr. Q was reduced to 906k indicating that the vacuum sealed packaging pressure is below 1 micro-torr.

3.2.7 Leak rate and vacuum stability

The final discussion focuses on the stability of packaging pressures over time. For this purpose, two NEG and one getter-less package were set aside to periodically measure pressure sensor voltage. Minute drifts in vacuum packages due to low leak rates could indicate micro-voids in the AuSn preform seal, providing leak paths for low atomic number gas species. Therefore, it's prudent to test vacuum packaging pressure over long durations to determine its stability.

Figure 3.2-10 demonstrates that over 132 and 180 days, for NEG and getter-less packages respectively, the vacuum pressures continue to decrease over time. The initial vacuum voltage reading is offset to zero, and any positive increase in voltage change implies a decrease in packaging pressure. Packaging pressures seem to reduce and stabilize after approximately 80 days. However, the general takeaway from these results is that the sealing remains robust and does not exhibit any leaks over the depicted period. To determine the finite leak rate that may occur after package pressure stabilization (~80 days), resonate sensors like the QMG are required to monitor changes in Q over time. NEG vacuum packaging pressures have been shown to be < 1 micro-torr and the QMG has proven to be sensitive to Q changes when in >30 micro-torr vacuum chambers.

Figure 3.2-11 presents the calibrated data for the getter-less vacuum package, RP2 from Figure 3.2-10, after an additional 200 days. Calibration occurs when the vacuum package lid seal is comprised, exposing the Pirani sensor to atmosphere, and immediate measurement. A 25 milli-torr drop in package pressure is seen after 80 days, proving that the package seal remains robust and void free.

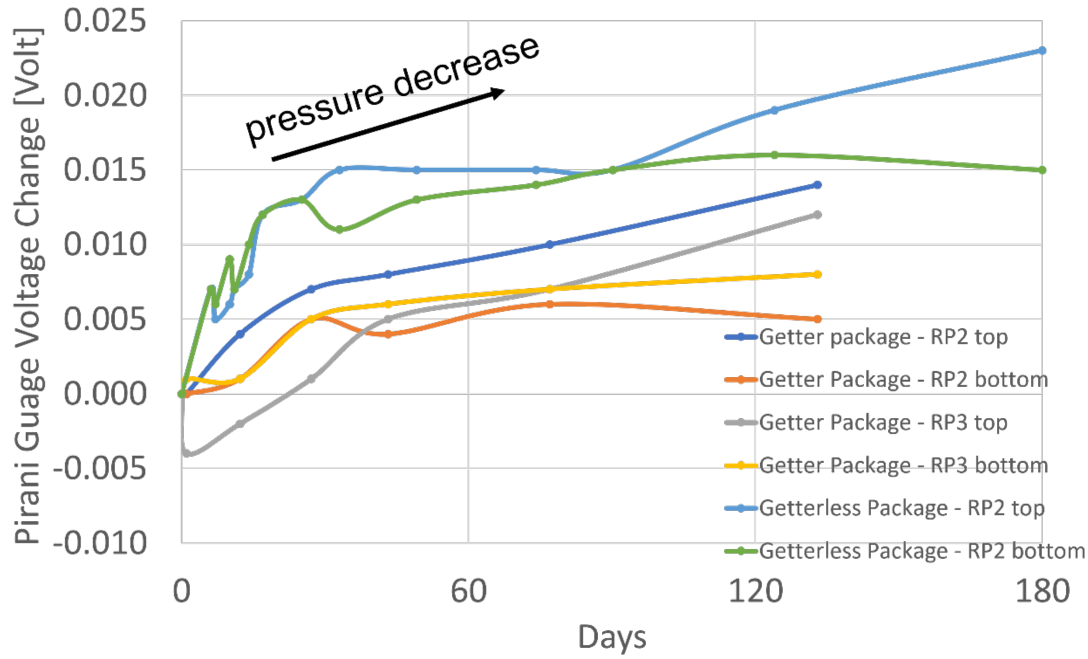

Figure 3.2-10. Normalized Pirani vacuum sensor reading over time for leadless ceramic package. Both getter-less and getter package pressure decreases overtime indicating that package pressure decrease is not solely a result of getter integration.

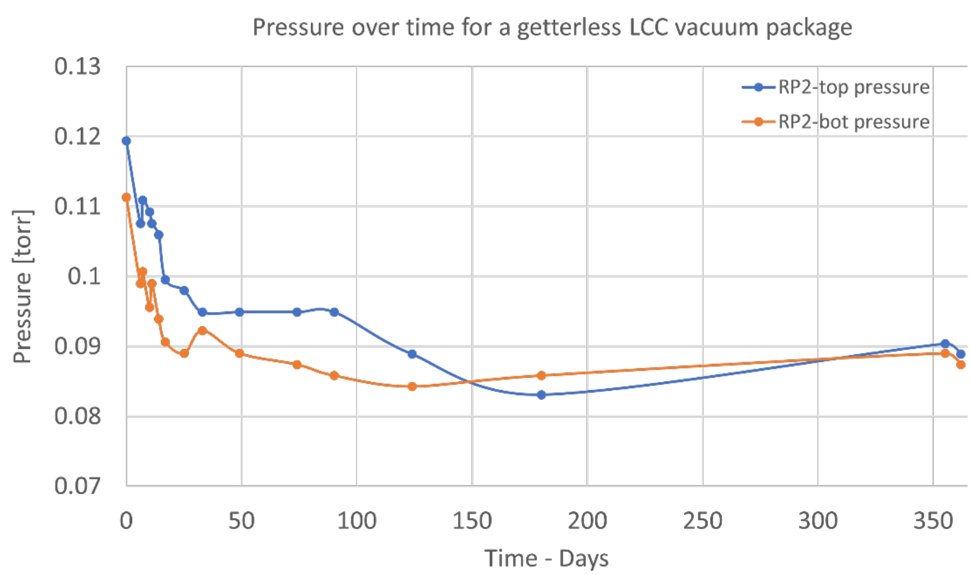

Figure 3.2-11. Calibrated Pirani pressure reading overtime for leadless ceramic package. RP2 Pirani sensor measurements were calibrated by opening RP2 vacuum package and calibrating sensor voltage in a pressure controlled vacuum chamber. Packaging pressure decreases roughly 20% over a year period.

3.3 Summary

The custom vacuum packaging furnace procured from Kurt J. Lesker, and now commercially available, enabled a new packaging approach, incorporating getter activation, and has facilitated the experimental verification of sub-micro-torr packaging pressure. This achievement is a first in the field, as reported in the literature, and remains state-of-the-art.

This work fielded a custom high-vacuum packaging tool having several operational advantages over previously reported vacuum packaging methods. The large process chamber equipped with a liquid cooled thermal shutter has enabled better thermal isolation than other commercially available tools, namely, SST3150. The process chamber also has a viewport, proving crucial when witnessing the vacuum sealing step. The approach employed here, as depicted in *Figure 3.1-2*(b), allows for higher, controllable temperatures on both the top and bottom movable platens. Given that the package, preform, and sensor are situated on the bottom base heater, the risk of losing sensor die and preform attachments due to gravity-induced detachment is effectively mitigated.

This work devised a vacuum sealing recipe aimed at minimizing the base pressure during the lid sealing step. However, this recipe only managed to decrease the final packaging pressure to 25 milli-torr for getter-less LCCs. A process optimized for time could potentially overlook the 4-day vacuum sealing process and proceed with sealing the package immediately following the initial bakeout recipe resulting in packaging pressures of ~1 torr. If one uses Kapton tape for sensor die attachment, an extensive bakeout of the attached sensor is crucial for achieving minimal vacuum, or else the packaging pressure will be two orders of magnitude higher due to the tape outgassing.

For a packaged sensor with silicon-gold interfaces, eutectic temperature and metallic diffusion will limit the maximum bakeout temperature. This work outlines a 24-hour bakeout procedure right below 370°C to yield satisfactory getter-less packaging pressure results of 60 milli-torr, without reaching the silicon-gold eutectic point and minimizing intermetallic diffusion.

This work also reveals that exposing a getter vacuum-packaged sensor to the atmosphere introduces loss mechanisms from oxide growth, surface ethanol, and hydrocarbon absorption Figure 3.2-3 - Figure 3.2-4 [43]. To replicate vacuum packaged Q factor measurements, the resonator either needs to experience the same bakeout processes (during vacuum packaging) in the vacuum measurement chamber or be opened in vacuum.

Lastly, we recorded the packaging pressure stability over 132, 180, and 350-day periods, determining that the package seal is robust and exhibits no leaks over the test duration.

Chapter 4: Quadruple Mass Gyroscope Angle Random Walk Reduction through Linearized Transduction

In Chapter 1.5 angle random walk and the mechanical thermal rate noise contribution to angle random walk (ARW) was discussed. Parameters like Q, drive frequency ω_x, drive amplitude A, and Coriolis mass m, if increased will decrease rate noise and effectively reduce ARW.

The vacuum packaging procedure and results were discussed in Chapter 3 with results indicating that the energy loss due to viscous damping forces, Q_{air}, were successfully mitigated with sub micro-torr vacuum packaging pressure. Measured Q will be shown to be limited by thermal elastic dissipation (TED) creating a Q ceiling for the novel QMG design presented.

The deep reactive ion etching (DRIE) procedure and results discussed in Chapter 2.4 revealed that large drive motion is feasible given the challenges that multi-aspect ratio etch features presents for DRIE. Smooth and vertical etch sidewalls are shown and notching at the buried oxide was significantly reduced.

The following sections in Chapter 4 discuss how to improve angular rate noise and reduce ARW through large amplitude linearized transduction. Linearized transduction encompasses and reduces nonlinearities associated for both mechanical and electrical effects. Mechanically, spring rates become nonlinear when MEMS folded flexures deflection begins to reveal axial force behavior in their reaction forces. Additionally, folded flexure deformation behaves nonlinearly when the small angle assumption for $\sin\theta$ no longer holds [64]. Nonlinearities due to electrical transduction are also analyzed, discussed, and mitigated.

By addressing nonlinear transduction mechanisms and implementing design improvements allowing for large displacement drive, this work has demonstrated the potential for significant noise reduction, resulting in best in class and state-of-the-art silicon MEMS CVG ARW performance.

4.1 MEMS CVG introduction and background

Consumer-grade microelectromechanical system (MEMS) Coriolis vibratory gyroscopes (CVGs) have steadily improved to meet demands of the smartphone market. With the emergence of virtual reality and autonomous vehicles, the need for high-performance low-cost, size, weight, and power (C-SWaP) inertial MEMS has been a driving force for sensor improvement. Similarly, applications in environments where GPS is unavailable (e.g., underwater, subterrains, buildings) have financially motivated governments to heavily invest in programs related to navigation-grade inertial MEMS.

In the literature over the past five years, both mode-split and mode-matched Coriolis vibratory MEMS gyroscopes have demonstrated laboratory measurements near or at navigation-grade angle random walk (ARW) and in-run bias instability (BI) [52]-[61]. ARW is governed by short term angular rate noise, while BI represents the ultimate angular rate sensitivity limited by flicker noise and long-term drift. CVGs operate by sensing energy moving from one mode to an orthogonal mode through the Coriolis effect. CVGs can be designed to operate in mode-matched or mode-split configurations. In mode-matched gyroscopes, the drive and sense mode are set to the same frequency, which enables gain in drive amplitude and sensitivity from resonance operation. In mode-split the drive and sense frequency are offset, simplifying design by eliminating the need for frequency matching but losing the resonance amplification on the sense axis. The mode-split configuration offers lower power, better scale factor stability, and less complexity than its mode-matched counterpart, however, rate noise performance, i.e., ARW, is limited by sense motion. Mode-matched gyroscopes utilize degenerate drive and sense modes to increase sensitivity, however, with the tradeoff of more complex, higher power electronics, and worse scale factor stability. Because of this, mode-matched gyroscopes theoretically should be able to achieve much lower ARW than the mode-split configuration with the mentioned tradeoffs. For this reason, the highest performance macro-scale CVGs operate in mode-matched configuration [52].

Some of the earliest published work in near-navigation grade silicon MEMS was out of Boeing [53],with their work in mode-matched disc resonator gyroscopes (DRG) demonstrating BI of 0.01 deg/hr and ARW of 0.0033 deg/√hr. Recently, Xu et al. have reported on a honeycomb-like DRG with record DRG-type quality factor of 650k while maintaining similar performance [54]. For mode-split gyros, Endean et al. from Honeywell [55]-[57], have recently demonstrated in-run and over temperature bias stabilities of 0.01 deg/hr and ARW of 0.002 deg/√hr. Honeywell plans to commercialize their gyroscope as a subcomponent of their HG7930 IMU in a future release [58]. Similarly, in [59] Gadola et al. from Politecnico di Milano with fabrication at CEA-Leti have demonstrated, through a mode-split CVG, the smallest high-performance MEMS CVG with BI sub-0.04 deg/hr and mean ARW of 0.004 deg/√hr. These recent improvements in ARW and BI in mode-split MEMS CVGs have outpaced mode-matched MEMS CVGs over the past few years.

Increasing MEMS gyroscope performance by reducing ARW and bias instability can be accomplished by increasing frequency and material Q. High frequency bulk acoustic wave gyroscopes attempt to accomplish this through increased operational frequency but are limited by drive amplitude and phonon-phonon loss (only relevant at high frequencies) in silicon. At high frequencies silicon carbide (SiC) is less limited by phonon-phonon losses and does offer large improvements in Q relative to silicon [61]. SiC is more inert and currently more difficult to fabricate at high aspect ratios which is inconsistent with the precision manufacturing that is required for navigation-grade inertial sensors [61],[62].

Glass blowing and torching methods developed by Cho and Wang [60], [63] have created a new class of 3D micro-gyroscopes and are promising technologies to miniaturize hemispherical resonator gyroscope (HRG) topologies. These approaches, however, combine disparate fabrication approaches and transducers are typically not defined in-situ with the resonator but rather by pick-and-place. Cho [60] has shown similar ARW and bias instability results as the mini HRG, however, this type of gyroscope does not follow the traditional economies of scale as traditional silicon MEMS.

Reducing electronic and quantization noise on both drive and sense also improves ARW when CVGs are not limited by thermomechanical noise. Therefore, careful consideration must be taken when designing the interfacing integrated circuits. Sense voltage white noise, drive white noise, and quantization noise are all factors that can add to ARW.

A recent example of CVG ARW improvement was shown in [59]. They were able to reduce CVG volume while maintaining low ARW by increasing drive amplitude to ~9 μm at a 25 kHz operating frequency and use high signal-to-noise ratio nano-resistive sensing. The nano-resistive gauges were carefully designed to cope with the 1%-nonlinearity and fracture limits. However, given the mode-split operation, sense quality factor provides little gain, and ARW cannot be reduced to a level below the navigation-grade of 0.003 deg/√hr.

Eq. (4.1) describes the thermomechanical noise contribution to CVG ARW for closed loop force-to-rebalance operation where k_B is the Boltzmann constant, A is the drive amplitude, Q_y is the sense quality factor, ω is the x drive or y sense frequency, T is temperature, and M is the Coriolis mass [68].

$$\mathrm{ARW_{MTN,CL}} \approx \sqrt{\frac{k_B T \omega_y}{A^2 M \omega_x^2 Q_y}\left[1+\left(\frac{Q_y(\omega_y^2-\omega_x^2)}{\omega_y}\right)^2\right]}\frac{rad}{\sqrt{sec}} \tag{4.1}$$

From Eq. (4.1), the most intuitive ways to decrease ARW_{MTN} are to maximize A, M, ω_x, and Q_y. Tradeoffs exists for each one of these parameters: i) increasing Coriolis mass could lower frequency, increase die size, or impact fabrication precision for thicker device layers, ii) increasing drive frequency could lower Coriolis mass, increase flexure stiffness and nonlinearity, decrease drive amplitude, and lower Q_y if operating in isothermal thermoelastic damping regime, and iii) increasing Q_y if thermoelastic limited requires flexure redesign. If Coriolis mass is increased, then to keep all other parameters the same, stiffer flexures will be needed to compensate for the increase in modal mass, stiffer flexures could impact the onset of nonlinearity, and Q_y could be lower if the operating in the isothermal regime.

When driving CVGs at large amplitudes (relative to MEMS characteristic spring length) special consideration must be taken to ensure linear operation [64]-[67]. Nonlinear frequency effects like Duffing, due to the axial beam stiffness and electrostatic spring softening, can lead to a diminishing effect on scale factor [66] creating more ARW and bias instability noise at the onset of nonlinearity. Furthermore, nonlinear resonance behavior creates instabilities on the rate signal [66]. Driving at signals beyond the onset of Duffing will increase ARW and bias instability due to noise and instability in the gyroscope output at both short and intermediate integration times [65], [66].

Maximizing drive amplitude is also not intuitive. As a general design rule, parallel plate transducers need to move at motions below ⅓ the parallel plate transducer gap, which constrains the drive amplitude and etch gaps to have a 3:1 relationship, placing a constraint on drive and sense transduction gap. In the QMG configuration reported in this work, comparable parallel plate capacitors operating at amplitudes less than 50% of the gap will maintain linearity to less than 0.1%. Mechanical flexures also need to be designed to handle larger drive amplitudes while minimizing axial flexure forces due to increased amplitudes. Although increasing drive amplitude A in Eq. (4.1) is not straightforward, if careful considerations are taken for linear design, ARW_{MTN} will have the largest reduction compared to any other parameter.

This works reports state-of-the-art MEMS CVG ARW performance 10× lower than prior published QMG work [70]-[73] Through extensive design and finite element analysis (FEA) simulation, previously reported in [69] and expanded on here, the work presented has minimized positive and negative Duffing term sources, and this research has demonstrated 0.0005 deg/√hr ARW, an uncompensated bias instability of 0.08 deg/hr, at a 6-Hz system bandwidth. This value was achieved by local moment balancing of symmetric folded flexures, linearizing the antiphase coupler beams, and the consideration, selection, and modification of electrostatic transducers that often lead to relatively large softening nonlinearities and instabilities. Furthermore, cross-axis stiffness (defined in Eqs. 4.8-(4.9)) has been reduced by 16× relative to some of the original quadruple mass gyroscope (QMG) groundwork [70]-[73]. Although cross-axis stiffness is not explicitly stated in Eq. (4.1), it creates a difference between ω_y and ω_x and is important for realizing improvements in ARW and BI. From Eq. (4.1) dependence of drive and sense frequencies, ω_x and ω_y, mode-match CVG operation can be orders of magnitude below mode-split operation, and the results reported here finally highlight this for silicon MEMS CVGs.

Following this introduction, Section 4.2.1 describes the design and fabrication of the improved linearity components. Section 4.3 presents the results and discussion. Section 4.4 contains concluding remarks and implications.

4.2 Design and Fabrication

4.2.1 Design

To ensure minimal mechanical design nonlinearity, the system mechanics must behave well below silicon's tensile strength in the linear elastic regime, and beam flexure design must minimize any axial component of stress. Three different folded flexure designs, shown in *Figure 4.2-1*, have been modeled and simulated for linearity and cross-axis stiffness. Design A contains a single folded flexure, Design B has two symmetric folded flexures, and Design C has two symmetric folded flexures with a truss connection. Among these three designs, design *B* was down selected and fabricated. Additionally, the antiphase coupler is compared to a fixed-fixed beam attachment type, similar to [72], for both linearity and mode separation.

The other common source of nonlinear frequency Duffing behavior is negative electrostatic force or spring softening. Mode-matched frequency tuners and parallel plate pickoffs and drives are major contributors to negative frequency Duffing [67].

Comb drive and sense pickoffs are used to minimize this behavior. Lastly, symmetric parallel plate frequency tuners are used to minimize further negative Duffing when the QMG as-fabricated Δf is tuned to meet the mode-matched condition.

The work presented here carefully reduces both these positive mechanical and negative electrostatic nonlinear frequency Duffing effects through moment-balanced folded flexures, linearized antiphase couplers, comb drive and sense pickoffs, and symmetric force-balanced parallel plate tuners, all described in the next sections.

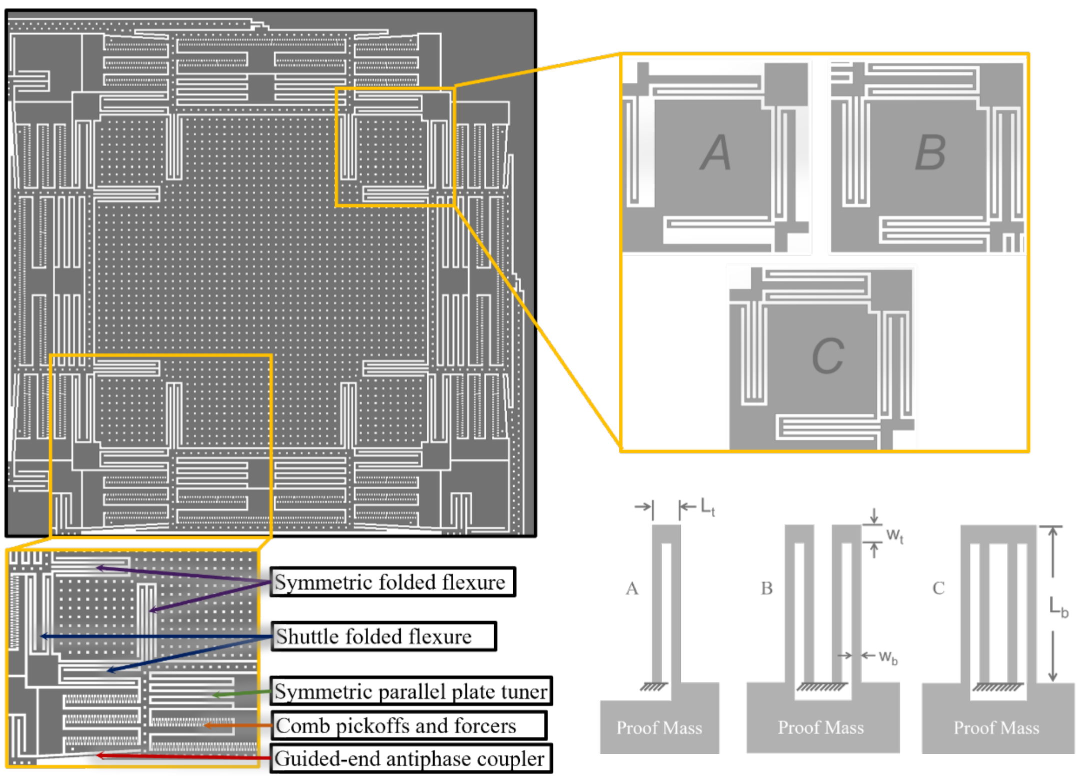

Figure 4.2-1 CAD model of one quadrant of the QMG with inset design A, B, and C. The dimensions shown for the folded flexure schematics relate to Eqs. (4.3)-(4.7). The bottom inset describes the quarter quadrant locations of folded flexures, antiphase coupler, capacitive forcers and pickoffs, and the frequency tuners.

4.2.2 Folded flexures

The three folded flexure designs have been modeled to understand acceptable nonlinearity over the maximum drive amplitude, determined by 20 μm transduction gaps, and balanced relative to softening nonlinearities described in sections 4.2.4 and 4.2.5. Inset images of three different flexure designs *A*, *B*, and *C* have been modeled. Design *A* is similar to prior QMG art [70]-[73], design *B* uses mirrored flexures balancing any local moments produced [74] at the individual folded flexure location, and design *C* uses trussed folded flexures [74]-[78]. Eq. (4.3)-(4.7) represent the *x* and *y* spring constant for each design [75].

Design A - folded flexure

$$k_{x,f} = \frac{Etw_b{}^3}{8L_b^3}\frac{\left(4L_b+\alpha\frac{L_t}{2}\right)}{\left(L_b+\alpha\frac{L_t}{2}\right)} \tag{4.2}$$

$$k_{y,f} = \frac{32Etw_b{}^3}{L_t^3}\frac{(L_b+2\alpha L_t)}{\left(L_b+\alpha\frac{L_t}{2}\right)} \tag{4.3}$$

Design B - symmetric folded flexure

$$k_{x,sf} = \frac{Etw_b{}^3}{4L_b^3}\frac{\left(4L_b+\alpha\frac{L_t}{2}\right)}{\left(L_b+\alpha\frac{L_t}{2}\right)} \tag{4.4}$$

$$k_{y,sf} = \frac{16Etw_b{}^3}{L_t^3}\frac{(L_b+2\alpha L_t)}{\left(L_b+\alpha\frac{L_t}{2}\right)} \tag{4.5}$$

Design C - symmetric folded flexure with truss

$$k_{x,t} = \frac{6EtI_{z,b}}{L_b^3}\frac{L_t^2+14L_t\alpha+36\alpha^2}{4L_t^2+41L_t\alpha+36\alpha^2} \tag{4.6}$$

$$k_{y,t} = \frac{6EtI_{z,t}}{L_t^3}\frac{8L_t^2+8L_t\alpha+\alpha^2}{4L_t^2+10L_t\alpha+5\alpha^2} \tag{4.7}$$

Here, $L_b$and w_b are beam length and width, L_t and w_b are truss length and width, as labeled in *Figure 4.2-1*, $I_{z,b}$ and $I_{z,t}$ are the second moment of inertia for the beam and truss, t is thickness, E is Young's modulus and $\alpha = \frac{I_{z,b}}{I_{z,t}}$.

From Eq. (4.3)-(4.7) the relationship between k_x and k_y, design *C* has the most axial stiffness compared to the other flexure design [74]-[75]. This is because when design *C* in its undeformed state, it can be reduced to four parallel beams in compression when the truss length L_t is small relative to the beam length L_b, and the truss width is greater than the beam width $\alpha < 1$. For the deformed shape, relevant due to the large deflection targeted in this work, this simplification is no longer valid, and FEA must be used to analyze stiffness. Figure 4.2-2 Fig. 2 plots an FEA comparison of Designs A-C, using sinusoidal x-motion and averaging the displacement dependent spring rates over half a period, plotting the relative frequency shift over 16 µm of drive amplitude. A quarter modal mass of ~1.9 mg was derived from FEA. Summing all the moving masses and weighting moving springs by 0.2235 (a commonly used value for a cantilever's effective mass) [76] validates this approach with a calculated modal mass of 2.05 mg. Design *C* behaves the most linear shifting frequency by only 307 ppm at 16 µm where Design *B* shifts frequency by 480 ppm. Design *A* which was included to resemble prior QMG art [70]-[73] behaves the most nonlinear, shifting frequency by 992 ppm.

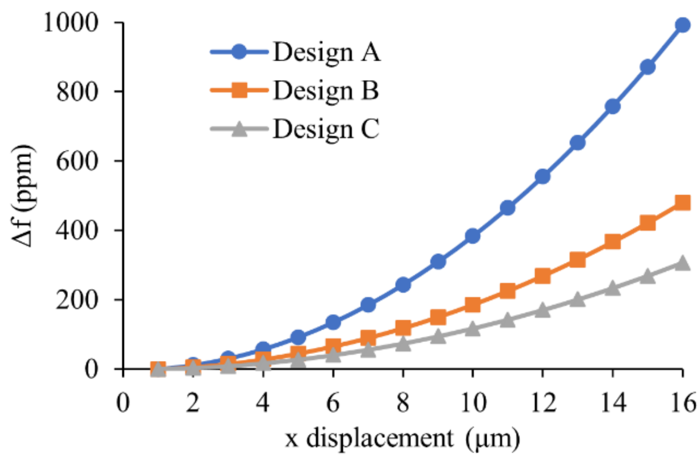

Figure 4.2-2 FEA frequency nonlinearity results of QMG with designs *A*-*C*.

When designing flexures for MEMS gyroscopes, cross-axis stiffness is another important factor that needs to be minimal [64], [75]. Cross-axis stiffness when simplified and reduced to only x and y degrees of freedom (neglecting z and respective θ rotations) is represented by the following 2 × 2 matrix.

$$\begin{bmatrix} k_{xx} & k_{xy} \\ k_{yx} & k_{yy} \end{bmatrix} \begin{bmatrix} x \\ y \end{bmatrix} = \begin{bmatrix} F_x \\ F_y \end{bmatrix} \tag{4.8}$$

where, $k_{xx} = k_{yy},\ k_{xy} = k_{yx}, F_y = 0$

$$k_{xy} = -\frac{k_{xx}y}{x}, k_{xx} = \frac{F_x x}{x^2 - y^2} \quad (4.9)$$

Due to the two-fold symmetry [77], the QMG has equal k_{xx} and k_{yy} as well as k_{xy} and k_{yx}. The pivoting exterior levers, however, do introduce minute imbalances that can be amplified by fabrication asymmetries and cross axis compressive forces that result in cross-axis motion. From Eq. (4.8) a relationship is derived to determine cross-axis stiffness k_{xy}. In FEA the modal mass (on the left in *Figure 4.2-1*) is displaced in the x direction and the output solution of F_x and y are captured to determine k_{xx} and k_{xy}. Since the modal mass is not displaced in the y-direction, the reaction force F_y is zero.

Figure 4.2-3 plots the static y displacement of the QMG modal mass, analogous to quadrature motion, during 16 μm of static drive motion. Design *A* has over 25 nm more y-motion whereas designs *B* and *C* have <5 nm y-motion. Although the symmetric trussed folded-flexure (design *C)* has lower y motion at small static drive displacements, at x drive displacements >7 μm the trussed symmetric folded-flexure (design *C*) begins relieving net axial compression forces by displacing the shuttles resulting in larger y motion after higher deflections. Design *B* folded flexures accommodate larger axial forces making the folded flexure inherently more nonlinear in k_{xx} but less prone to y quadrature motion. Given the overall lower amount of y motion, it is believe that design *B* is more promising due to an effective quadrature reduction rather than reducing its frequency nonlinearity by 173 ppm.

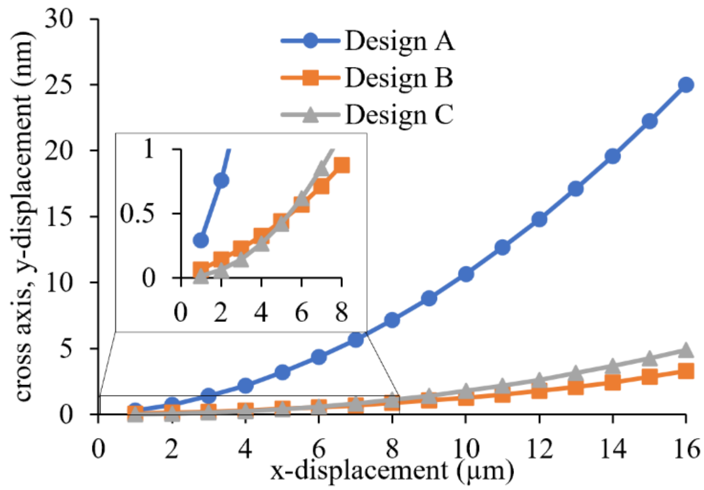

Figure 4.2-3 EA results of static quadrature *y* motion over 16 µm of drive displacment. Prior QMG art has over 5× more static quadrature motion than both designs *B* and *C.* Inset is a zoomed-in region showing the overlapping cross-axis y-displacement between *B* and *C.*

Taking a deeper look at flexure designs *A*-*C*, as the flexures deform in the *x* direction the *y* component of stiffness changes due to the spring deformation. Figure 4.2-4a illustrates exaggerated *y* motion when the flexure is under downward compressive loading and zero *x* motion. Figure 4.2-4b illustrates 16 µm of *x* motion with zero *y* motion. Figure 4.2-4a-b are useful to help visualize axial stiffnes as the Coriolis mass travels in the *x* direction.

The folded flexure and the trussed folded flexure, designs *A* and *C*, have decreasing k_y with increasing δ_x , while design *B,* k_y increases with δ_x due to moment balancing of the mirrored folded flexures. Therefore, for designs *A* and *C*, the nonlinear δ_x component of k_y can be thought as a virtual flexure in series. Since design *B* has an increasing k_y with δ_x, the nonlinear k_y component can be thought as adding a virtual spring in parallel. Eqs. (4.10)-(4.12) represent these nonlinear flexures where $\widetilde{C_f}$=1.19, $\widetilde{C_{sf}} = 1.0$, and $\widetilde{C_t} = 2.02$ are empirical correction factors with results derived from FEA using deformed meshes with δ_x steps of 1 µm.

$$k_{y,f}(\delta_x) \approx \frac{1}{\frac{1}{k_{y,f}}+\frac{1}{\frac{1}{\widetilde{C_f}}\left(\frac{EI_b}{L_b w_b}\right)\frac{1}{\delta_x}}} \quad (4.10)$$

$$k_{y,sf}(\delta_x) \approx k_{y,sf} + \frac{1}{\widetilde{C_{sf}}}\left(\frac{200EI_b}{3L_b^3 w_b^2}\right){\delta_x}^2 \quad (4.11)$$

$$k_{y,t}(\delta_x) \approx \frac{1}{\frac{1}{k_{y,t}}+\frac{1}{\frac{1}{\widetilde{C_t}}\left(\frac{200EI_b}{3L_b}\right)\frac{1}{{\delta_x}^2}}} \quad (4.12)$$

The empirical Eqs. (4.10)-(4.12) are plotted in Fig. 5. The trussed folded flexure's virutal spring constant of Eq. (4.12) is the equation that was analytically derived in [12] with the added FEA correction factor.

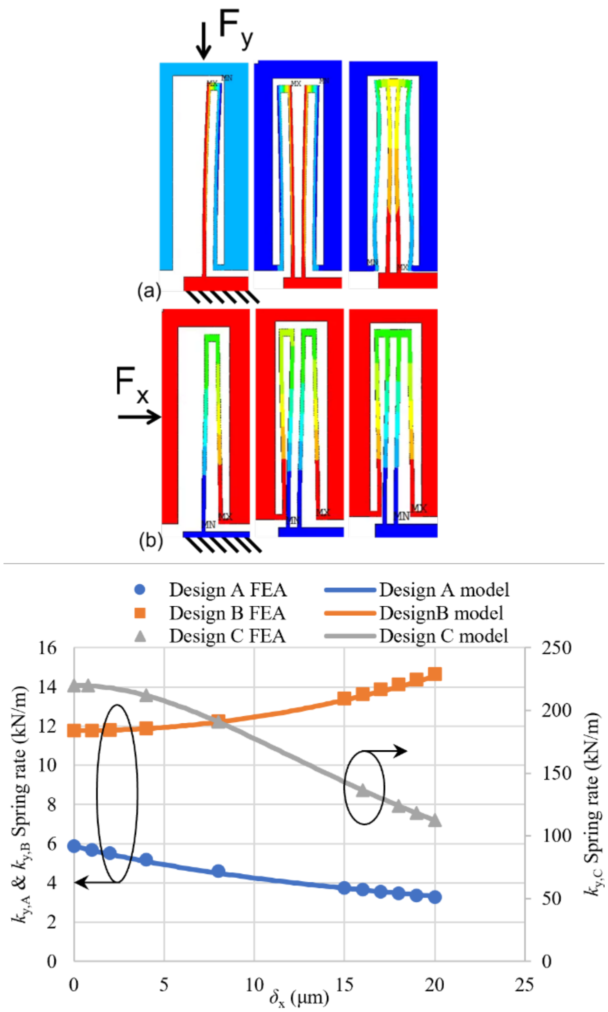

Figure 4.2-4 Top: (a) Flexure designs *A*-*C* with a compressive *y* load with zero x motion and magnified y motion. (b) Flexure designs *A*-*C* with zero *y* motion and 16 μm of *x* motion.Bottom: FEA results and the respective fit equations for $k_{y,f}(\delta_x)$, $k_{y,sf}(\delta_x)$, and$k_{y,t}(\delta_x)$.

From the Figure 4.2-4 plot, design *A* is the most compliant whereas *B* and *C* are, respectively, 2× and 33× stiffer than *A*. As design *C* travels in the CVG drive direction, axial forces generated also become 33× larger. If a small k_y difference is introduced, the net force will be balanced by quadrature *y* motion – this motion is also shown in Figure 4.2-3. Design *B*'s overall superior performance relative to *A* and *C*, with 480 ppm frequency nonlinearity and ~3 nm of static quadrature motion, makes it the best design to minimize ARW by increasing drive amplitude and reducing quadrature - i.e., the difference between ω_y and ω_x.

4.2.3 Antiphase coupler

To reduce gyroscope vibration sensitivity, vibration modes where the QMG Coriolis masses move in-phase are undesirable and are sensitive to environmental accelerations. Given the fundamental operation of tuning fork gyroscopes (TFGs) like the QMG, these modes cannot be eliminated but rather shifted away from the fundamental operational mode by means of an antiphase coupler. In the intended operational mode, neighboring quadrants of the QMG will move in opposite direction (antiphase) to balance momentum and minimize anchor loss. At the bottom of Table 4-1 illustrates the intended antiphase mode and the other parasitic modes that can arise during operation. The design by Simon et al. in [72] and others [70], [73] shift these parasitic modes well above the antiphase frequency by suppressing the Coriolis mass coupling spring in-phase motion but introduce a large positive frequency Duffing term due to the antiphase clamped-clamped beam mechanism [72]. This clamped-clamped beam design limits the linearity of drive amplitude and, ultimately, the maximum drive displacement is typically < 2 μm. On the left of Figure 4.2-5a is the clamped-clamped antiphase coupler similar to what is used in prior QMG art [70], [72]-[73] and on the top right is a linearized guided folded flexure antiphase coupler. The guided folded flexure antiphase coupling spring suppresses in-phase motion by introducing beams with a slight angle off from the grid-like x-y planar layout (i.e., lines are orthogonal). Additionally, the angled beams have an end folded flexure that increases y direction compliance, thus, reducing axial beam forces that create nonlinear spring rates.

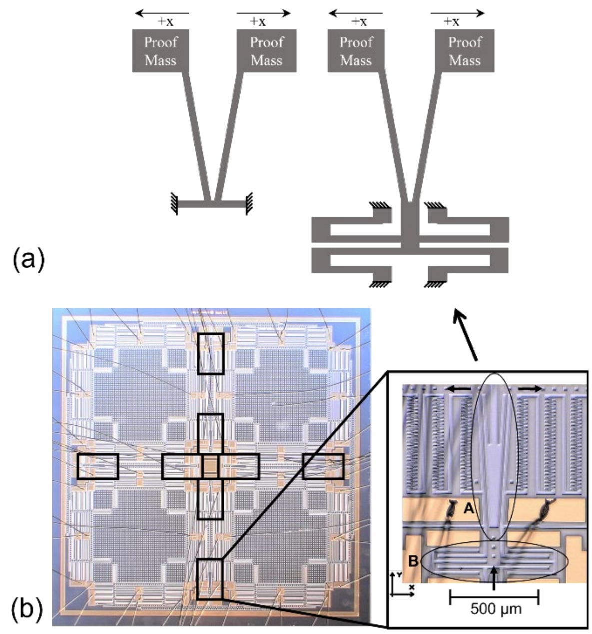

Figure 4.2-5 Top: schematic of a clamped-clamped beam antiphase coupler (left) and the linearized guided folded flexure antiphase coupler (right). Bottom: fabricated and wirebonded QMG with zoomed in portion illustrating the antiphase coupling mechanism's components A' and B' where A' is the angled flexures and B' is the guided folded flexure.

The reported guided folded flexure mechanism shown on the right in Figure 4.2-5a has been designed and simulated in Ansys® FEA to minimize stress and cubic stiffening that occurs during large displacements. For comparison, the clamped-clamped type was also simulated (Figure 4.2-5a). The angled beams in Figure 4.2-5b, (circle *A'*), separate the antiphase and in-phase modes while the guided folded flexure antiphase coupler (Figure 4.2-5a right, circle *B'* Figure 4.2-5b left), accommodate linear *y* displacement and moment balance at the angled-beam connection.

Due to symmetry of the antiphase degenerate modes, positive displacement, $+k_x$, is defined by the arrow directions in Figure 4.2-5a. The folded flexure on the right in Figure 4.2-5a (also shown and labeled B' in Figure 4.2-5b right) also offers a unique integration point on the guided-end folded flexures where piezoelectric transduction and Quality factor tuning can be implemented [79]. Here, y-motion in the guided end from piezoelectric transduction would induce x-motion on the Coriolis masses. At the bottom of Table 4-1 labeled "1", plots the QMG drive mode shape, the first degenerate mode, and the sense mode can be visualized by simple rotating the page by 90 °. Table 4-1 lists the first four degenerate modal frequency values where modes 3-4 are the most sensitive to environmental accelerations due to the in-phase motion of the Coriolis mass. The respective mode shapes are shown below Table 4-1for visualization. The reported guided folded flexure mechanism separates the antiphase and in-phase modes by a factor of 1.26 which scales with fundamental antiphase frequency. Although the clamped-clamped beam further separates the antiphase mode from the in-phase modes by 1.4, the nonlinear implications make the design unsuited for large actuation.

TABLE 4-1 MODAL ANALSYS OF THE FIRST 4 DEGENERATE MODES

Mode #	*Degenerate mode description*	*Frequency (Hz)*		*Normalized wrt to fundamental mode*		
		Clamped - clamped	Guided folded flexure	Simon [21]	Clamped - clamped	This work
1	Anti-phase mode	3807	3860	1	1	1
2	Lever anti-phase mode	4468	4513	1.46	1.17	1.17
3	In-phase mode	5330	5180	1.69	1.40	1.34
4	Lever in-phase mode	5748	5691	1.99	1.51	1.47

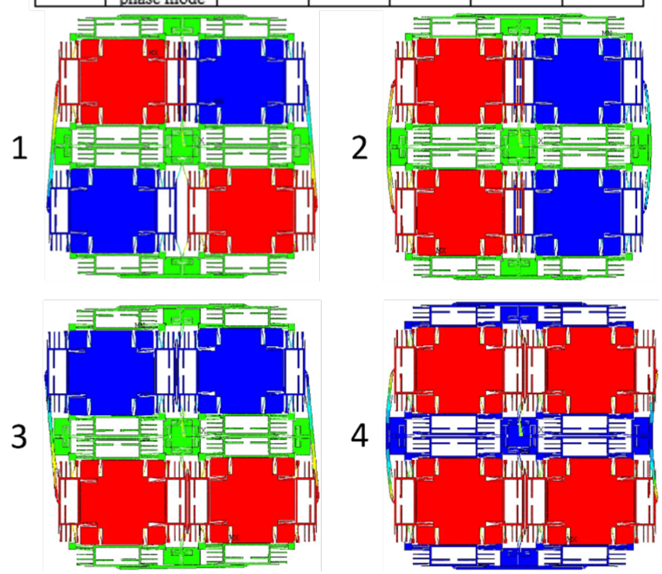

***FEA modal plot of the QMG first four degenerate modes. Blue contours represent negative motion, red contours represent positive motion, and green contours represent zero motion.**

Table 4-1 also includes a column with Simon's [21] clamped-clamped antiphase coupler design that was demonstrated to further separate all parasitic modes; however, still faces the challenge of nonlinearity at larger drive amplitudes.

Clamped-clamped beams are well known to behave nonlinearly [64], [74]-[76], [78]. This is due to the axial stiffness component when normal deflections become large relative to their characteristic length. *Figure 4.2-6* plots the percent change in tension and compression, $+k_x$ and $-k_x$, for values up to 16 µm of static drive displacement. For small displacements, $+k_x$ and $-k_x$ for clamped-clamped and the guided folded flexure antiphase coupler are nominally 120 and 97 N/m, respectively. The clamped-clamped coupler behaves 5× more nonlinearly than the guided folded-flexure coupler. For both cases, the antiphase coupler is the largest nonlinear Duffing source for the QMG accounting for 58% of the total positive Duffing frequency nonlinearity. The antiphase coupler only accounts for ~9% of the total QMG stiffness and contributes a total of ~280 ppm drive nonlinearity at 16 µm displacement whereas the symmetric flexures and shuttle springs account for the remaining 42% of the total positive Duffing nonlinearity. The antiphase coupler nonlinearity can also be seen in the total nonlinearity in Figure 4.2-2's comparison of flexures with a 280 ppm offset for all Designs *A*-*C*.

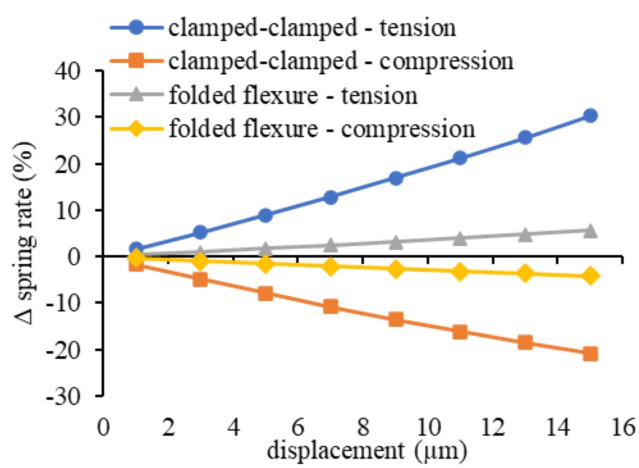

Figure 4.2-6 Percent change in the antiphase coupler spring rate as a function of drive displacement.

4.2.4 Electrostatic softening – comb drives and pickoffs

In this section and all subsequent sections, the QMG described has flexure Design *B* and the guided folded flexure shown on the right in Figure 4.2-5a. Electrostatic drive and pickoffs require DC bias voltage for transduction which also appears as negative frequency Duffing at large amplitude drive [67], [81]-[83]. While offering large capacitance gradients, parallel plate drive and pickoffs suffer from nonlinear spring softening due to the inverse gap relationship. To mitigate this effect, the reported QMG electrostatic comb transducers for both drive and sense to reduce electrostatic spring softening. Comb capacitors, however, cannot eliminate spring softening due to the comb tips acting like parallel plate capacitors as the designed etch gap is closed [83]. Comb capacitance is readily described by (4.13) where *N* is the number of overlapping comb fingers, *t* is the silicon thickness, L_0, is the static overlap length, *g* is the comb gap, and ε_0 is permittivity of free space.

$$C_c = \frac{2Nt\varepsilon_0(L_0+x)}{g} \tag{4.13}$$

When operating comb drives in push-pull the following expression (4.14) is obtained [79]:

$$F_c(t) = \frac{1}{2}\frac{\partial C}{\partial x}(V_2^2 - V_1^2) = 2\frac{\partial C}{\partial x}V_{dc}V_{ac}\sin(\omega_0 t) \tag{4.14}$$

V_1 and V_2 are drive signals at frequency ω0 that are 180° out of phase and when V_1 and V_2 have equal V_{dc} and V_{ac} terms, the resulting push-pull force is described by eq. (4.14). Although comb capacitor parallel plate tip capacitance is negligible at small displacements, as drive displacements increase so does electrostatic softening as described in (4.15)-(4.17):

$$C_{tip} = \frac{N\varepsilon_0(w_{tip}t)}{L_0 - x} \tag{4.15}$$

$$F_{c,tip} = \frac{1}{2}\frac{\partial C_{tip}}{\partial x}V^2 = \frac{1}{2}\frac{C_{tip}L_0}{(L_0 - x)^2}V^2 \tag{4.16}$$

$$k_{e,tip} = \frac{\partial F_{c,tip}}{\partial x} = \frac{C_{tip}L_0}{(L_0 - x)^3}V^2 \tag{4.17}$$

As drive displacement approaches half the gap or 10 µm, $k_{e,tip}$ becomes a non-negligible softening term. Figure 4.2-7 plots static +kx and -kx obtained from FEA as well as +kx and -kx when including comb tip softening mathematical model from eqs. (4.15)-(4.17). Table 4-2 highlights various parameters used for design, modeling, and FEA simulation. Although antiphase guided folded flexure introduces both positive and negative spring rates, the net effect is reduced since half the QMG is in compression while the other half is in tension. The maximum static nonlinear change of combined values $+k_x$ and $-k_x$, changes by 0.105% representing a +480-ppm change in frequency when neglecting comb tip softening. This value is similar to [59] but at nearly twice the static amplitude (0.1% at 9 µm [59]vs 0.039% at 9.5 µm here). Since the QMG will be driven well above 2/3rd the gap, the static pull-in voltage for comb tip capacitance effect was also calculated to be 248 V, well below the V_{DC} bias applied [76], [83].

Although capacitive comb transducers introduce electrostatic softening, their relative impact on the QMG drive operation is small. In comparison to parallel plate capacitors, comb transducers' softening, and nonlinear sense signal behavior are superior and have relatively low impact on net nonlinearity of the QMG that spring rates introduce. Prior DRGs and QMGs [52],[70]-[73] have been limited to 8× lower drive motion due to parallel plate softening and transduction nonlinearities, thus limiting ARW.

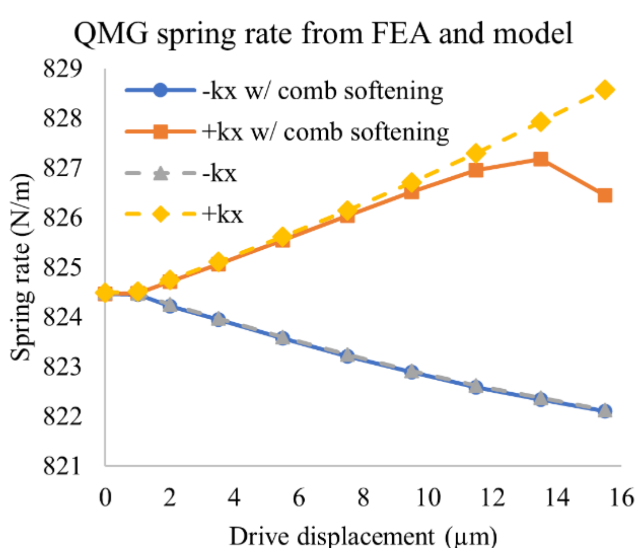

Figure 4.2-7 FEA static spring rates for positive (+k_x) and negative (-k_x) displacements and the combined static spring rates with comb drive tip electrostatic softening (+k_x w/ comb sofenting) (-k_x w/ comb softening). Note, "-k_x w/ comb softening" and "-k_x" only have a minute difference where the lines are overlapping.

TABLE 4-2 QMG DESIGN PARAMETERS AND MEASURED VALUES

Parameter	***Symbol***	***Value***
B' antiphase spring width	w_a	10 µm
A' angled antiphase beam width	w_θ	10 µm
Combined spring constant	k_x	824.5 N/m

Parameter	***Symbol***	***Value***
Modal mass	*m*	6.67 mg
Comb tip width	w_{tip}	5.1 µm
Comb drive capacitance per mass	C_c	1.8 pF
Comb drive gradient	dC_c/dx	0.0673 pF/µm
Comb tip capacitance per mass	C_{tip}	0.11 pF
Quality factor – drive	Q_x	705k [a]
Quality factor – sense	Q_y	704k [a]
Drive frequency	f_D	3,540 *Hz* [a]
As-fabricated mismatch	Δf	3.8 *Hz* [a]

a. Measured values

4.2.5 Electrostatic softening – parallel plate frequency tuners

Lastly, symmetric parallel plate frequency mismatch tuners were implemented to adjust as-fabricated Δf for mode-matched CVG operation while minimizing Duffing nonlinearity due to higher-order electrostatic force terms. These tuners are originally described in [81]. Eq. (4.18)-(4.23) compare typical parallel plate capacitors to a symmetric type.

$$C_{pp} = \frac{\epsilon_0 A}{(g-x)} \tag{4.18}$$

$$C_{pp,sym} = \frac{\epsilon_0 A}{(g-x)} + \frac{\epsilon_0 A}{(g+x)} \tag{4.19}$$

$$F_{pp} = \frac{1}{2}\frac{\partial C}{\partial x}V^2 = -\frac{1}{2}\frac{\epsilon_0 A}{(g+x)^2}V^2 \tag{4.20}$$

$$F_{pp,sym} = +\frac{\epsilon_0 A}{2}\left(\frac{1}{(g-x)^2} - \frac{1}{(g+x)^2}\right)V^2 \tag{4.21}$$

$$k_{pp} = \frac{\partial F_{pp}}{\partial x} = -\frac{1}{2}\frac{\epsilon_0 A}{(g-x)^3}V^2 \tag{4.22}$$

$$k_{pp,sym} = -\frac{\epsilon_0 A}{2}\left(\frac{1}{(g-x)^3} + \frac{1}{(g+x)^3}\right)V^2 \tag{4.23}$$

Symmetric parallel plate tuners have a rotor on both sides of the stator, balancing out net electrostatic forces under small displacements. Although symmetrical parallel plate tuners do not offer any dual use (sense transduction and tuning), they are relatively less nonlinear than a typical parallel plate layout. Figure 4.2-8 plots the symmetric parallel plate tuner force and spring softening normalized with respect to a parallel plate (ratio of Eqs. (4.21):(4.20) and Eqs. (4.23):(4.22)). The symmetric parallel plate tuner offers larger electrostatic spring softening during drive but exhibits lower net electrostatic force. Introducing small fabrication imperfections will result in only small deviations in Figure 4.2-8's net force ratio and electrostatic softening ratio.

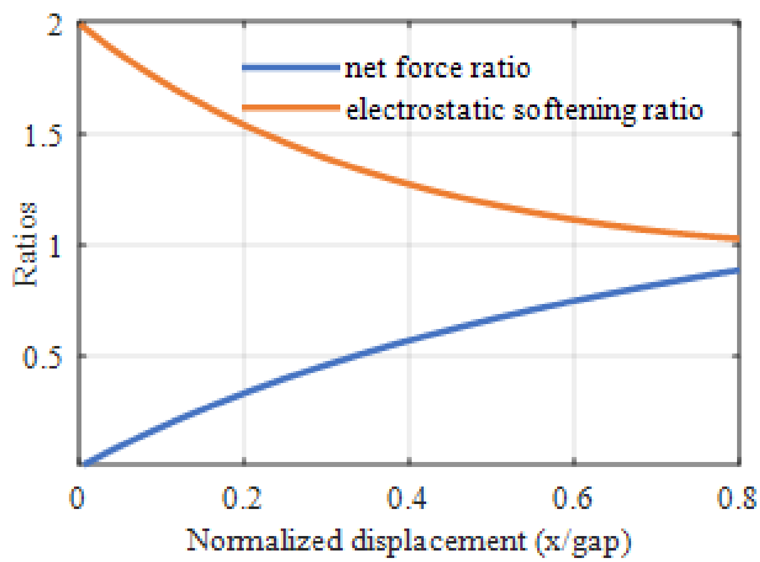

Figure 4.2-8 Plotted ratios of symmetric parallel plate to a parallel plate for force and electrostatic spring softening.

Given the relative benefits of the symmetric parallel tuner in comparison to a traditional parallel plate capacitor, the symmetric capacitor was selected due to its relatively larger electrostatic spring softening behavior, lowering bias V_{DC}, and lower net bias force which adds to negative Duffing frequency nonlinearity. Since tuning as-fabricated *Δf* is required for mode-match CVG operation, eliminating negative Duffing is impossible, however, prudent design selection of the symmetric parallel plate tuner will minimize its overall impact.

The static pull-in voltage for the symmetric tuners was calculated to be 56 V which accounts for symmetric nature of the parallel plates effectively increasing $V_{pull\text{-}in}$ by ~3 V. Given the relatively low static $V_{pull\text{-}in}$, it's worth highlighting that in this configuration 50 V_{DC} tuning will tune a maximum of 10 Hz as fabricated *Δf*. To maintain the desired and comparable linear behavior and frequency tuning resolution, as fabricated Δf should be below 4 Hz. Consequently, conservative estimates for dynamic pull-in voltage are 10% lower than that of the static value [83]. Therefore, careful consideration must be taken when tuning as-fabricated *Δf* and driving beyond 2/3rd the gap [76].

4.2.6 Fabrication and packaging

This work extends on the original work in [84]-[85] using similar manufacturing and packaging approaches. A three-mask process using <0.005 *Ω-cm* P-type doped 150 mm (100) oriented single crystal silicon on insulator wafers with device layer thickness of 100 µm are processed with backside die attach metal, top electrode metal, and deep reactive ion etching (DRIE) that defines the CVG. The DRIE mask layer has trench widths that are 5, 15, 20, and 40 µm wide. The 5 µm wide etch trenches define the comb capacitance and the 20 and 40 µm trench widths accommodate parallel plate tuners and the large displacement travel of the QMG Coriolis masses. DRIE is performed with a Plasma-Therm VERSALINE DSE tool with a recipe developed specifically for an aspect ratio independent etch with minimal notching and 90° sidewalls. The DRIE recipe includes a changing electrode bias and waveform that allows for charge relaxation at the buried oxide etch stop [86]. The DRIE recipe is broken down in two etch process: i) a bulk etch and ii) a finishing or landing etch. Since the etch aspect ratio varies by a factor of 8, C_4F_8 passivation polymer is nonlinearly morphed during the bulk etch to protect the low aspect ratio features as the etch lands on the buried oxide. The landing etch was developed to slowly etch the 5 µm critical dimension (CD) features while continuing to passivate and protect the larger etch areas. Additionally, the landing etch uses a nonlinear passivation morph to minimize silicon-oxide interface notching.

After DRIE, the wafers are singulated using DiscoTec America's Stealth Dicing™ laser dicing. Vapor hydrofluoric acid releases the device layer from the handle by etching the 5 µm of buried oxide. The dies are attached using either a AuSi or AuSn eutectic in a leadless ceramic chip carrier. Multiple sensor physics packages go through various bakes and vacuum sealed with getter at pressures below 1 µTorr. Die attach and the vacuum sealing process of the physics packaged is further described in [84]-[85].

4.3 Results and Discussion

4.3.1 Test setup

Vacuum packaged QMGs were tested on a rate table in an environmental chamber (Acutronic AC117) with electronics provided by Toyon Research Corp through a small business innovative research contract, electronic boards shown in *Figure 4.3-1* . The rate table sits on a 1500 lb granite table providing low frequency vibration isolation. The front-end Toyon electronics pickoff channels use a two-stage ultralow noise amplifier where the first amplifier is configured as a transimpedance amplifier and the second is unity gain producing 30 zF/√Hz capacitive noise and designed to operate with a nominal 1.6 pF input capacitance and 12 pF of stray capacitance. The push-pull [80] differential forcers channels have a maximum output of ± 10 V at 10 nV/√Hz noise. The power conditioning electronics bias voltages can tune up ~5 Hz frequency mismatch (symmetric parallel plates at ~38 V) with 38 μV precision reducing Δf to ~70 mHz. Further details about the CVG front-end conditioning electronics can be provided by Toyon Research Corp through individual inquiries. Toyon Research Corp has inertial sensing roots that go back to Delco Systems Operations with David D. Lynch [52]-[88] which has since then been acquired by Northrop Grumman.

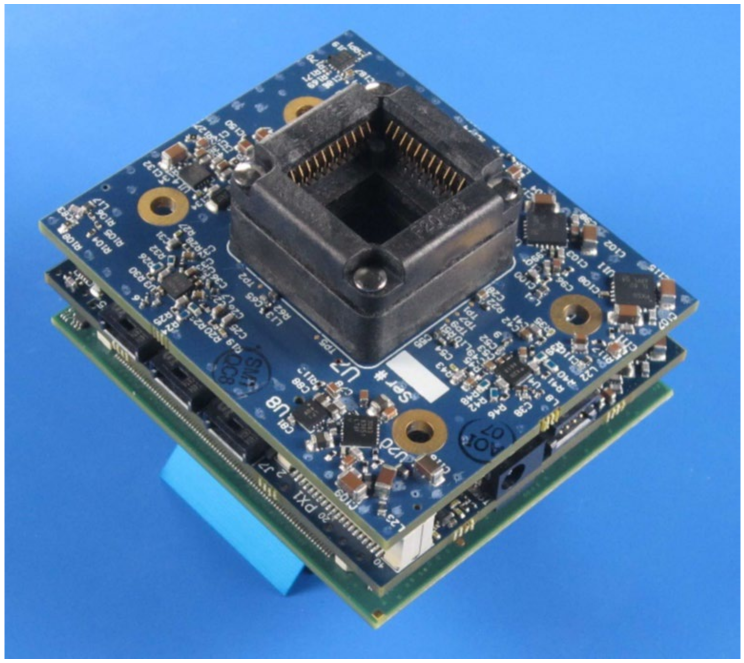

Figure 4.3-1. Toyon Research Corporation electronics procured by the Army Research Lab by a small business innovative research contract. Toyon Research has a history working with low noise Coriolios vibratory electronics and has demostrated navigation-grade noise performance with several gyroscope architectures.

The measurement setup experiences a maximum temperature fluctuation rate of 0.1 ℃ per hour and mean temperature coefficient of frequency for the QMGs is -17 ppm/°C. Quality factor was measured using a Zurich Instruments HF2LI lock-in amplifier by ringdown method using a phase-locked loop. The measured *Q* values are at room temperature and listed in Table 4-2. Figure 4.3-2 provides frequency and *Q* values for both drive and sense modes over a -35 ℃ to 75 ℃ range. Both drive and sense frequencies maintain a 3.8 Hz as-fabricated delta over the temperature range with temperature coefficient of frequency of ~ -17 ppm/°C.

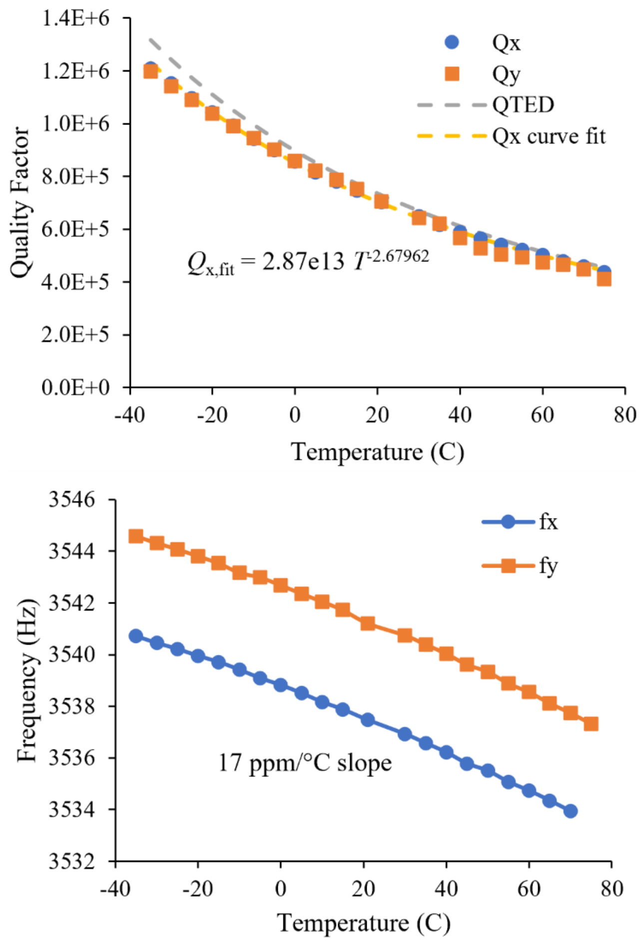

Figure 4.3-2 Quality factor and frequency plotted from -35 °C to 75 °C. Q difference between Q_x and Q_y maintain a <1% mismatch and temperature fluctuations are believed to introduce larger error at lower absolute Q values. As fabricated Δf maintains a 3.8 *Hz* mismatch over the defined temperature range. Q_{TED} is shown for comparison. QMG quality factor is mostly limited by Q_{TED}.

4.3.2 Thermoelastic dissipation limited quality factor

Extensive QMG thermoelastic dissipation (TED) modeling has been reported in [89]. [89] examines individual TED sources of loss for various flexure components of the QMG. Quality factor for TED can be represented by the following Eq. (4.24):

$$Q_{TED} = \left[\frac{\rho C_{Si}}{E\alpha^2 T_0}\right]\frac{1+(\omega\tau)^2}{\omega\tau}, \tau = \left[\frac{W}{\pi}\right]^2 \frac{\rho C_{Si}}{\kappa}, \omega = 2\pi f \qquad (4.24)$$

where ρ is material density, C_{Si} is specific heat capacity, E is Young's modulus, α is coefficient of thermal expansion, κ is thermal conductivity, W is beam width, and ω is angular frequency. τ represents the time constant of the thermal mode. Since the modulus and coefficient of thermal expansion change with temperature [90]-[93], Q_{TED} over temperature scales with $T^{-2.8}$ and the measured Q_x scales with $T^{-2.68}$. Figure 4.3-2 plots Q_{TED} as a function of temperature and is compared with the QMG Q_x and Q_y results. Since the designs in this work operate well within the isothermal regime, fQ of 2.58e9 obtained from COMSOL FEA in [89] is used to scale the Q_{TED} for the actual operational frequency. Since $Q_{measured}$ is the inverse sum of all Q mechanisms, the difference in $Q_{measured}$ and Q_{TED} can determine the contribution of Q_{other}. Q_{other} is defined by the following Eq. (4.25).

$$\frac{1}{Q_{other}} = \frac{1}{Q_x} - \frac{1}{Q_{TED}} \tag{4.25}$$

The mean value over temperature of Q_{other}, which includes viscous losses, anchors losses, and surface losses among other loss mechanisms, is ~17M indicating the QMG reported here is mostly limited by Q_{TED}. Q_{TED} can further be improved if (111) silicon is used [89], [93], however, given this Q ceiling, noise improvements for this work can only be improved by increasing drive amplitude.

4.3.3 Drive motion frequency behavior

The QMG drive axis was excited with varying *AC* voltage amplitudes at a V_{dc} of 10 V and 0 V net tuning voltage. Using a Zurich Instruments HF2LI lock-in amplifier frequency response sweeper, slow frequency sweeps centered over a 0.25 Hz window measured demodulated amplitude with 2,500 points. Using Eqs. (4.3)-(4.6) and the parameters in Table 4-2 for a measured drive frequency of 3,540 Hz, with a measured room temperature Q of 705k, a nominal 16 μm amplitude was modeled and achieved at maximum *AC* drive voltage amplitude of 55 mV. Beyond 55 mV the QMG begins to exhibit the onset of pull-in behavior for both the model and sweep measurements. Figure 4.3-3 plots the frequency behavior for FEA and modeled comb softening with the modified modal mass parameter to match the measured frequency. The k_{xx} and $k_{e,tip}$ (4.4), ((4.17)) are averaged over half sinusoidal displacement motion. The secondary y-axis of Figure 4.3-3 plots the ppm frequency change versus drive amplitude for both the model and measured values. Since MEMS CVGs are not perfectly fabricated and the CVG evaluated here has a Δf of 3.8 Hz, frequency behavior over drive with varying tuning voltage is informative for subsequent closed-loop CVG control.

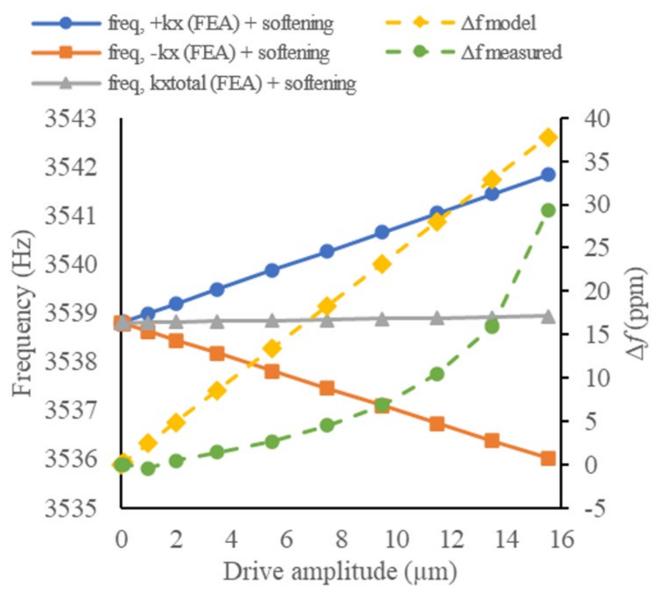

Figure 4.3-3 Modeled frequency nonlinearity with FEA springrates over half oscillation period ($+k_x$ and $-k_x$), the combined affect of the full oscillation period, and the parts per million (ppm) change as compared to the measured value when operating at 10 V_{dc} with 0 V net tuning voltage.

Figure 4.3-4 plots the ppm change in frequency over 40 V bias tuning range which provides ~4.3 Hz frequency tuning. At voltages beyond 40 V magnitude, pull-in phenomen may arise since the calculated static pull-in voltage for the combined symmetric parallel plate and comb tips is 56 V. From [83] a convervative assumption for dynamic pull-in is 10% lower than the static value. Both the drive and sense axes have the same applied tuning voltage, avoiding the mode-matched condition with increasing tuning voltage. Although the symmetric parallel plate tuners add to negative Duffing, their overall contribution is scaled similarly to the mechanical nonlinearity as well as the comb tip softening, thereby having minimal net impact on linear frequency operation.

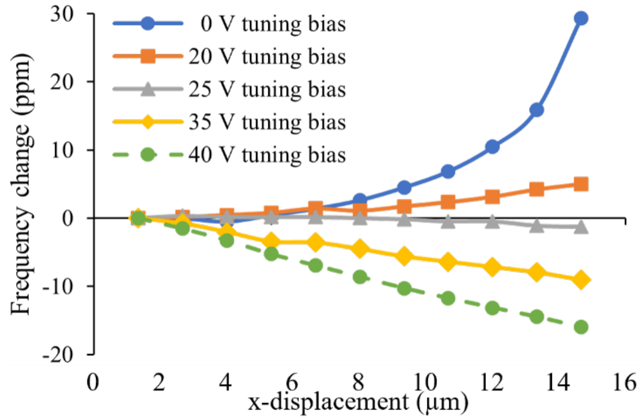

Figure 4.3-4 QMG frequency change over various drive motion amplitudes range from15-16 µm at 10 V_{dc}. AC drive amplitude ranged from 5-55 mV. Symmetric parallel plate tuning voltages ranging from 0-40 V (below $V_{pull\text{-}in}$) are applied to both the drive and sense axis keeping the modes separated during frequency.

4.3.4 Closed-loop Coriolis vibratory gyroscope measurements.

To show that increasing CVG drive amplitude improves ARW performance, the QMG was operated as a mode-matched gyroscope in closed-loop force-to-rebalance control performed using the Toyon Research Corporation front-end and power conditioning electronics and controlled with the Zurich Instruments HF2LI lock-in amplifier. The closed-loop control operates with automatic gain control on the drive channel with quadrature nulling and force-to-rebalance on the sense channel [70], [73], [52]. The forcer transducers – QMG drive, quadrature nulling, and force-to-rebalance – are all capacitive combs. Similarly, the drive and sense motion pickoffs are all combs. Both the forcer and pickoffs are of equal number and total capacitance. The closed loop approach using the lock-in amplifier is further described in [87] and schematically shown in Figure 4.3-5.

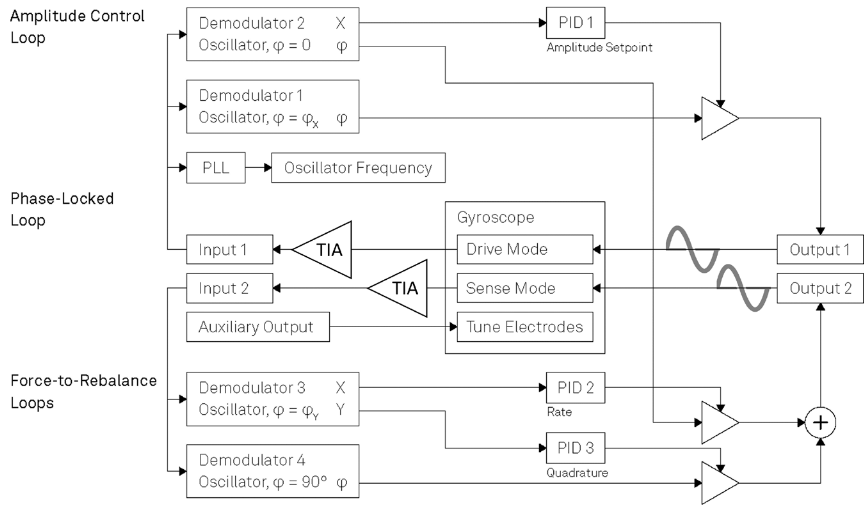

Figure 4.3-5 Gyroscope control with both closed-loop drive-mode and closed loop sense-mode. This mode is usually called force-to-rebalance (FTR). With FTR, the rate and quadrature output of the sense mode are suppressed by means of feedback control. The necessary feedback force is a measure of the rate of angular rotation. *Reproduced with permission from Zurich Instruments Application Note: Control of MEMS Coriolis Vibartory Gyroscope [87].

Scale factor was measured over various drive pickoff voltages at room temperature with input rotation rates up to 1 °/s. The expected full rate range at maximum drive amplitude is anticipated to be not much greater than 1 °/s where the same drive and force-to-rebalance noise levels are maintained. Above 1 °/s both the lock-in's analog to digital conversion range as well as the drive and force to rebalance digital to analog converter ranges have to be scaled by 10×. Absolute drive displacement cannot easily be inferred during mode-matched closed-loop operation because of quadrature and force-to-rebalance. Therefore, the maximum drive amplitude is set to be -20 ppm of its room temperature frequency – based on 36.5 V tuning voltage and results from Figure 4.3-4. A -20-ppm frequency shift represents a maximum drive sense amplitude of 280 mV. The results for *ARW* and *BI* are shown in Table 4-3. Although zero rate output bias voltage changes over drive amplitude voltage setpoint, the raw rate bias output maintains 34-40 °/hr bias die to larger scale factors with increasing drive setpoint amplitude. Table 4-3 provides both Allan deviation (ADEV) and power spectral density (PSD) slope fit methods for determination of ARW and BI [94]. The MATLAB™ *pwelch* function using the *'maxhold'* option was used to obtain conservative estimates for ARW and PSD. The '*maxhold*' option keeps the maximum spectrum estimate at each frequency bin of all segments. These estimates are ~2× higher than ADEV slope fitting.

TABLE 4-3 QMG ARW AND BI RESULTS AT VARIOUS DRIVE VOLTAGE SENSE SETPOINTS.

Drive sense (mV)	*freq (Hz)*	*ARW (°/√hr)*		*BI (°/hr)*	
		ADEV	**PSD**	**ADEV**	**PSD**
40	3534.44	0.0051	0.0087	0.22	0.26
80	3534.43	0.0023	0.0039	0.14	0.19
120	3534.42	0.0013	0.0027	0.12	0.12
160	3534.41	0.0011	0.0027	0.11	0.18
200	3534.40	0.0009	0.0023	0.10	0.16
240	3534.39	0.0007	0.0015	0.09	0.12
280	3534.37	0.0005	0.0011	0.08	0.10

Figure 4.3-6a-b plots zero rate PSD (a) and ADEV (b) of the QMG operating at 280 mV drive pickoff voltage and the respective ARW and ADEV results are shown in the last row of Table 4-3. The rate ramp seen in Figure 4.3-6 is believed to be due deterministic room temperature changes during data acquisition and could be compensated with temperature. To the author's knowledge, the ADEV fit for ARW is the best published results for silicon MEMS and considered state-of-the-art. However, the values listed in Table 4-3, thermomechanical angle random walk (ARW_{MTN}, Eq. (4.1)) with a $\Delta\omega = 0$ is still an order of magnitude lower than the measured 0.0005 °/√hr. Electronic noise and $\Delta\omega \neq 0$ are two sources of ARW, where electronic ARW is

the most dominant source, and these noise sources add (root sum squared) to the total ARWs list in Table 4-3 [60].

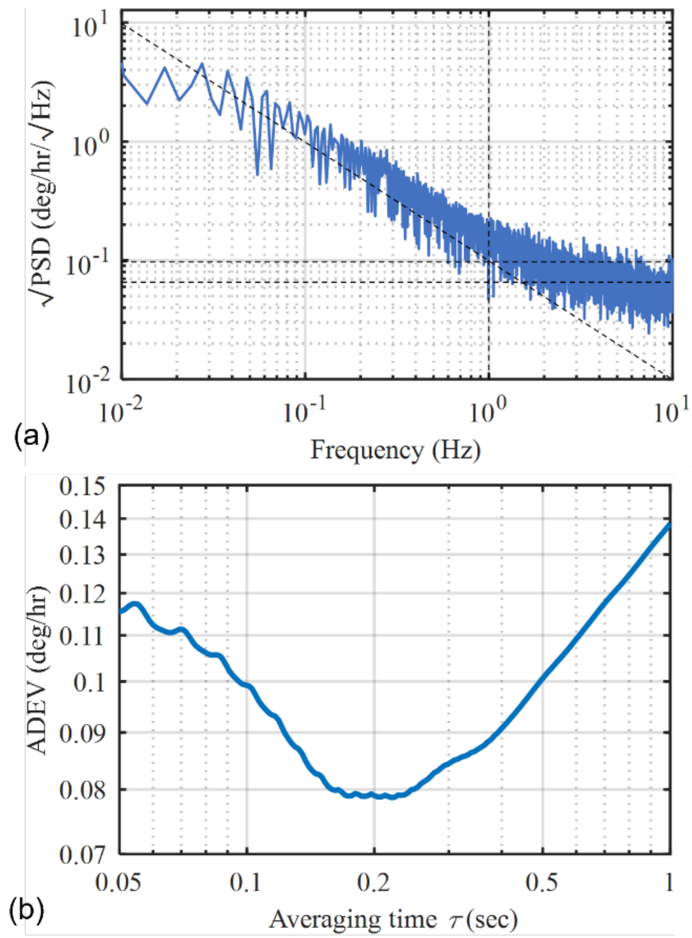

Figure 4.3-6 Top PSD plot using Matlab™ *pwelch* function *'maxhold'* condition and bottom ADEV plot. The QMG is driven to sense setpoint voltage of 280 mV. The PSD and ADEV plots are curve fitted to determine ARW and BI [93].

Comparing the results in work to other published work, Table 4-4 is a list comparing various miniaturized gyroscopes. The rows are categorized first by 2D silicon MEMS mode-matched, followed by 2D silicon mode-split tuning fork gyroscopes, miniaturized nuclear magnetic resonance gyroscopes, integrated photonics gyroscopes, 3D microscale glass blown gyroscopes, and finally the work published here.

TABLE 4-4 MEMS AND NON-MEMS MINIATURIZED GYRSOCOPES REPORTED IN THE LITERATURE

Author	Type	ARW (°/√hr)	BI (°/hr)	Die size
Aksari [22]	QMG mode-matched**	0.0058	0.066	8 × 8 × 0.6
Challoner [2]	DRG mode-matched**	0.0035	0.012	8 × 8 × 0.6*
Xu [3]	DRG mode-matched**	0.0048	0.015	8 × 8 × 0.6*
Safran [44]	Concentric mass mode-matched**	0.004	0.007	n.a.
Hamelin [47]	BAW gyro mode-matched**	0.07	4.2	< 1 × 1 × 0.6*
Koenig [45]	TFG mode-matched**	0.016	0.021	n.a.
Endean [4]	TFG mode-split**	0.003	0.01	n.a.
Gadola [8]	NEMS TFG mode-split**	0.004	0.02	1.45 × 0.91 × 0.6*
Walker [48]	Nuclear Magnetic Resonance	0.005	0.02	n.a.
Gundavarapu [49]	Optical MEMS**	8.52	58.7	42 × 45 × 0.6*
Cho [9]	3D Glass Blown HRG	0.00016	0.0014	10 × 10 × 3*
Wang [12]	3D Glass Blown HRG	0.03	n.a.	10 × 10 × 3*
This work	QMG mode-matched**	0.0005	0.08	8 × 8 × 0.6

assumed 600 μm thick wafer*
batch fabrication process**

4.3.5 Discussion

The results reported here illustrate the sentiment that was discussed in "*Flat is not Dead" [70]* and in "*Silicon MEMS inertial sensors evolution over a quarter century*" [101]. MEMS gyroscope ARW has only improved by a factor of 1000× over the last

25 years and have recently stagnated over the past five years, however, most of the MEMS gyroscopes reported are nowhere near their respective ARW_{MTN} limit. Mode-split gyroscopes have improved recently at a faster rate than their mode-matched counterparts, approaching and surpassing mode-matched gyroscopes in ARW and bias stability [55]. Academic fabrication facilities and lack of commercial demand are potential reasons why mode-matched CVGs have stagnated.

Since gyroscopes operate like two degenerate resonators, recent advancements in low drift silicon oscillators are further proof that there's plenty of performance left to squeeze out of silicon [102] especially related to bias drift for both mode-split and mode-match gyros. The ARW result here is believed to be limited by electronic angle white noise, which is a combination of sense electronic noise, Δf, and voltage noise – further improvements could be realizable.

This work reports state-of-the-art MEMS CVG ARW performance 10× lower than prior published QMG work. The author acknowledges that at a 6-Hz system bandwidth, the QMG here has limited rate range that has not been identified. Scale factor tests up to 1 °/s rate input were well with the drive amplitude's rate range, but the author has yet to extend scale factor testing to larger input calibration rotation rates.

4.4 Summary

This study presents significant advancements in the redesign of a quadruple mass Coriolis vibratory gyroscope, aimed at reducing nonlinear transduction mechanisms and enhancing noise reduction at higher motion amplitudes. The implementation of various improvements, such as redesigned folded flexures, linearized antiphase coupler, linear combs, force-balanced electrostatic tuners, and vacuum packaging, has proven successful in achieving an ADEV-estimated ARW performance of 0.0005 deg/√hr and an uncompensated bias instability of 0.08 deg/hr. These findings have implications for improving the performance and precision of vibratory gyroscopes, making them more suitable for applications in virtual reality, autonomous vehicles, and environments without GPS availability.

Overall, the results presented in this study contribute to the field of inertial MEMS technology, where precision and noise reduction are crucial. By addressing nonlinear transduction mechanisms and implementing design improvements, this work has demonstrated the potential for significant noise reduction, leading to higher performance gyroscopes. These advancements hold promise for various applications where accurate and reliable inertial sensing is essential, benefiting industries such as navigation, robotics, and aerospace. Further research and development in this area is likely to lead to even more sophisticated and precise MEMS gyroscopes for future technological advancements.

Chapter 5: Piezoelectric Enhanced QMG

This chapter introduces a novel approach to reduce QMG bias instability by tuning the intrinsic Quality (Q) factor. The quality factors for degenerate modes in as-fabricated Microelectromechanical Systems (MEMS) gyroscopes are never identical due to fabrication errors and other manufacturing or material imperfections. Teledyne DALSA, a high-performance inertial MEMS 200 mm foundry, has reported an average Q mismatch of 7% for their foundry service [104]-[105]. On the other hand, their as-fabricated frequency split is much tighter, at approximately 500 ppm. Some methods exist to trim the as-fabricated Q, but these can be costly, time-consuming, and may require additional mechanical structures or physical modification to the MEMS mechanical layer [106]-[108]. Even the best-performing hemispherical resonator gyroscopes, with nearly flawless manufacturing, still exhibit noticeable Quality factor mismatches that are identified dynamically and mechanically trimmed post-production [109].

The bias equation introduced in Chapter 1.5 and reiterated below as, Eq. (5.1), identifies two sources of gyroscope angular rate bias: 1) angular rate bias due to the difference in degenerate mode $\Delta\left(\frac{1}{\tau}\right)$ and 2) the quadrature signal that leaks into the angular rate bias signal because of rate sense pickoff alignment error and frequency mismatch. When cross-axis stiffness is set to zero by quadrature nulling, the difference in the inverse of the degenerate mode τ becomes the predominant source of angular rate bias.

$$Bias = \frac{1}{2a_g}\Delta\left(\frac{1}{\tau}\right)\sin(2\theta_\tau) + \omega\Delta\omega\cos 2\theta_\omega q\frac{1}{2a_g} \quad (5.1)$$

One way to visualize bias drift due to inverse τ mismatch is by imagining two bells with different ringdown times, placed at a radial distance of 10 feet in front of a listener, each 5 feet apart. If the listener closes their eyes and both bells are struck simultaneously, the sound will seem to radiate directly from the center point between the two bells. As the sound decays, differing ringdown times would create the illusion of the bells slowly rotating around the listener at the 10-foot radius. Just as a listener might turn their head to follow the sound, veering towards the bell with the longer ringdown time, a gyroscope might display a similar bias. If both bells had the exact same ringdown time, the sound would appear to emanate from the center point of the two bells, and there would be no perceived rotation.

The ringdown time constant, τ, and quality factor are closely related, only differing by the product of frequency and pi. Therefore, if quality factor mismatches are tuned to match, gyroscope angular rate bias can be improved. This is akin to the scenario with the bells where simultaneous ringdown creates no perceived rotation.

Subsequent sections will delve into the feasibility of this process, its limitations, and demonstrate, using frequency data from the QMG evaluated in Chapter 4, that an improvement in bias instability can be realized if quality factor tuning is employed.

5.1 *Intrinsic quality factor tuning with piezoMEMS*

Quality factor tuning generally falls into two categories: 1) intrinsic quality factor tuning and 2) effective quality factor tuning. Intrinsic quality factor tuning modifies a resonator's thermomechanical force, yielding an amplitude spectral density with a lower noise floor and a higher quality factor. In contrast, effective quality factor tuning changes the measured quality factor by introducing an additional energy source or sink external to the resonating system, as described in works [106]-[108]. The intrinsic Q can be modified via mechanical methods, where the resulting thermal mechanical noise floor is reduced, correspondingly increasing the intrinsic Q. Both intrinsic and effective Q tuning will alter the resonator's transfer function. However, only intrinsic Q tuning will impact the amplitude spectral density noise floor [103].

The subsequent sections contend that piezoelectric tuning of Q, focusing on intrinsic Q, generates less noise compared to methods that tune the effective Q. The Army Research Laboratory's cluster tool for the sputtered lead zirconate titanate ($PbZr_{0.52}Ti_{0.48}O_3$) (PZT) process produces a material capable of tuning the quality factor with an increasing DC polarization field, V_{bias}. This distinctive property can potentially demonstrate Q matching and stabilization of the drive and sense axes by tuning Q in both axes, creating a $\Delta\left(\frac{1}{\tau}\right)$ condition that nears zero. The axis with the lower Q will have a higher applied DC polarization field than the axis with the higher Q, and they can be tuned to match the $\Delta\left(\frac{1}{\tau}\right)$ condition. An example of unloaded Q tuning with DC bias voltage is illustrated in *Figure 5.1-1*. Here the unloaded Q being tuned is on a MHz length extension resonator and its unloaded *fQ* is much lower than the QMG results presented in Chapter 3 and 4. This is due to the large volumetric ratio of PZT to the structural silicon layer where PZT is a known low *Q* material.

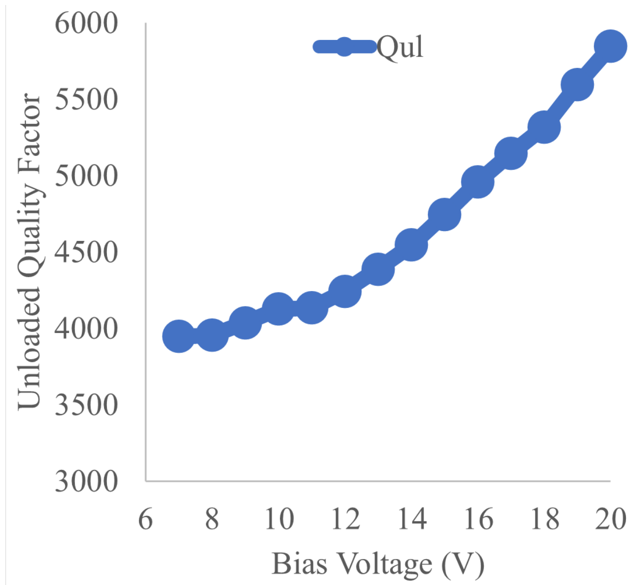

Figure 5.1-1. Unloaded quality factor as a function of applied DC bias voltage for an example MHz length extension PZT resonators [110]. Similar Q tuning behavior is anticipated on the lower frequency QMG.

The $\Delta\left(\frac{1}{\tau}\right)$ term assumes a θ_τ misalignment between the pickoff axes and the principal axis of damping, as previously shown in Figure *1.5-2*. If the principal axes of damping perfectly aligns with the pickoff axes then the *Q*-matched condition will eliminate zero-rate bias and further reduce bias instability. However, the θ_τ misalignment is never perfectly aligned to the pickoff axis inducing some error. Eq. (5.2)-(5.4) are derived from the dynamic equation for a two degree of freedom oscillator discussed in Chapter 1.5. Because *x* and *y* direction are never perfectly aligned with the principal axis of damping the cross-axis term in Eq. (5.2) will never be zero. However, tuning the τ_x and τ_y to match will still bring the eigenvalues, shown in Eq. (5.3), closer to the matching condition and steer the eigenvectors, Eq. (5.4), closer to the tuning axes.

$$\begin{bmatrix} \frac{2}{\tau} + \Delta\left(\frac{1}{\tau}\right)\cos(2\theta_\tau) & -\Delta\left(\frac{1}{\tau}\right)\sin(2\theta_\tau) \\ \Delta\left(\frac{1}{\tau}\right)\sin(2\theta_\tau) & \frac{2}{\tau} - \Delta\left(\frac{1}{\tau}\right)\cos(2\theta_\tau) \end{bmatrix} \begin{bmatrix} x \\ y \end{bmatrix} \tag{5.2}$$

$$\lambda_{1,2} = \frac{2}{\tau} \pm \sqrt{\left(\Delta\left(\frac{1}{\tau}\right) cos(2\theta_\tau)\right)^2 + \left(\Delta\left(\frac{1}{\tau}\right) sin(2\theta_\tau)\right)^2} \tag{5.3}$$

$$v_{1,2} = \left(\frac{\Delta\left(\frac{1}{\tau}\right) cos(2\theta_\tau)}{\Delta\left(\frac{1}{\tau}\right) sin(2\theta_\tau)} \pm \frac{\sqrt{\left(\Delta\left(\frac{1}{\tau}\right) cos(2\theta_\tau)\right)^2 + \left(\Delta\left(\frac{1}{\tau}\right) sin(2\theta_\tau)\right)^2}}{\Delta\left(\frac{1}{\tau}\right) sin(2\theta_\tau)}, 1 \right) \tag{5.4}$$

It's vital to reiterate here that while tuning the as-fabricated *Q* mismatch will improve the anisodamping matrix of Eq. (5.2), if the principal axis of damping is not aligned with the tuning axes, then equalizing the principal damping eigenvalue will not be possible. However, improvements in *Q* matching will still be observable due to the reduction in $\Delta\left(\frac{1}{\tau}\right)$.

5.2 Q degradation due to PZT integration

Sputtered lead zirconate titanate ($PbZr_{0.52}Ti_{0.48}O_3$) (PZT) is characterized as a low *Q* material, as evidenced by the unloaded *Q* results for an MHz length extension resonator shown in *Figure 5.1-1*. Consequently, when integrating PZT into the QMG CVG, potential *Q* degradation must be examined. This necessitates an analysis of the tradeoffs between the effective tuning of *Q* and the degradation of *Q* due to integration. Regions on the QMG need to provide space for electrode integration and nearby signal routing, have relatively low mechanical coupling, and be broad enough to accommodate future fabrication milling processes. The guided folded flexure regions depicted in *Figure 5.2-1* fulfill these requirements. The anchors surrounding all eight guided folded flexure regions offer substantial electrode area for transduction and signal routing, and the 20 µm width of the folded flexure will suit future fabrication process tolerances. Furthermore, low mechanical coupling is shown with only 1.05 µm *y* displacement for 16 µm *x* displacement.

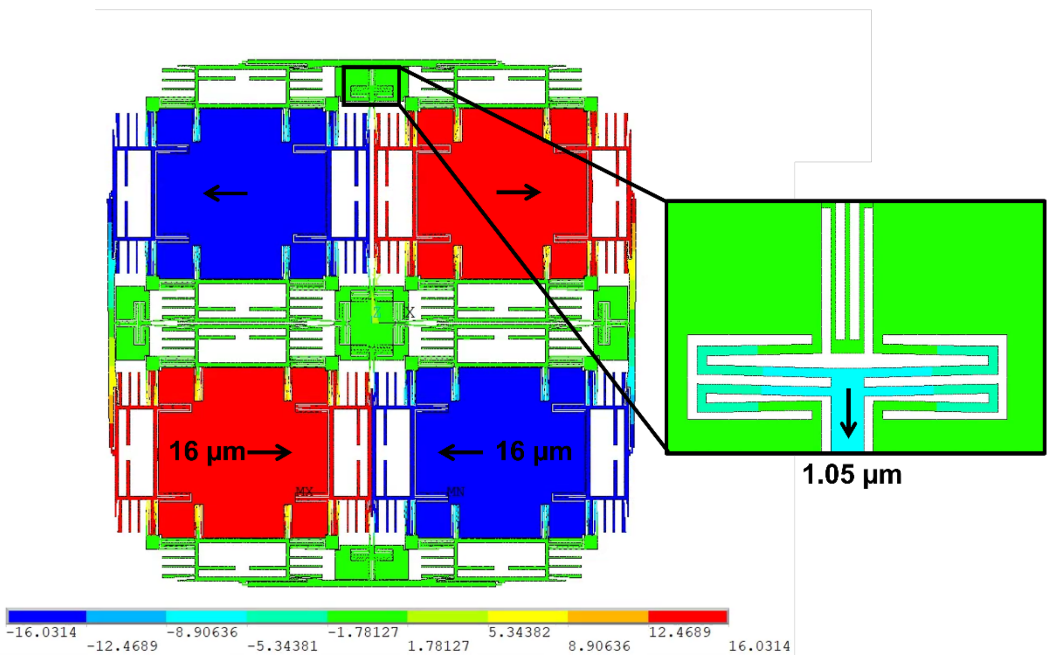

Figure 5.2-1. FEA of QMG antiphase motion of 16 µm x drive displacement. The inset image zooms in on the guided folded flexure discussed in Chapter 4.2.3 illustrating an exaggerated *y* motion. Per 16 µm of Coriolis proofmass displacement the guided folded flexure moves 1.05 µm in the *y* direction. PZT integration onto the guided folded flexure is anticipated to have moderate impact on Q due to the low coupling.

Finite Element Analysis (FEA) simulations were performed to examine the effect of PZT volumetric integration on *Q* degradation and tuning range. *Figure 5.2-2*a illustrates green PZT patch length with *x* length and *Figure 5.2-2*b depicts PZT patch size covering the entire folded flexure.

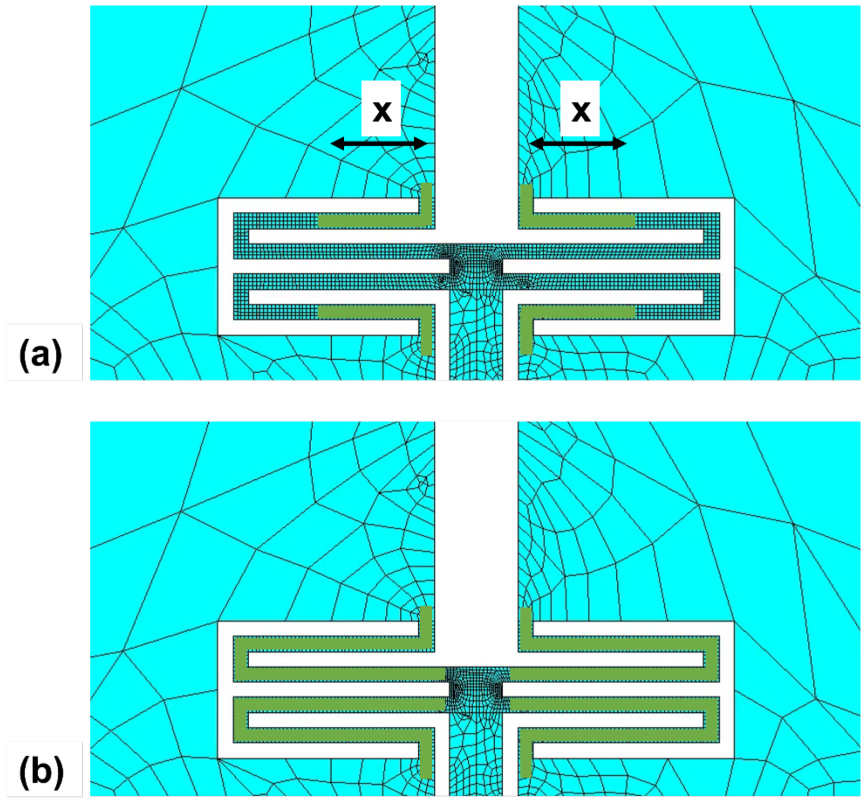

Figure 5.2-2. The green overlay on the guided folded flexure depicts the regions where PZT can cover. (a) the length dimension x is varied and the total Q degradation is simulated using volumetric Q ratios of the PZT and 100 μm thick silicon. (b) PZT cover the entire guided folded flexure.

The FEA simulations assume a starting *Q* for the QMG to be 1M. Two different PZT material *Q* values were examined providing a best-worst case plot shown in Figure 5.2-3. The lowest and highest ARL-produced PZT Q will reduce the overall QMG *Q* factor by 30-40% with a patch length of 120 μm. Conversely, each material can enhance Q by 10% with a maximum DC bias voltage of 15 V. Smaller PZT patch lengths will decrease *Q* degradation due to material integration, but will also limit the *Q* tuning range. Therefore, thoughtful consideration is needed when tuning as-fabricated *Q* mismatch. Substantial datasets of wafer mapping for silicon-only as-fabrication Q mismatch need to be quantified before determining the PZT patch length. Moreover, the integration of PZT could potentially worsen the as-fabricated Q mismatch, necessitating further adjustments to the PZT patch length.

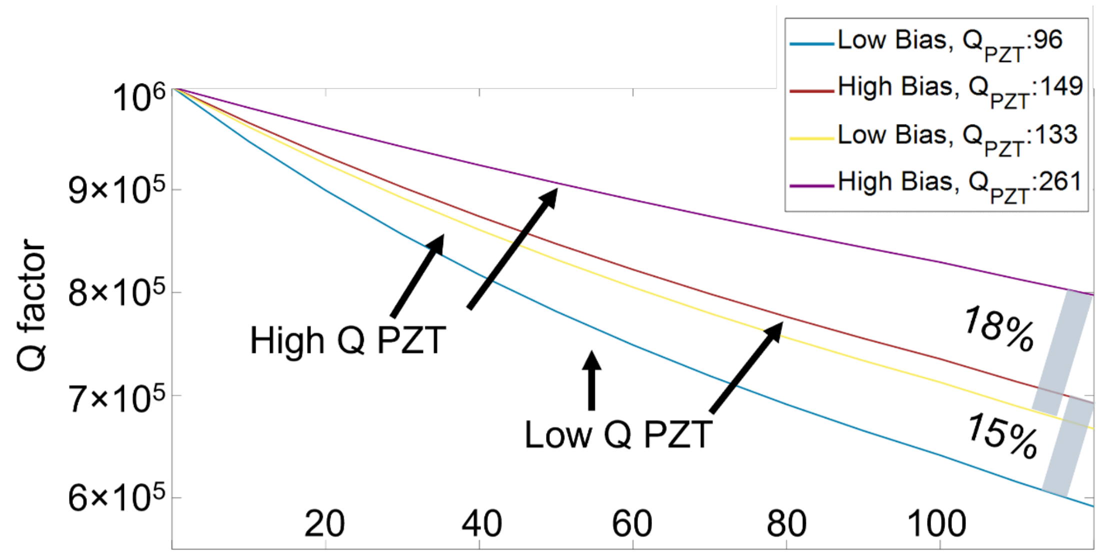

Figure 5.2-3. Volumetric Q model of loss in total Q-factor from PZT material integration onto the guided folded flexure shown in Figure 5.2-2*. This models increases length x, shown in* Figure 5.2-2*, by 10 µm for each FEA simulation. Two different PZT Q properties are simulated illustrating the range of Q degradation and tuning (low to high bias) with curves from blue to purple. The PZT properties have been empiracally measured for the various PZT recipes at ARL.*

5.3 Frequency drift correlation and bias reduction through quality factor tuning.

The bias output of the mode-matched gyroscope is determined by several factors: the drive and sense frequency, f_x and f_y drive and sense, Q_x and Q_y, quadrature, q, drive amplitude, a, and the principal axes of damping and frequency, θ_τ and θ_ω, respectively, as given in Eq. (5.1). Zero rate bias output and bias stability are both very important measures of a high-performance gyroscope. A perfectly bias stable gyroscope means that the output angular rate can be integrated without any drift, meaning that orientation can accurately be tracked for any mission duration. However, drift is always present in any physical system. To understand how angular rate bias drifts, it's instructive to look at known time dependent variables of Eq. (5.1). Differentiating Eq. (5.1) where frequency and quality factor are assumed to be functions of time, the follow equation is derived:

$$\frac{d}{dt}Bias = \frac{\pi}{2a_g}\left(\frac{\dot{f}_x Q_y - \dot{f}_y Q_x}{Q_x Q_y} + \frac{f_y \dot{Q}_y {Q_x}^2 - f_x \dot{Q}_x {Q_y}^2}{{Q_x}^2 {Q_y}^2}\right)\sin(2\theta_\tau) + q\frac{1}{2a_g}\cos 2\theta_\omega\left[\omega_x \dot{\omega}_x - \omega_y \dot{\omega}_y\right] \quad (5.6)$$

The first term, a product of $\sin(2\theta_\tau)$, arises from Q and frequency drift. Meanwhile, the second term, a product of $\cos(2\theta_\omega)$, stems from the misalignment of the sense and drive pickoff axes and frequency mismatch, resulting in quadrature error being detected on the rate signal. As Q doesn't affect the second term, it will be disregarded in the following analysis.

Frequency data of the QMG, reported in Chapter 4, was gathered over two hours using a Zurich Instruments HF2LI lock-in amplifier and shown in Figure *5.3-1*. Each frequency, f_x and f_y, had its own phase-locked loop (PLL) for the mode-matched QMG, permitting them to drift independently. Using the collected data from Figure *5.3-1* and plugging it into Eq. (5.6), assuming a nominal Q of 500,000 with Q_x and Q_y mismatch ranging from 0.1% to 10%, the bias instability can be computed via the Allan deviation method described in Chapter 1.5. The bias instability as a function of Q mismatch is plotted in Figure 5.3-2, illustrating a bias instability of 1.85 °/hr for a 10% Q mismatch and a 0.02 °/hr bias instability for a 0.1% Q mismatch.

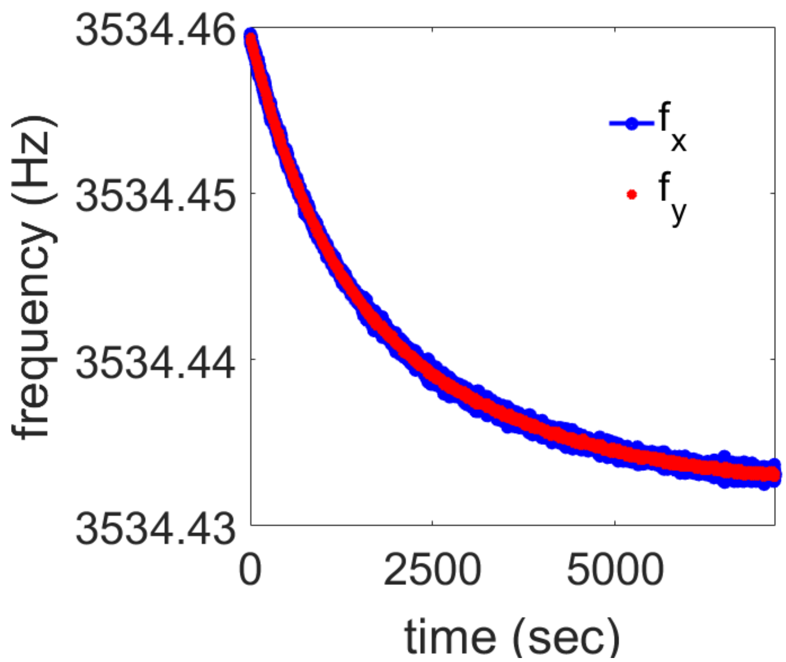

Figure 5.3-1. The x and y frequencies over time of a mode-matched QMG. Two separte PLLs are used to follow each frequency. The f_x and f_y drifts are nearly 100% correlated. Q tuning for with increased Q matching will result in a decrease in bias instability for bias drift attributed to angular rate channel.

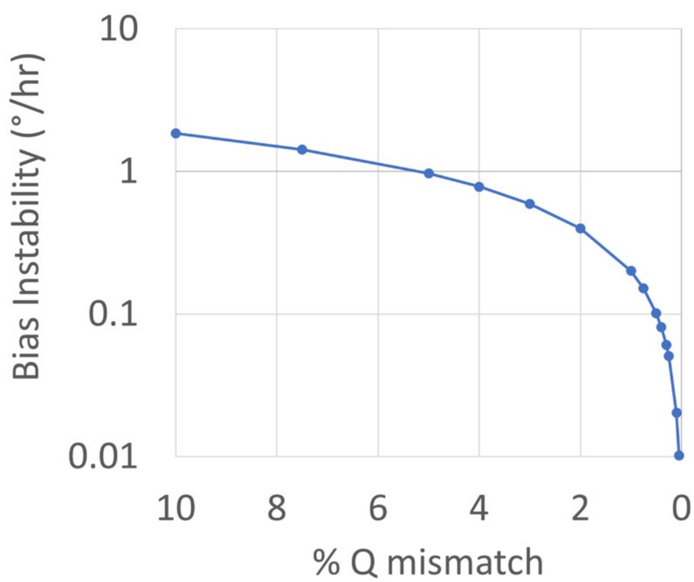

Figure 5.3-2. Using the relationship shown in Eq. *(5.6)*and using the measured frequency drift from Figure 5.3-1, bias instability is shown to decrease with decreasing %Q mismatch. With a constant Q mismatch of 0.1%, bias instability is simulated to reduce to 0.018 °/hr. These values are an upper limit since the computer bias instability only considers freqeuncy drift as the mechanism for bias drift.

Using a similar method with the data from *Figure 5.3-1* and Eq. (5.6), a plot of bias instability versus quality factor for a range typical for silicon MEMS CVGs can be generated. Figure 5.3-3 displays bias instability as a function of *Q*, with sloped lines representing various *Q* mismatch values. The QMG discussed in this work, along with typical Teledyne DALSA *Q* mismatch, is overlaid on this plot. One note of caution is that tuning the quality factor to match becomes progressively more challenging at higher *Q* values. External factors such as electronic loading and minor energy sinking can create *Q* noise, where a 0.5% change in *Q* for *Q*'s greater than 500,000 is equivalent to fluctuations of an external Q >10^8. Similarly, for nominal *Q*'s of 100,000, a *Q* fluctuation of 0.1% is equivalent to an external Q sink of Q >10^8.

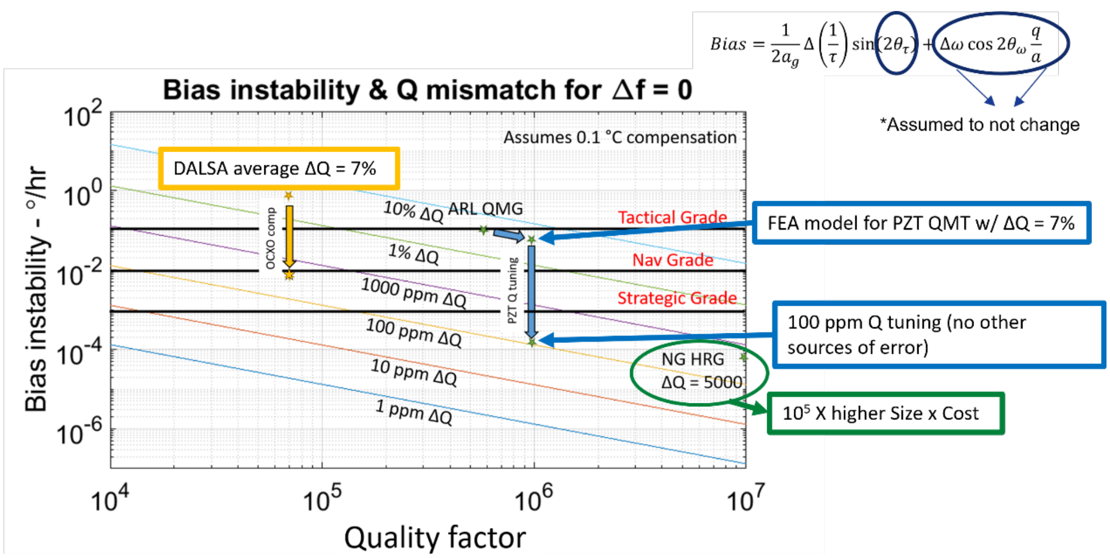

Figure 5.3-3. Bias instability as a function of quality factor where the sloped lines indicate the Q mismatch amount. When only considering frequency drifts, MEMS CVG bias instability performance can approach the strategic level for 1000 ppm mismatch and *Q*'s near 1M. Teledyne DALSA MEMS foundry routinely produce degenerate resonator *Q* values with an across wafer average mismatch of 7% [105], thus providing motivation for PZT Q tuning. The HRG circled in green highlights its performance relative to a very small *Q* mismatch.

Quality factor tuning of MEMS mode-matched CVGs represents an innovative approach to improving bias instability. By reducing angular rate bias instability, gyroscope orientation tracking is enhanced due to minimized integration of drift. Inertial measurement units produced for navigation, orientation tracking, and North finding can benefit from MEMS CVG Q tuning, as it has been demonstrated to decrease bias instability, leading to a lower drift solution. Future work towards this goal through the integration of piezoelectric may provide an effective path for tuning of intrinsic Q values with lower noise than alternative effective quality factor tuning approaches.

Chapter 6: Summary and Future Work

This dissertation describes the importance of high-performance MEMS CVG as an integral component for inertial measurement unit dead reckoning. IMU error drifts with cubic time and the gyroscope is the largest source of IMU error. Thus, the performance requirements demanded for navigation mainly fall onto the gyroscope.

Precision MEMS manufacturing in high-performance mode-matched gyroscopes is essential to minimize frequency mismatches between degenerate modes, eliminate surface damping on mechanical flexures, and reduce damping asymmetries. To achieve this, as-fabricated stiffness asymmetries must be minimized to tune the degenerate frequency modes precisely, aiming for zero frequency mismatch. This requires maintaining nanometer of x and y critical dimensions in MEMS flexure tolerancing. Pristine silicon surface during fabrication is necessary to decrease defect density and contamination, thereby increasing wafer yield.

One approach to reducing gyroscope angular rate noise, specifically angle random walk, is to increase the MEMS CVG drive amplitude. However, driving the CVG at large motion while maintaining considerable electrostatic transduction gain poses a challenge in multi-aspect ratio deep reactive ion etching. The DRIE process described in this research addresses this problem by developing morphed bulk and landing etches. An aspect-ratio independent DRIE has been developed, featuring a morphed bulk etch followed by a morphed landing etch. The landing etch maintains critical dimension requirements while minimizing notching at the buried oxide. The DRIE recipe developed produces vertical and smooth sidewalls and lands cleanly on the buried oxide.

Increasing the quality factor has been identified as a key mechanism to enhance MEMS CVG performance. To achieve this, vacuum packaging is essential to eliminate sources of Q degradation, such as viscous damping losses caused by gaseous components of air. Surface contaminants also contribute to Q degradation due to frictional losses, and vacuum packaging with high-temperature bakes helps remove surface contaminants.

The vacuum packaging work presented has successfully reduced the vacuum packaging pressure to state-of-the-art levels for leadless ceramic chip carrying physics packages. This improvement significantly enhances high-performance MEMS CVGs and improve the performance of physics packages, like chips scale atomic clocks, where sub-micro-torr ultrahigh vacuum is needed.

To decrease rate noise and effectively reduce angle random walk (ARW), the impact of increasing parameters like Q, drive frequency ω_x, Coriolis mass m, and drive amplitude A has been examined. The results of the deep reactive ion etching (DRIE) procedure demonstrated the feasibility of achieving large drive motion despite the challenges posed by multi-aspect ratio etch features. As a result, linearized transduction, which helps reduce nonlinearities associated with both mechanical and electrical effects, has been described. Mechanically, spring rates become nonlinear when MEMS folded flexures deflection reveals axial force behavior in their reaction forces. Additionally, folded flexure deformation behaves nonlinearly when the small angle assumption for $sin\ \theta$ no longer holds. Nonlinearities due to electrical transduction were also analyzed, discussed, and mitigated. By addressing these nonlinear transduction mechanisms and implementing design improvements, this work has demonstrated the potential for significant noise reduction through larger drive motion, and demonstrated best-in-class silicon MEMS CVG ARW of 0.0005 deg/√hr, which is state-of-the-art. A bias instability of 0.08 deg/hr has also been demonstrated which is on-par with the latest results in the literature.

Lastly, a novel approach to tuning intrinsic quality factor was discussed. By tuning as-fabricated quality factor mismatch between degenerate modes, bias instability can be reduced. quality factor tuning can be accomplished by incorporating unique lead zirconate titanate ($PbZr_{0.52}Ti_{0.48}O_3$) (PZT) developed at ARL into regions where the tradeoff between Q mechanical, Q tuning, and bias instability reduction are balanced. Modeling and the use of empirical frequency data provide justification of this approach for bias instability reduction. This approach is the first of its kind and research subsequent to this dissertation will hopefully demonstrate MEMS CVG Q tuning during closed-loop gyroscope operation.

6.1 Scientific Contributions

- Identified a repeatable process to vacuum package sensors in leadless ceramic chip carriers at pressures below 1 micro-torr.

- The custom vacuum packaging tool is now commercially available to the scientific community through Kurt J. Lesker company.
- Revealed to a major MEMS foundry *Q* improvements are realizable through lower wafer level vacuum packaging.
- The vacuum packaging results have gained interest at a major manufacturer of chip scale atomic clock where a similar tool might be procured.

- First in class and state-of-the-art silicon MEMS CVG angle random walk of 0.0005 deg/√hr has been demonstrated.
  - A 10× reduction in ARW could be achieved through large amplitude drive which could provide motivation to the high-performance MEMS CVG community to investigate similar methods to increase drive amplitude.
- Introduced a novel intrinsic quality factor tuning approach that balances as-manufacture *Q* mismatch and has been shown to improve bias instability with empirical frequency data.
  - The high-performance inertial MEMS community can use this approach to balance as-fabricated *Q* mismatch further eliminating bias drifts without the need for post-fabrication mechanical trimming or substantial design modifications.

6.2 Future work

- Design – increase drive and sense frequency to be above 10 kHz. Higher drive and sense frequency decreases sensitivity and susceptibility to vibration and rolls off at frequencies above 10 kHz. Tripling the frequency will require flexures to have 9× more stiffness. The linearity study laid out in Chapter 4 provides the framework to redesign the QMG to operate above 10 kHz. More flexures will need to be added and flexure width will have to be increased. Both flexure count and increasing width will affect linearity and lower Q_{ted} while drive frequency is increased. Ideally, the mechanical thermal noise ARW will remain similar to the results in Chapter 4, where Q_{ted} decreases proportionally to ω_x increase.

- Vacuum packaging – investigate higher temperature eutectic preforms, like 75 Au / 25 In with a eutectic at 485 °C. Higher temperature preform eutectics will enable higher physics package bakeout temperatures allowing the vacuum packaging recipe to both eliminate a pre-bake and vastly shorten the overall bakeout time.
- Fabricate and demonstrate bias instability improvement with Quality factor tuning when the QMG has PZT material integration. Investigate in-run zero-rate bias output stabilization with DC Quality factor matching. Furthermore, investigate Quality factor matching during in-run rate calibration as a control approach to bias adjustment. With this approach, two gyroscopes will be needed per axis where one gyroscope is used to determine rate and other uses that known angular rate to compensate zero-rate bias with Quality factor tuning.

- Design – cross axis frequency tuner. Investigate designs that allow for cross-axis frequency tuning for quadruple mass gyroscope architectures that will have minimal impact on gyroscope die footprint.
- Design – cross axis Q tuning. Investigate designs that would allow for cross-axis Quality factor tuning which will further align the principal axis of damping to the drive and sense pickoff axes.
- Closed loop thermal compensation for improvement in-run performance and stability revealing electronic flicker limitations. Temperature rate random walk currently dominates the perceived bias instability.
- Rate range – investigate rate range control limitations and tradeoffs between maximum forcer voltage, forcer voltage noise, and DC voltage.
- Use the above rate range study to determine drive comb spacing versus pickoff comb spacing. Redesign the QMG with smaller comb gap spacing and determine if the DRIE recipe developed can tolerate smaller gaps and longer over-etch in regions with larger gaps.

Bibliography

[1] O. J. Woodman, "An introduction to inertial navigation," Aug. 2007.

[2] https://vrscout.com/news/vr-headset-standalone-inside-out/

[3] https://www.darpa.mil/program/precise-robust-inertial-guidance-for-munitions

[4] https://en.wikipedia.org/wiki/History_of_navigation

[5] https://www.nature.com/news/2011/110131/full/news.2011.58.html

[6] https://en.wikipedia.org/wiki/Knot_(unit)

[7] Gould, Rupert T. (1923). The Marine Chronometer. Its History and Development (PDF). London: J. D. Potter. ISBN 0-907462-05-7.

[8] http://invention.si.edu/invention-time-and-navigation-0

[9] https://en.wikipedia.org/wiki/Robert_H._Goddard

[10] Y. Liu, M. Shi, and X. Wang, "Progress on atomic gyroscope," in *2017 24th Saint Petersburg International Conference on Integrated Navigation Systems (ICINS)*, 2017, pp. 1–7.

[11] A. Madni, L. E. Costlow, and S. J. Knowles, "Common design techniques for BEI GyroChip quartz rate sensors for both automotive and aerospace/defense markets," *Sensors Journal, IEEE*, vol. 3, pp. 569–578, 2003.

[12] https://www.siliconsensing.com/products/gyroscopes/crm-pinpoint/

[13] V. M. N. Passaro, A. Cuccovillo, L. Vaiani, M. De Carlo, and C. E. Campanella, "Gyroscope Technology and Applications: A Review in the Industrial Perspective," *Sensors*, vol. 17, no. 10, p. 2284, 2017.

[14] D. Rozelle, "The Hemispherical Resonator Gyro: From Wineglass to the Planets," *Adv. Astronaut. Sci.*, vol. 134, pp. 1157–1178, 2009.

[15] DJ. M. Gray et al., "Hemispherical micro-resonators from atomic layer deposition", Journal of Micromechanics and Microengineering, vol. 24, no. 12, pp. 125028, 2014.

[16] A. D. Challoner, H. H. Ge, and J. Y. Liu, "Boeing disc resonator gyroscope," *Rec. - IEEE PLANS, Position Locat. Navig. Symp.*, pp. 504–514, 2014.

[17] A. A. Trusov, I. P. Prikhodko, S. A. Zotov, A. R. Schofield, and A. M. Shkel, “Ultra-high Q silicon gyroscopes with interchangeable rate and whole angle modes of operation,” *Proc. IEEE Sensors*, pp. 864–867, 2010.

[18] I. P. Prikhodko, S. A. Zotov, A. A. Trusov, and A. M. Shkel, “Foucault pendulum on a chip: angle measuring silicon MEMS gyroscope,” in *2011 IEEE 24th International Conference on Micro Electro Mechanical Systems*, 2011, pp. 161–164.

[19] D. Endean et al., "Near-Navigation Grade Tuning Fork MEMS Gyroscope," Inert. 2019 - 6th IEEE Int. Symp. Inert. Sensors Syst. Proc., pp. 1-4, 2019.

[20] B. R. Johnson et al., "MEMS IMU for GPS-Denied Navigation."

[21] B. Johnson et al., "Development of a Navigation-Grade MEMS IMU," Inert. 2021 - 8th IEEE Int. Symp. Inert. Sensors Syst. Proc., pp. 2021-2024, 2021.

[22] https://eri-summit.darpa.mil/docs/ERIsummit2020/posters/26P_PRIGM_Polcawich_Honeywell_Poster.pdf

[23] G. ~H. Bryan, “The Waves on a Rotating Liquid Spheroid of Finite Ellipticity,” *Philos. Trans. R. Soc. London Ser. A*, vol. 180, pp. 187–219, 1889.

[24] IEEE, *IEEE Standard Specification Format Guide and Test Procedure for Single –Axis Interferometric Fiber Optic Gyros*, vol. 1997. 1998.

[25] R. P. Leland, “Mechanical-thermal noise in MEMS gyroscopes,” *IEEE Sens. J.*, vol. 5, no. 3, pp. 493–500, 2005.

[26] Rudyk AV, Semenov AO, Kryvinska N, Semenova OO, Kvasnikov VP, Safonyk AP. Strapdown Inertial Navigation Systems for Positioning Mobile Robots—MEMS Gyroscopes Random Errors Analysis Using Allan Variance Method. Sensors. 2020; 20(17):4841. https://doi.org/10.3390/s20174841

[27] K. Kunal and N. Aluru, Akhiezer damping in nanostructures, Phys. Rev. B 84, 245450 (2011).

[28] R. Rameshan, “Evaluation of Non-Evaporable Getters for High Vacuum Hermetic Packages,” *NEPP Progr. Doc.*, pp. 1–31.

[29] A. A. Trusov, A. R. Schofield, and A. M. Shkel, “A substrate energy dissipation mechanism in in-phase and anti-phase micromachined z -axis vibratory gyroscopes,” *J. Micromechanics Microengineering*, vol. 18, no. 9, p. 95016, 2008.

[30] R. B. Bhiladvala and Z. J. Wang, “Effect of fluids on the Q factor and resonance frequency of oscillating micrometer and nanometer scale beams,” *Phys. Rev. E*, vol. 69, no. 3, p. 36307, Mar. 2004.

[31] Z. Gan, D. Huang, X. Wang, D. Lin, and S. Liu, “Getter free vacuum packaging for MEMS,” *Sensors Actuators, A Phys.*, vol. 149, no. 1, pp. 159–164, 2009.

[32] D. Sparks, J. Trevino, S. Massoud-Ansari, and N. Najafi, “An all-glass chip-scale MEMS package with variable cavity pressure,” *J. Micromechanics Microengineering*, vol. 16, no. 11, pp. 2488–2491, 2006.

[33] I. P. Prikhodko, B. R. Simon, G. Sharma, S. a Zotov, A. a Trusov, and A. M. Shkel, “High and Moderate-Level Vacuum Packaging of Vibratory MEMS,” *Int. Symp. Microelectron.*, no. Imaps, pp. 705–710, 2013.

[34] https://www.palomartechnologies.com/sst-3150-high-vacuum-furnace.

[35] Kurt J. Lesker Company, www.lesker.com, Jefferson Hills, PA.

[36] POSIFA Microsystems, Inc., http://www.posifamicrosystems.com/, San Jose, CA.

[37] R. R. Knight and R. G. Polcawich, “A new approach to vacuum packaging of getter-less and gettered ceramic chip carriers,” in 2017 IEEE International Symposium on Inertial Sensors and Systems (INERTIAL), 2017, pp. 105–108.

[38] H. K. Charles and B. M. Romenesko, “The Reflow Attachment and Reliability Testing of Ceramic Chip Carriers,” in *19th International Reliability Physics Symposium*, 1981, pp. 93–103.

[39] A. Trusov et al, J. of Micromech. Microeng. 18 (2008).

[40] R. Bhiladvala et al, Physical Review E 69, (2004).

[41] P. Prikhodko et al, 46th International Symp. On Microelec., IMAPS (2013).

[42] SAES Getters Group, PageLid https://www.saesgetters.com/sites/default/files/PageLid%20Product%20 Datasheet_0.pdf

[43] R. Tabrizian, G. Casinovi, and F. Ayazi, “Temperature-stable silicon oxide (SilOx) micromechanical resonators,” IEEE Trans. Electron Devices, vol. 60, no. 8, pp. 2656–2663, 2013.

[44] B. Kim, M. A. Hopcroft, R. N. Candler, C. M. Jha, M. Agarwal, R. Melamud, S. A. Chandorkar, G. Yama, and T. W. Kenny, “Temperature Dependence of Quality Factor in MEMS Resonators,” *J. Microelectromechanical Syst.*, vol. 17, no. 3, pp. 755–766, Jun. 2008.

[45] V. P. Mitrofanov and K. V. Tokmakov, “Effect of heating on dissipation of mechanical energy in fused silica fibers,” *Phys. Lett. Sect. A Gen. At. Solid State Phys.*, vol. 308, no. 2–3, pp. 212–218, 2003.

[46] M. H. Asadian, S. Askari, and A. M. Shkel, “An Ultrahigh Vacuum Packaging Process Demonstrating Over 2 Million Q-Factor in MEMS Vibratory Gyroscopes,” *IEEE Sensors Lett.*, vol. 1, no. 6, pp. 1–4, 2017.

[47] R. Tabrizian, G. Casinovi, and F. Ayazi, “Temperature-stable silicon oxide (SilOx) micromechanical resonators,” *IEEE Trans. Electron Devices*, vol. 60, no. 8, pp. 2656–2663, 2013.

[48] Martinez, G.D., Li, C., Staron, A. et al. A chip-scale atomic beam clock. Nat Commun 14, 3501 (2023). https://doi.org/10.1038/s41467-023-39166-1.

[49] B. R. Simon, A. A. Trusov, and A. M. Shkel, “Anti-phase mode isolation in tuning-fork MEMS using a lever coupling design,” *Proc. IEEE Sensors*, pp. 295–298, 2012.

[50] Y. Tao, P. Navaretti, R. Hauert, U. Grob, M. Poggio, and C. L. Degen, “Permanent reduction of dissipation in nanomechanical Si resonators by chemical surface protection,” *Nanotechnology*, vol. 26, no. 46, 2015.

[51] J. Rodriguez, D. D. Gerrard, S. Chandorkar, Y. Chen, G. M. Glaze, I. B. Flader, C. H. Ahn, E. J. Ng, and T. W. Kenny, “Wide-range temperature dependence studies for devices limited by thermoelastic dissipation and anchor damping,” *TRANSDUCERS 2017 - 19th Int. Conf. Solid-State Sensors, Actuators Microsystems*, pp. 1100–1103, 2017.

[52] J. Yang, T. Ono, and M. Esashi, “Energy dissipation in submicrometer thick single-crystal silicon cantilevers,” *J. Microelectromechanical Syst.*, vol. 11, no. 6, pp. 775–783, 2002.

[53] A. Sharma, “CMOS systems and circuits for sub-degree per hour MEMS gyroscopes,” *Georg. Inst. Technol.*, no. December, p. 181, 2007.

[52] D. D. Lynch, "MRIG frequency mismatch and quadrature control," 1st IEEE Int. Symp. Inert. Sensors Syst. ISISS 2014 - Proc., no. 7, 2014.

[53] A. D. Challoner, H. H. Ge, and J. Y. Liu, "Boeing disc resonator gyroscope," Rec. - IEEE PLANS, Position Locat. Navig. Symp., pp. 504-514, 2014.

[54] Y. Xu et al., "0.015 Degree-Per-Hour Honeycomb Disk Resonator Gyroscope," in IEEE Sensors Journal, vol. 21, no. 6, pp. 7326-7338, 15 March15, 2021, doi: 10.1109/JSEN.2020.3046716.

[55] D. Endean et al., "Near-Navigation Grade Tuning Fork MEMS Gyroscope," Inert. 2019 - 6th IEEE Int. Symp. Inert. Sensors Syst. Proc., pp. 1-4, 2019.

[56] B. R. Johnson et al., "MEMS IMU for GPS-Denied Navigation."

[57] B. Johnson et al., "Development of a Navigation-Grade MEMS IMU," Inert. 2021 - 8th IEEE Int. Symp. Inert. Sensors Syst. Proc., pp. 2021-2024, 2021.

[58] https://eri-summit.darpa.mil/docs/ERIsummit2020/posters/26P_PRIGM_Polcawich_Honeywell_Poster.pdf

[59] M. Gadola et al., "1.3 mm 2 Nav-Grade NEMS-Based Gyroscope," vol. 30, no. 4, pp. 513-520, 2021.

[60] J. Y. Cho, S. Singh, J.-K. Woo, G. He, and K. Najafi, "0.00016 deg/ ? hr angle random walk (ARW) and 0.0014 deg/hr bias instability (BI) from a 5.2M-Q and 1-cm precision shell integrating (PSI) gyroscope," in Proc. IEEE Int. Symp. Inertial Sensors Syst. (INERTIAL), Mar. 2020.

[61] B. Hamelin, J. Yang, Z. Liu, and F. Ayazi, "Monocrystalline 4H Silicon Carbide-on-Insulator Substrates for Nav-Grade Planar BAW Gyroscopes," Inert. 2021 - 8th IEEE Int. Symp. Inert. Sensors Syst. Proc., pp. 2021-2024, 2021.

[62] Z. Liu and F. Ayazi, "A Review of Eigen-Mode and Frequency Control in Piezoelectric MEMS Resonators," IEEE Trans. Ultrason. Ferroelectr. Freq. Control, vol. PP, p. 1, 2023.

[63] D. Wang, M. H. Asadian, W. Guan, D. Hii, A. R. Parrish and A. M. Shkel, "Effect of Metallization on Quality Factor and Noise Characteristics in Fused Silica Dual-Shell Gyroscopes," in Journal of Microelectromechanical Systems, vol. 31, no. 6, pp. 877-887, Dec. 2022, doi: 10.1109/JMEMS.2022.3199231.

[64] R. Legtenberg, A. W. Groeneveld, and M. Elwenspoek, "Comb-drive actuators for large displacements," J. Micromech. Microeng., vol. 6, no. 3, pp. 320-329, 1996.

[65] S. Nitzan et al., "Epitaxially-encapsulated polysilicon disk resonator gyroscope," Proc. IEEE Int. Conf. Micro Electro Mech. Syst., pp. 625-628, 2013.

[66] S. Nitzan et al., "Impact of gyroscope operation above the critical bifurcation threshold on scale factor and bias instability," Proc. IEEE Int. Conf. Micro Electro Mech. Syst., pp. 749-752, 2014.

[67] J. D. Grade, H. Jerman and T. W. Kenny, "Design of large deflection electrostatic actuators," in Journal of Microelectromechanical Systems, vol. 12, no. 3, pp. 335-343, June 2003, doi: 10.1109/JMEMS.2003.811750.

[68] R. P. Leland, "Mechanical-thermal noise in MEMS gyroscopes," in IEEE Sensors Journal, vol. 5, no. 3, pp. 493-500, June 2005, doi: 10.1109/JSEN.2005.844538.

[69] R. R. Knight et al., "Large Amplitude Linear Drive Quadruple Mass Gyroscope," Inert. 2023 - 10th IEEE Int. Symp. Inert. Sensors Syst. Proc., pp. 4-7, 2023.

[70] A. A. Trusov et al., "Flat is not dead: Current and future performance of Si-MEMS Quad Mass Gyro (QMG) system," Rec. - IEEE PLANS, Position Locat. Navig. Symp., pp. 252-258, 2014.

[71] S. A. Zotov, I. P. Prikhodko, B. R. Simon, A. A. Trusov, and A. M. Shkel, "Self-calibrated MEMS gyroscope with AM/FM operational modes, dynamic range of 180 dB and in-run bias stability of 0.1 deg/hr," 2014 DGON Inert. Sensors Syst. ISS 2014 - Proc., 2014.

[72] B. R. Simon, A. A. Trusov, and A. M. Shkel, "Anti-phase mode isolation in tuning-fork MEMS using a lever coupling design," Proc. IEEE Sensors, pp. 1-4, 2012.

[73] S. Askari, M. Asadian, and A. Shkel, “Performance of Quad Mass Gyroscope in the Angular Rate Mode,” Micromachines, vol. 12, no. 3, p. 266, Mar. 2021, doi: 10.3390/mi12030266.

[74] Judy M W 1994 Micromechanisms using sidewall beams, PhD Dissertation Faculty of Electrical Engineering and Computer Sciences, University of California, Berkeley, CA

[75] G. K. Fedder, "Simulation of Microelectromechanical Systems," Univeristy Calif. Berkley Dr. Theis, p. 319, 1994.CMU MEMS Course, folded flexures, pp. 2-5.

[76] Senturia, Stephen D. Microsystem design. Springer Science & Business Media, 2005.

[77] Q. Shi, S. Wang, A. Qiu, Y. Xu, and X. Ji, "Design principle of suspension of MEMS gyroscope," Proc. 1st IEEE Int. Conf. Nano Micro Eng. Mol. Syst. 1st IEEE-NEMS, pp. 242-245, 2006.

[78] H. A. C. Tilmans, M. Elwenspoek, and J. H. J. Fluitman, "Micro resonant force gauges," Sensors and Actuators A Physical., vol. 30, no. 1-2, pp. 35-53, Jan. 1992, doi: 10.1016/0924-4247(92)80194-8.

[79] R. Q. Rudy, et al., "Dynamic quality factor equalization for improved bias stability in mode-matched gyroscopes," Inertial 2023 - 10th IEEE Int. Symp. Inert. Sensors Syst. Proc.

[80] T. Zhao and Y. C. Liang, "J I Eq J = J I," vol. 50, no. 6, pp. 2002-2004, 2003.

[81] D. A. Horsley, R. Horowitz, and A. P. Pisano, "Microfabricated electrostatic actuators for hard disk drives," IEEE/ASME Trans. Mechatronics, vol. 3, no. 3, pp. 175-183, 1998, doi: 10.1109/3516.712113

[82] S. Tez and M. Kaya, "A simulation study verified by experimental test results for frequency response analysis of MEMS comb-drive resonator," Microsyst. Technol., vol. 0123456789, 2023

[83] W. Zhang, H. Yan, Z. Peng, and G. Meng, "Electrostatic pull-in instability in MEMS / NEMS : A review," Sensors and Actuators A Physical, vol. 214, pp. 187-218, Aug 2014, doi: 10.1016/j.sna.2014.04.025.

[84] R. R. Knight and R. G. Polcawich, "A new approach to vacuum packaging of getter-less and gettered ceramic chip carriers," IEEE International Symposium on Inertial Sensors and Systems, INERTIAL 2017 - Proceedings, Mar. 2017, pp. 105-108, doi: 10.1109/ISISS.2017.7935658.

[85] R. R. Knight et al., "Micro-Torr Vacuum Packaging of Gettered Ceramic Chip Carriers," Inert. 2019 - 6th IEEE Int. Symp. Inert. Sensors Syst. Proc., vol. 26, no. 5, pp. 3-6, 2020.

[86] https://plasmatherm.com/pdfs/papers/Chip_2008-Process%20Latitude-Cornell.

[87] https://www.zhinst.com/sites/default/files/zi_appnote_mems_gyroscope.pdf

[88] P. Lines, IEEE Standards, vol. 2003, no. September. 2003.

[89] A. Mazzoni, R. Rudy, R. Knight, and J. Pulskamp, "Investigation of Thermoelastic Damping in Microelectromechanical System (MEMS)

Quadruple-Mass Gyroscope (QMG) Designs," ARL-TR-9216, Dist. A, 2021.

[90] H. Watanabe, N. Yamada, and M. Okaji, "Linear thermal expansion coefficient of silicon from 293 to 1000 K," International Journal of Thermophysics, vol. 25, no. 1, pp. 221-236, Jan. 2004, doi: 10.1023/B:IJOT.0000022336.83719.43

[91] T. Middelmann, A. Walkov, G. Bartl, and R. Schödel, "Thermal expansion coefficient of single-crystal silicon from 7 K to 293 K," Phys. Rev. B, vol. 92, no. 17, pp. 1-7, Nov. 2015, doi: 10.1103/PhysRevB.92.174113.

[92] Y. Yang et al., "Nonlinearity of Degenerately Doped Bulk-Mode Silicon MEMS Resonators," in Journal of Microelectromechanical Systems, vol. 25, no. 5, pp. 859-869, Oct. 2016, doi: 10.1109/JMEMS.2016.2586099.

[93] J. Kim, D. Cho, R. Muller, “Why is (111) Silicon a Better Mechanical Material for MEMS?,” In: Obermeier, E. (eds) Transducers ’01 Eurosensors XV. Springer, Berlin, Heidelberg, doi: 10.1007/978-3-642-59497-7_157

[94] I. N. Jleta, A. A. Hussein, and M. M. Khalfalla, "MEMS Inertial Sensors Modeling Using Power Spectral Density Method," no. 24, pp. 77-94.

[95] J. D. Emerard et al., "Si-MEMS gyro by Safran: Towards the navigation grade," Inert. 2022 - 2022 9th IEEE Int. Symp. Inert. Sensors Syst. Proc., pp. 1-4, 2022.

[96] S. Koenig et al., "A configurable single axis Si-MEMS Gyro," 2021 DGON Inert. Sensors Syst. ISS 2021 - Proc., pp. 1-14, 2021.

[97] S. Koenig et al., "Towards a navigation grade Si-MEMS gyroscope," 2019 DGON Inert. Sensors Syst. ISS 2019 - Proc., pp. 1-18, 2019.

[98] B. Hamelin, J. Yang, Z. Liu, and F. Ayazi, "Monocrystalline 4H Silicon Carbide-on-Insulator Substrates for Nav-Grade Planar BAW Gyroscopes," Inert. 2021 - 8th IEEE Int. Symp. Inert. Sensors Syst. Proc., pp. 2021-2024, 2021.

[99] T. G. Walker and M. S. Larsen, "Spin-exchange-pumped NMR gyros," Advances In Atomic, Molecular, and Optical Physics, Elsevier, vol. 65, pp. 373-401, Jan. 2016, doi: 10.1016/bs.aamop.2016.04.002.

[100] S. Gundavarapu, M. Belt, T. Huffman, M. Tran, T. Komljenovic, J. Bowers, and D. Blumenthal, "Interferometric Optical Gyroscope Based on an Integrated Si3N4 Low-Loss Waveguide Coil," J. Lightwave Technol. 36, Issue 4, 1185-1191 Feb. 2018, doi: 10.1109/JLT.2017.2765918.

[101] G. Langfelder, M. Bestetti, and M. Gadola, "Silicon MEMS inertial sensors evolution over a quarter century," J. Micromech Microeng, vol. 31, no. 8, pp. 084002, Aug. 2021, doi: 10.1088/1361-6439/ac0fbf.

[102] https://www.sitime.com/products/ruggedized-mhz-super-tcxos/sit5543

[103] Miller, J.M.L., Ansari, A., Heinz, D.B., Chen, Y., Flader, I.B., Shin, D.D., Villanueva, L.G. and Kenny, T.W., 2018. Effective quality factor tuning mechanisms in micromechanical resonators. *Applied Physics Reviews*, *5*(4).

[104] J. DeNatale, S. Martel, F. Dion and J. Lachance, "Manufacturing Transition of High-Performance MEMS Gyroscopes", 2020 IEEE/ION Position Location and Navigation Symposium (PLANS), pp. 24-26, 2020.

[105] J. DeNatale, P. Stupar, S. Martel and J. Lachance, "Manufacturing Platform for High-Performance MEMS Inertial Sensors," 2023 IEEE/ION Position, Location and Navigation Symposium (PLANS), Monterey, CA, USA, 2023, pp. 6-9, doi: 10.1109/PLANS53410.2023.10140045.

[106] N. E. Bousse, J. M. L. Miller, H. Kwon, G. D. Vukasin and T. W. Kenny, "Quality factor tuning of micromechanical resonators via electrical dissipation", Appl. Phys. Lett., vol. 116, no. 023506, 2020.

[107] J. Chen, T. Tsukamoto and S. Tanaka, "Triple Mass Resonator with High Capacity to Tune Frequency and Quality Factor", 2020 IEEE International Symposium on Inertial Sensors and Systems, 2020.

[108] A. A. Trusov, S. A. Zotov and A. M. Shkel, "Electrostatic regulation of quality factor in non-ideal tuning fork MEMS" in 2011 IEEE SENSORS, Limerick, Ireland, 2011.

[109] https://en.m.wikipedia.org/wiki/Hemispherical_resonator_gyroscope

[110] R. Q. Rudy et al., "Tunable quality factor resonators for inertial sensors", 2020 IEEE IFCS.